VERITAS observations of galactic compact objects

Roxanne Guenette

Doctor of Philosophy

Department of Physics

McGill University

Montreal,Quebec

2010-08-30

A thesis submitted to McGill University in partial fulfilment of the requirements of the degree of Doctor in Philosophy.

À ma mère Danièle,

pour sa présence exceptionnelle dans ma vie.

ACKNOWLEDGEMENTS/REMERCIEMENTS

I would first like to thank my supervisor, Ken Ragan, who gave me with the opportunity to work on a great experiment. He gave me the freedom to find my own path of interest and while providing me with the necessary support when I wanted to present my results at international conferences or to attend summer schools or collaboration meetings.

I also want to thank the whole McGill VERITAS group. David Hanna was always available to provide useful and pertinent comments and suggestions. I am extremely thankful to the all my office mates: Audrey MacLeod (who always patiently listened to my concerns, science related or not, and was a really good travel companion for several conference trips), Andrew McCann (who, with his enthusiasm about the VERITAS project, keeps the troops motivated, who greatly improved the enjoyment of the long months passed on Mount Hopkins in Arizona and was really helpful at one CASCA conference), Micheal McCutcheon (who's with his encyclopedic knowledge was always there to answer questions or to bring light on complex problems), Luis Valcarcel (who was very patient with all the coding questions I had), Mary, Sean and Jonathan. Thanks to the post-docs John Kildea (for the joy he brought to the group and for the help he gave me for several things), Peter Cogan and Gordana Tesic (who always accepted to help me and was a great travel companion).

I also owe an enormous "Danke" to Gernot Maier. I had the chance to work with him during my entire Ph.D.. He really showed me what the word efficiency means. Gernot was extremely helpful with all aspects of the work in VERITAS and this work would not have been possible without his contributions and help.

I thank all the VERITAS members that helped me along during my PhD, scientifically and mentally (especially during those long hours of observations). Gracias a Ana, Ester, Luis por su paciencia con mi español y todos los momentos divertidos durante estos años. Muchas gracias a Victor por su presencia y por todas las fiestas en Tucson.

I also want to thank Paul Mercure, who helped me a lot with my computer problems. To all the McGill students that shared my PhD life (Seb, Pat, Rene, Aaron, Cindy, Marjorie, Rhiannon, James, and the softball team): thank you.

Un gros merci à ma gang d'amis physiciens de l'Université de Montréal: Yoni, Phil, Ariane, Hélène, Pat, Vincent, P-L, Gen, Julien et les autres. Vous m'avez permis de maintenir une santé d'esprit (à long terme du moins). Merci à ma gang de Mont-lo: Milou, Stef et Jou.

Merci à tous les membres de ma famille, qui m'ont apporté leur support tout au long des ces années. Merci à mes parents de m'avoir encouragée et permis de réaliser ce long projet. Un merci très spécial à ma tante Marie-France, qui m'a apporté une aide énorme tout au long de mes études.

A very special thank you to my boyfriend Laurie Shaw, who shared my life during all these years. His presence, support and encouragements made everything better and easier.

Finally, thanks to McGill University, to FQRNT and to NSERC for providing the financial support that made this work possible.

ABSTRACT

VERITAS consists of an array of four 12 m imaging atmospheric telescopes, designed to observe very high energy (VHE) gamma-ray emission between 100 GeV and 30 TeV. In this thesis, galactic compact objects, observed with the VERITAS telescopes, will be presented.

Magnetars are highly magnetized neutron stars. Three magnetars were observed by VERITAS: 4U 0142+61, 1E 2259+586 and SGR 0501+4516. No significant gamma-ray emission was observed during the quiescent phase. These results support the current magnetar models, which do not predict any VHE emission. No data were acquired during outburst activity. Magnetar observations during outburst are now part of the VERITAS burst alert program.

It is now known that X-ray binaries can emit in the TeV regime. There is no clear correlations with physical properties that could indicate with certainty which ones are TeV emitters. Data on 15 X-ray binaries were retrieved from VERITAS archival data. No gamma-ray emission was observed from any of the systems. Due to the differences between the systems studied and the three known TeV emitters, no conclusions could be made on the physical properties that might be responsible for TeV emission.

The SS 433 system, hosting a black hole (BH), exhibits two powerful jets. TeV emission has been predicted from near the BH and from the regions where the jets hit the surrounding medium. VERITAS acquired $\sim$19 h of data on the system, allowing analyses at the BH and at the region where the western jet interacts with the surrounding medium (w2). No significant gamma-ray emission was observed. From the results at the black hole position, constraints were put on a theoretical model of emission. In the case of the w2 region, an excess, lower than the canonical detection level of 5 σ, was observed. This excess is not attributed yet to gamma-ray emission; more data are required to confirm or refute the excess as a gamma-ray signal. If the excess is treated as a statistical fluctuation, the upper limit on the gamma-ray flux is too weak to constrain the theoretical model. If more observations reveal gamma-ray emission, the flux level would place strong constraints the model.

RÉSUMÉ

VERITAS est un réseau de quatre télescopes Cherenkov à imagerie de 12 m, conçu pour l'observation de rayons gamma entre 100 GeV et 30 TeV. Dans cette thèse, plusieurs objets compacts galactiques, observés par VERITAS, seront présentés.

Les magnétars sont des étoiles à neutron fortement magnétiques. Trois magnétars ont été observés par VERITAS: 4U 0142+61, 1E 2259+586 et SGR 0501+4516. Aucune émission de rayons gamma n'a été détectée. Ces résultats supportent les modèles théoriques actuels, qui ne prédisent aucune emission à ces énergies. Aucune donnée n'a été enregistrée pendant un épisode de sursaut d'activité. L'observation de magnétars pendant un sursaut fait maintenant partie du programme d'alerte de sursauts de VERITAS.

Il est maintenant connu que les binaires à rayons X peuvent émettre dans le régime des TeV. Il n'y a cependant pas de corrélations claires entre les propriétés physiques de ces objets qui pourraient indiquer avec certitude les propriétés responsables de l'émission à très haute énergie. Des données sur 15 binaires à rayons X ont été retirées des archives de VERITAS. Aucune émission gamma n'a été détectée dans ces sytèmes. Aucune conclusion n'a pu être tirée sur les propriétés physiques qui pourraient être responsables de l'émission gamma, due aux trop grandes différences entre les systèmes étudiés et les trois systèmes émettant dans les TeV.

Le système SS 433, comprenant un trou noir (TN), présente deux puissants jets. L'émission de rayons gamma a été prédite près du TN et dans les régions où les jets entrent en contact avec le matériel environnant. VERITAS a obtenu $\sim$19 h de

données sur le système, permettant l'analyse à la position du TN et à l'endroit où le jet ouest interagit avec le matériel environnant (w2). Aucune émission gamma n'a été détectée à aucun des endroits. Les résultats à la position du TN ont permis de mettre des contraintes sur le modèle théorique. Dans le cas de la région de w2, un excès, inférieur au niveau de détection de 5 σ, a été observé. Cet excès ne peut cependant pas être attribué à un signal de rayons gamma. Plus de données sont nécessaires afin de confirmer ou infirmer ce résulat. En considérant ce signal comme une fluctuation statistique, la limite supérieure obtenue ne permet pas de contraindre le modèle théorique. Si des observations supplémentaires indiquent une émission gamma, le niveau de flux placerait de fortes contraintes sur le modèle.

TABLE OF CONTENTS

LIST OF TABLES

LIST OF FIGURES

INTRODUCTION

The field of very high energy (VHE) gamma-ray astrophysics started twenty years ago with the discovery of TeV gamma-ray emission from the Crab Nebula. Since then, the field has undergone an exponential evolution, with now more than 100 objects observed at TeV energies. The new generation of imaging atmospheric Cherenkov telescopes, H.E.S.S., MAGIC and VERITAS, have moved the field forward. The observations performed today in the TeV energy band contribute significantly to understanding the physical processes involved in astrophysical objects, revealing the most energetic part of the electromagnetic spectrum.

Extragalactic (as well as galactic) astrophysics, has benefited from TeV observations. VHE emission from active galactic nuclei demonstrates efficient particle acceleration along the powerful relativistic jets produced in these galaxies. TeV gamma rays emitted by pulsar wind nebulae show that the pulsar wind, interacting with its surroundings, can accelerate particles up to TeV energies. These results are essential to develop theoretical models that can explain emission up to those energies.

While extragalactic astrophysics accounts for over 30% of the TeV emitting sources, galactic astrophysics has been revealed to have more source classes. Among the 74 TeV galactic emitters, four identified classes emerge: pulsar wind nebulae, supernova remnants, X-ray binaries and young star clusters. Nevertheless, over 40% of the sources emitting in the TeV regime remain unidentified.

While theoretical models are being created and developed to explain the physical processes occurring in galactic sources, the hunt for new source classes of TeV emitters continues. Eccentric objects, such as magnetars or microquasars, are observed by TeV experiments, in order to provide additional information on the exotic behavior of these objects. Some objects have already been identified by theoretical models as potential TeV emitters. The detection or the non-detection of TeV gamma rays from these objects is therefore crucial to validate or refute the models.

Since 2008, the *Fermi* satellite has joined the effort. Built to detect gamma rays with energies between 20 MeV and 300 GeV, the *LAT* instrument on board *Fermi* is bridging the gap between soft gamma-ray satellites and ground based TeV experiments. It is now possible to study high energy processes in astrophysical objects from the X-rays to TeV gamma rays. Such coverage is essential to distinguish between the physical mechanisms responsible for the different emissions. Astrophysicists now have powerful tools to push forward the frontiers of knowledge.

Thesis outline

This thesis reports on VERITAS observations of compact galactic objects. Magnetars, X-ray binaries and the SS 433 system have been analyzed and studied.

In Chapters 1 to 3, a brief overview of history and science of the gamma-ray astrophysics will be presented. Since gamma-ray telescopes do not directly detect the incoming gamma rays, a detailed description of the gamma-ray detection technique will be presented. The VERITAS experiment will also be described.

In Chapter 4, the details of the analysis techniques will be presented in order to understand the results presented further in the thesis. Each step of the analysis used by the VERITAS collaboration will be detailed.

In Chapter 5, magnetars will be reviewed. A brief overview of the objects and the radiative processes involved will be given. Theoretical models predicting very high energy emission for magnetars will be described. The VERITAS observations and results on three magnetars (4U 0142+61, 1E 2259+586 and SGR 0501+4516) will be presented, as well as the physical interpretations of these results.

In Chapter 6, a review of X-ray binaries, including their physical properties and radiative mechanisms, will be given. The small class of X-ray binaries emitting in the TeV band will be described in detail, as well as the theoretical models proposed to explain the VHE emission. A search in the VERITAS archival data allowed the analysis of 15 binary systems. The results for these systems will be presented, as well as the implications for theoretical models.

Finally in Chapter 7, the SS 433 system, a microquasar with powerful relativistic jets firing into the surrounding interstellar medium, will be described. Observations at different wavelengths will be presented in order to understand the radiative processes involved in the system. Two theoretical models predicting VHE emission from the SS 433 system will be reviewed in detail. VERITAS observations and results at the black hole position and at the region where the western jet is interacting with the surrounding material will be presented, as well as the interpretation of those results regarding the two theoretical models.

CHAPTER 1
Gamma-ray astrophysics

Gamma rays stand at the most energetic end of the electromagnetic spectrum. In astrophysics, their observed energies cover over eight orders of magnitude, going from ∼1 MeV to ∼100 TeV. In this chapter, a brief review of the history of the experiments having contributed (or contributing) to the field of gamma-ray astrophysics will be given. The science that is done at gamma-ray wavelengths will also be presented.

1.1 History of γ-ray experiments

Gamma-ray energies span over eight orders of magnitude and the most energetic gamma rays require more collection area and material depth to be detected than lower energy ones. At TeV energies, for example, the fluxes involved are very low, requiring huge collection areas, rendering space observatories totally inefficient. The history of the field approximately follows the energy of the particles. For this reason, this section is ordered by gamma-ray energy.

1.1.1 Soft gamma rays

Soft gamma rays have energies between ∼100 keV and ∼10 MeV. Gamma-rays, similar to X-rays, are absorbed by the atmosphere (see Section 2.1); therefore, satellites are required to detect them directly. The first experiments dedicated to the detection of soft gamma rays were the Orbiting Solar Observatory (OSO) missions. In 1962, NASA launched OSO 1, designed to study solar radiation. One instrument on board was dedicated to detecting soft gamma rays from space. This instrument operated in the energy range between 50 keV and 3 MeV. The science outputs of this mission were slight; however, it provided useful information on the technical aspects of gamma-ray detection.

Several other satellite missions were launched from the 1960s to the 1990s. Among these, the Vela satellites (Vela 5A and 5B) are worth mentioning. Indeed, these satellites, designed to operate in the 150-750 keV energy range to detect nuclear tests, were the first to discover gamma-ray bursts (GRBs). They operated for 10 years. The other satellite missions did not make important scientific contributions in the field of soft gamma-ray astrophysics, even though they were useful to understand and improve the detectors.

It is only in 1991 that a dedicated satellite for gamma-ray astrophysics, sensitive to soft γ rays was launched. The NASA Compton Gamma Ray Observatory (CGRO) was composed of four instruments. In the soft γ-ray regime, BATSE (Burst And Transient Source Experiment) was dedicated to gamma rays in the 20 keV to 1 MeV energy range, OSSE (Oriented Scintillation Spectrometer Experiment) was designed to operate at energies between 50 keV and 10 MeV and the COMPTEL (imaging

COMPton TELescope) instrument was for gamma rays with energies between 800 keV and 30 MeV. (The fourth instrument, EGRET, will be described below). The satellite is shown in Figure 1–1.

BATSE contributions to gamma-ray astrophysics were important. Indeed, the instrument detected over 2000 GRBs (showing that they were distributed isotropically in the sky) over 2000 transient sources and nearly 200 soft gamma-ray repeater (SGR) bursts. The CGRO satellite was decomissioned in 2000.

Figure 1–1: The CGRO satellite. Figure taken from [88].

In 2002, the INTEGRAL (INTErnational Gamma-Ray Astrophysics Laboratory) mission was launched by ESA (European Space Agency) to study soft γ rays with energies between 15 keV and 8 MeV.

In June 2008, the *Fermi* satellite was launched by NASA. One of the instruments on board, the GBM (Gamma-ray Burst Monitor), is designed to study gamma rays in the energy range between 8 keV and 1 MeV. In its first year of operation, the GBM instrument detected over 250 GRBs. Figure 1–2 shows the *Fermi* satellite.

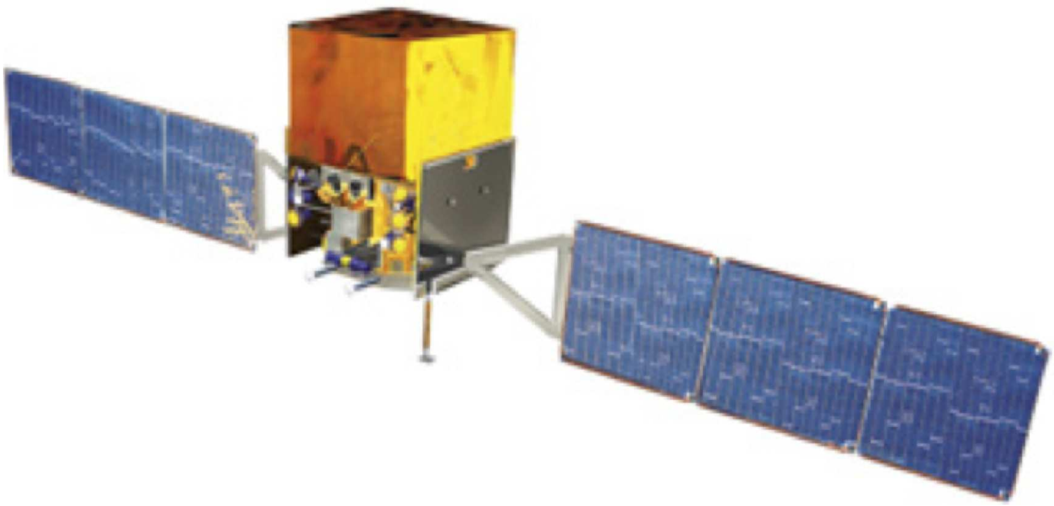

Figure 1–2: The *Fermi* satellite. Figure taken from [85].

1.1.2 High energy gamma rays

High energy (HE) gamma rays have energies from ∼10 MeV to ∼100 GeV. The first mission dedicated to HE gamma rays was the Explorer XI satellite launched in 1961 by NASA. This satellite was designed to detect gamma rays with energies higher than 50 MeV. A total of 22 γ rays were detected in the nine hours of data recorded during the mission.

In 1972, the Small Astronomy Satellite 2 (SAS 2) was launched by NASA. This satellite was the first entirely dedicated to gamma-ray astronomy. It was designed to operate in the energy range from 20 MeV to 1 GeV. Gamma rays from the Crab and the Vela pulsars were detected and HE γ-ray astrophysics was born. In addition, a first look was taken at the gamma-ray sky.

In 1975, the ESA launched the COS-B mission, dedicated to gamma-ray energies between 30 MeV and 5 GeV. This mission produced a gamma-ray map of the galaxy as well as detailed observations of the Geminga pulsar.

Although the previously mentioned missions opened the field of HE gamma-ray astrophysics, it was with the launch of CRGO, and specifically the EGRET (Energetic Gamma-Ray Experiment Telescope) instrument, that the field really took a major step forward. EGRET was dedicated to the observation of HE gamma rays with energies between 20 MeV and 30 GeV. EGRET revolutionized the field of HE gamma-ray astrophysics. The instrument produced the first map of the sky at energies above 100 MeV (see Figure 1–3) and detected over 250 sources. EGRET showed that blazars were sources of HE γ-ray emission. To date, many sources detected by EGRET have still not been identified. With the numerous new sources, scientists were able to use the EGRET observations to test theoretical predictions as well as to develop new models.

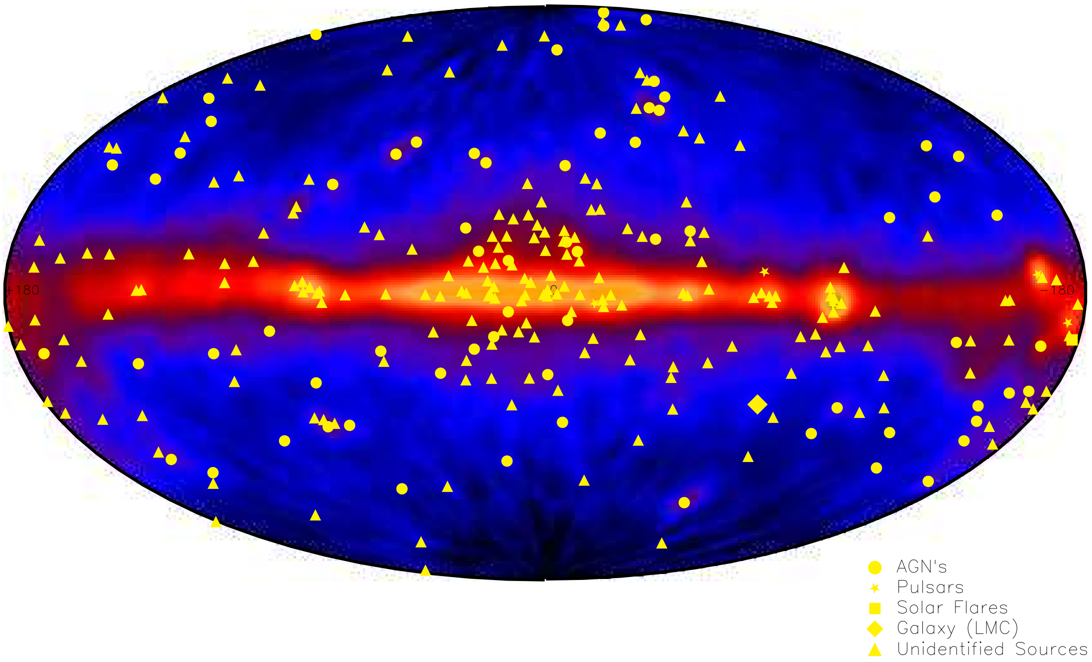

Figure 1–3: Skymap at energies above 100 MeV as seen by EGRET. The EGRET sources for the 3rd EGRET catalog are also shown. Figure taken from [87].

In April 2007, an Italian satellite, AGILE (Astro-rivelatore Gamma a Immagini LEggero), was launched to study in more detail the gamma-ray HE sky at energies between 30 MeV and 50 GeV. The satellite is still taking data.

Although the success of the CGRO mission is incontestable, its achievements have been surpassed by those of the *Fermi* satellite. Since its launch in 2008, *Fermi* has taken a deeper look at the HE gamma-ray sky. The LAT (Large Area Telescope) instrument, designed for γ rays in the 20 MeV-300 GeV energy range, has greatly extended our knowledge of HE gamma-ray astrophysics. Indeed, from the first year of data, over 1000 gamma-ray sources have been detected, including many different (and many new) classes of γ-ray sources, such as millisecond pulsars (some of which are only visible in the HE regime), globular clusters and starburst galaxies. Figure 1–4 shows the sky as viewed by *Fermi* at energies above 100 MeV.

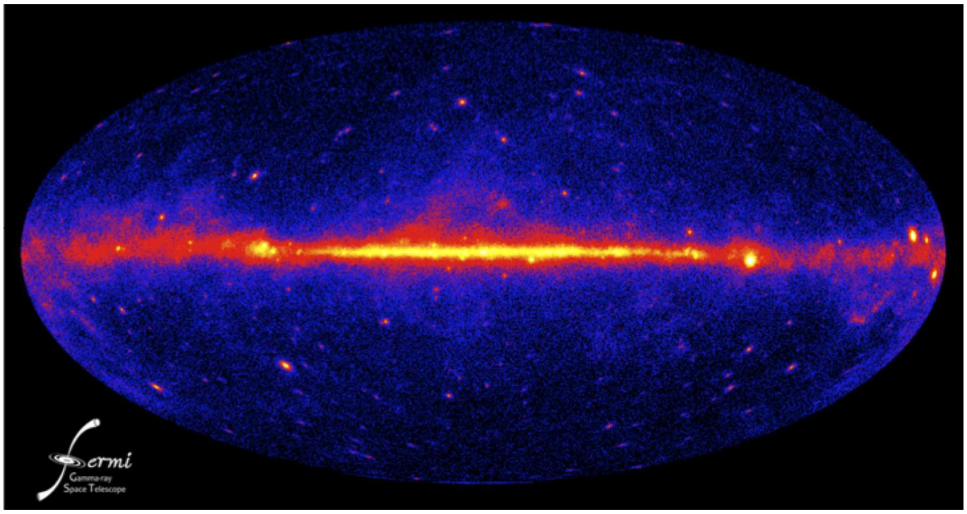

Figure 1–4: Skymap at energies above 300 MeV as seen by *Fermi*/LAT after one year of data. Figure taken from [90].

1.1.3 Very high energy gamma rays

Very high energy (VHE) gamma rays have energies between ∼100 GeV and ∼50 TeV. At these energies, satellite detection is not efficient (the collection area too is small). From the ground, VHE gamma rays are detected by using Cherenkov telescopes (see Chapter 2 for more details).

The idea of detecting Cherenkov light from air showers was first proposed by P.M. Blackett in 1948 [22], who suggested that Cherenkov light would represent 0.01% of the total night sky background. Blackett's idea was later tested in 1952 and confirmed in 1955 by W. Galbraith and J.V. Jelley [59, 60].

In 1968, T.C. Weekes and his group built the Fred Lawrence Whipple Observatory (FLWO) 10 m Cherenkov telescope (see Figure 1–5). In 1989, they made the first detection of TeV gamma rays coming from the Crab Nebula [174]. The era of TeV gamma-ray astrophysics was born. In the 1990s, the first array of Cherenkov telescopes was built by the HEGRA collaboration [99]. The complete array consisted of five 8.5 m^2 telescopes. The improvement from stereo observations was significant (see Section 2.2.3).

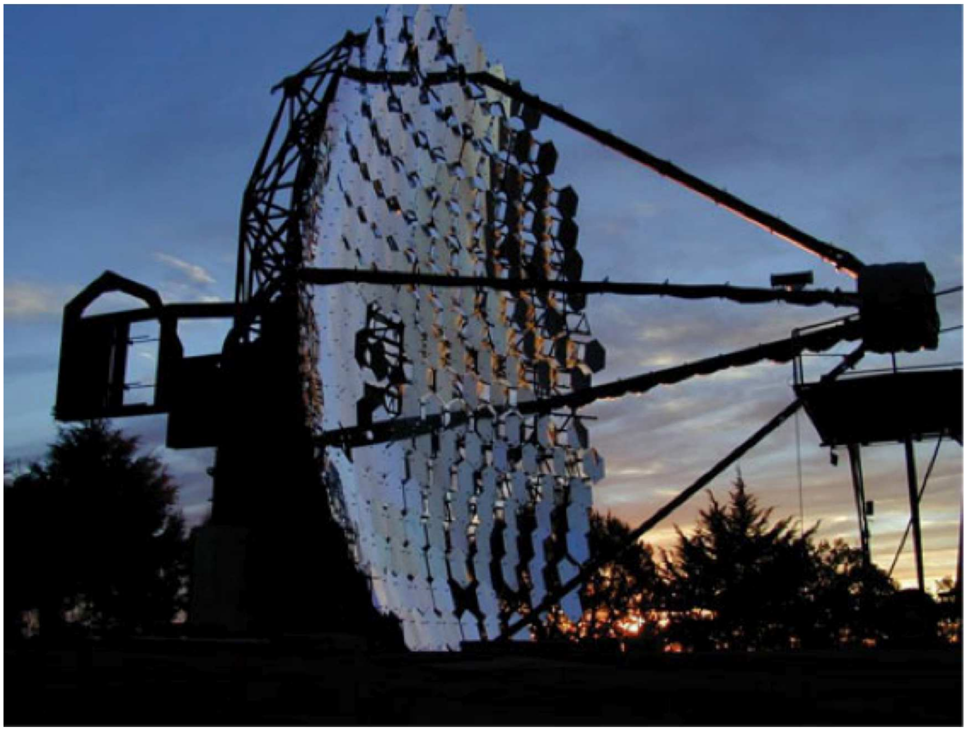

Figure 1–5: The 10 m Whipple telescope. Figure taken from [94].

Finally, at the beginning of the 2000's, a new generation of Cherenkov telescopes came into operation. The MAGIC telescope is composed of two 17 m telescopes [89] and the H.E.S.S and VERITAS arrays are composed of four 12 m telescopes [100, 93]. This new generation brought the number of TeV sources from a handful to over 100. Figure 1–6 shows the known TeV sources as of the beginning of 2010.

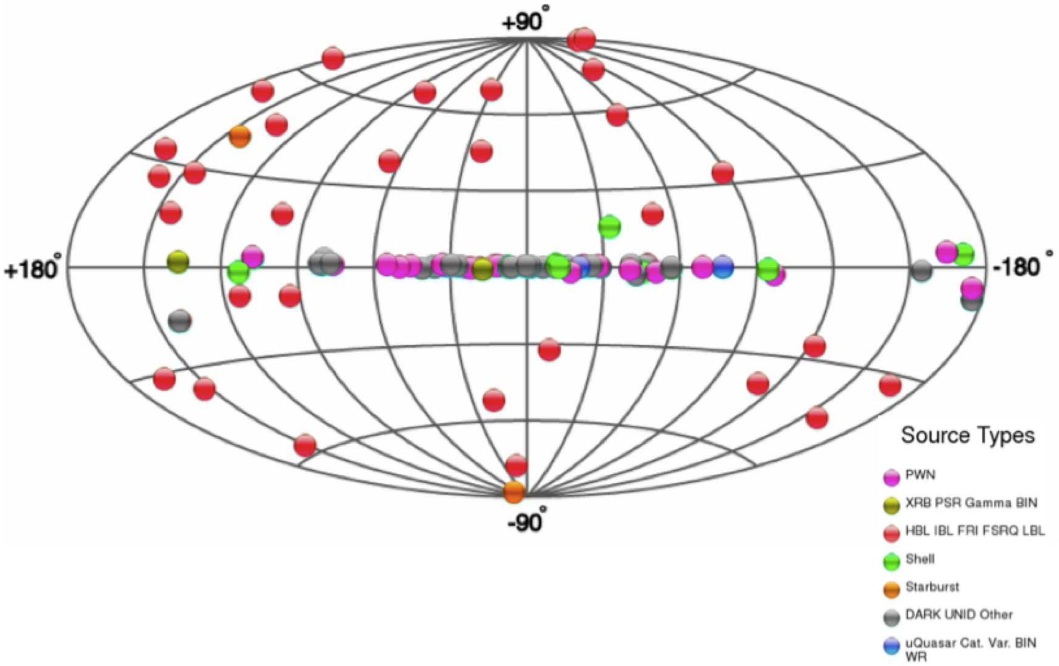

Figure 1–6: Known TeV sources. Figure produced by tevcat [91].

At the time of writing (early 2010), the MAGIC and H.E.S.S. collaborations are working to upgrade their arrays. MAGIC has built a second 17 m telescope and is now operating with both telescopes and H.E.S.S. is building a fifth telescope of 30 m aperture, that will be placed at the center of their array. In addition, two major projects are on their way for the next generation of Cherenkov telescope arrays. The AGIS (Advanced Gamma-ray Imaging System) [95] and CTA (Cherenkov Telescope Array) [98] collaborations are planning to build arrays of tens of telescopes (from 15 m to 25 m telescopes). Figure 1–7 shows a possible layout of the CTA experiment. This new generation will reach sensitivities 5 to 10 times higher than the current generation.

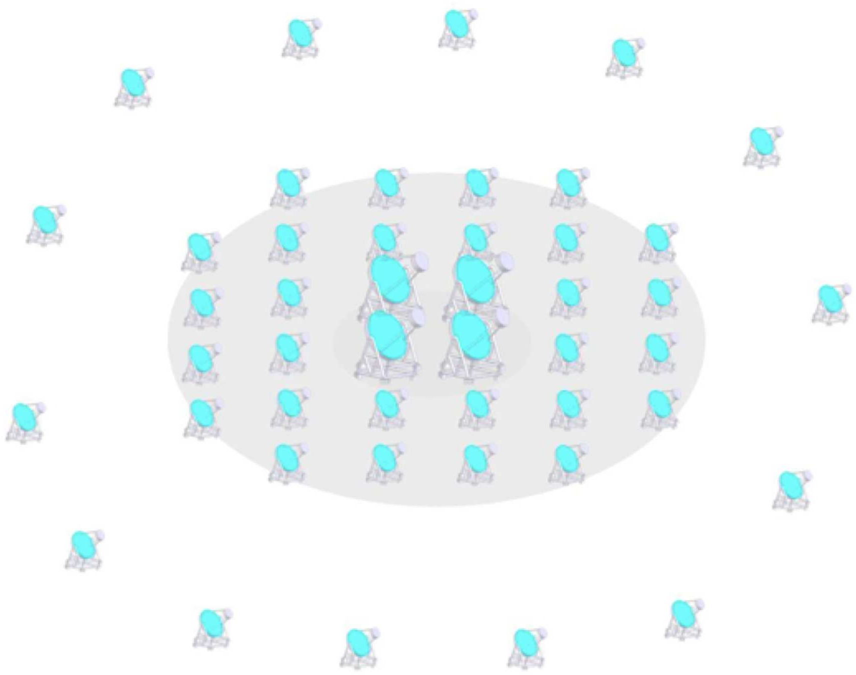

Figure 1–7: Possible layout of the CTA experiment. Four 25 m telescopes are placed at the center and 12 m to 18 m telescopes are distributed over the rest of the area. Figure taken from [98].

1.1.4 Ultra high energy gamma rays

Ultra high energy (UHE) gamma rays have energies higher than $\sim$50 TeV. As for VHE γ rays, UHE gamma rays can only be detected by the air showers that they produce in the atmosphere. Cosmic rays have been studied intensively since their discovery in 1938 by Pierre Victor Auger. But it was only in 1989 that an experiment dedicated to the search for UHE gamma rays was built. CASA−MIA (Chicago Air-Shower Array MIchigan muon Array) was designed to search for sources of gamma rays with energies higher than 100 TeV; none were detected [24].

The Milagro experiment [92], which consisted of a water Cherenkov detector, started to take data in 1998. It was operated for ten years, probing the gamma-ray sky between 1 and 100 TeV. The Milagro skymap is shown in Figure 1–8. A next generation water Cherenkov experiment is under construction: the HAWC (High Altitude Water Cherenkov) experiment [86]. This experiment will operate between 100 GeV and 100 TeV and will have a sensitivity 10 to 15 times better than Milagro's.

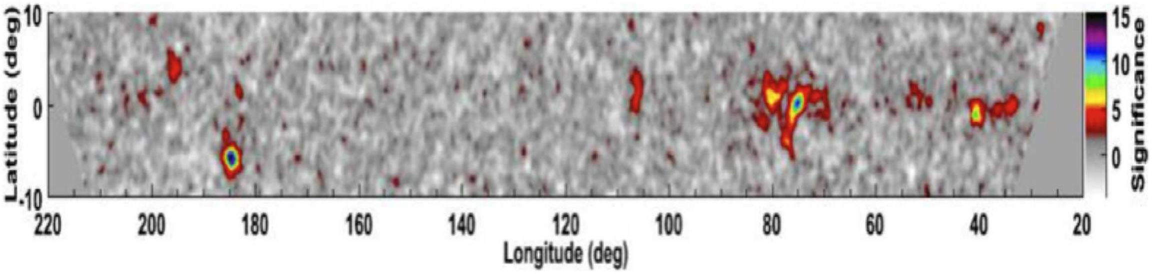

Figure 1–8: Gamma-ray sky in galactic coordinates (between 20° $< l <$ 220° and -10° $< b <$ 10°) at energies between 1 TeV and 100 TeV as seen by the Milagro experiment. Figure taken from [92].

1.2 VHE γ-ray sources

Since the beginning of the era of air Cherenkov telescopes, more than 100 TeV sources have been detected. Despite the large number of objects, they represent only six source classes: AGNs (active galactic nuclei), SNRs (supernova remnants), binary systems, PWNe (pulsar wind nebulae), young star clusters and, more recently, starburst galaxies. In this section, a review of these classes will be presented.

1.2.1 Extragalactic astrophysics

AGNs, mainly blazars, were among the first objects to be detected by the first generation of Cherenkov telescopes, such as Whipple. After more than 20 years of observations of the VHE gamma-ray sky, they are the most numerous VHE source class. To date, almost 30% of known TeV sources are AGNs. Recently, a new class of extragalactic TeV emitters has been discovered; starburst galaxies.

Blazars

Galaxies with AGN are galaxies thought to be hosting a supermassive black hole. The gravitational energy released from the accretion of matter onto the black hole powers relativistic jets emerging along the spin axis of the black hole. Figure 1–9 shows an image of the AGN jets. The luminosity of these galaxies is dominated by the emission from the core.

Blazars are active galaxies that have their jets oriented towards the Earth (see Figure 1–10). The first blazar to be discovered was Markarian (Mrk) 421 [140]. When in an intense flaring state, Mrk 421 is the brightest source in the TeV sky. The VHE detection of AGNs proved that the relativistic jets are efficient particle accelerators. In addition, the observations showed that AGNs are variable sources with flaring states having fluxes more than an order of magnitude greater than the flux of the quiescent emission.

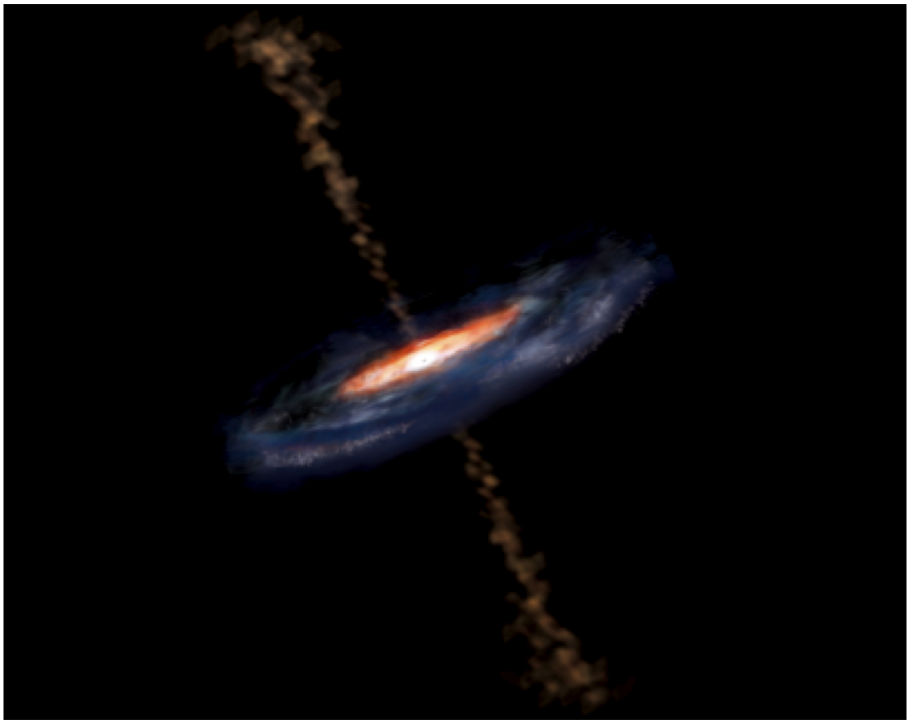

Figure 1–9: Artist's view of an AGN showing the relativistic jets. Figure taken from [101].

Radio galaxies

As shown in Figure 1–10, radio galaxies are AGNs having their jets oriented at an angle greater than ∼20° from the line of sight. The radio emission from these galaxies (more precisely from the jets) reveals the presence of relativistic particles. Radio galaxies have been observed as VHE emitters, for example, M87 [8] and Cen A [15]. Recently, a multiwavelength campaign performed by VERITAS, H.E.S.S. and Chandra (an X-ray satellite) on M87 showed that the VHE emission seems to be coming from the core of the galaxy [5].

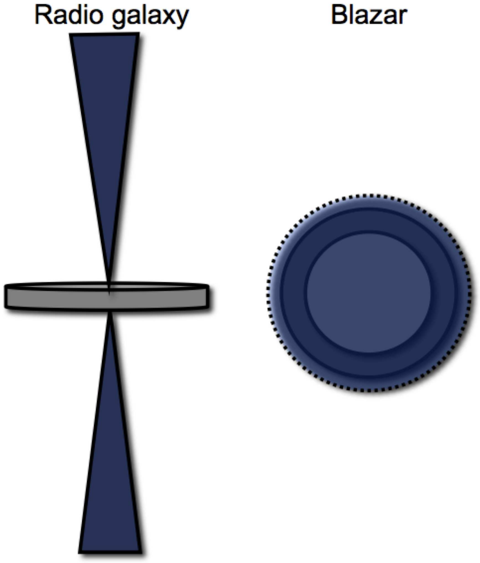

Figure 1–10: Blazars are AGNs having their jets pointing towards Earth (right figure) while radio galaxies have their jets oriented off-axis (90° here) from the line of sight (left figure).

Starburst galaxies

Starburst galaxies are galaxies containing regions of intense star formation. Recently, the VERITAS collaboration discovered VHE emission from the starburst galaxy M82 [6]. It was shortly followed by the discovery of VHE emission from NGC 253 by the H.E.S.S. collaboration [7]. These discoveries are important because they may help to answer the long-lasting question of the origin of cosmic rays. Indeed, the high density of cosmic rays in M82 may be responsible for the VHE emission.

1.2.2 Galactic astrophysics

The Crab Nebula was the first TeV source detected (see Section 1.1.3). Four classes of galactic sources have been found to emit at TeV energies; PWNe, SNRs, binary systems and young star clusters containing Wolf-Rayet stars. Several galactic TeV sources are still unidentified. Thus, the classes of objects emitting at VHE may well be enlarged soon.

Pulsar Wind Nebulae

PWNe (or plerions), are systems where a supernova remnant surrounding a rapidly rotating pulsar interacts with the pulsar wind. The wind, consisting of a stream of particles, created by the fast rotation of the pulsar and its magnetic field, interacts with the material of the SNR, producing non-thermal emission. PWNe constitute the most populous class of galactic TeV emitters. Figure 1–11 shows the Crab Nebula, a typical example of PWNe. The Crab Nebula is a bright steady TeV gamma-ray source that is used by TeV experiments as a standard candle.

Supernova Remnants

The distinction made here between PWNe (which are surrounded by SNRs) and SNRs is that in the latter, the emission comes from the shell of the remnant itself. Several SNRs have been detected in the VHE range, proving the existence of efficient particle acceleration. The VHE gamma rays are produced by the interaction of the shock of the supernova with the surrounding medium. It is still unclear if it is the acceleration of electrons or of protons that is responsible for the gamma-ray emission, but answering this question will also likely provide explanations for the origin of cosmic rays. SNRs are thought to be cosmic-ray accelerators.

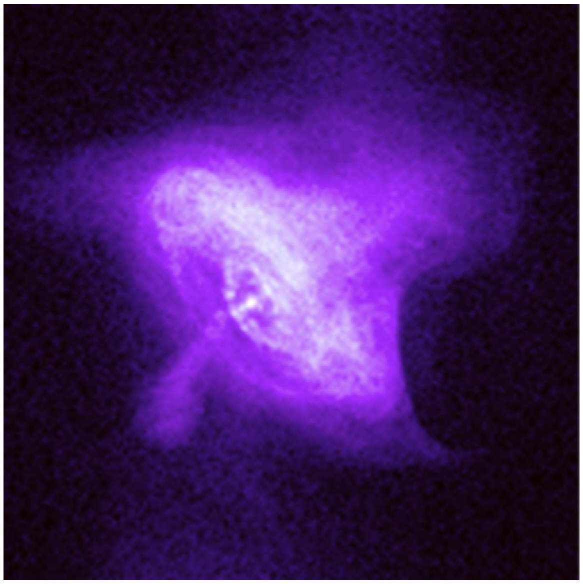

Figure 1–11: The PWNe of the Crab as seen in X-rays. The wind created around the pulsar is visible. Figure taken from [83].

Binary systems

Another class of galactic TeV emitters, with only three members, is X-ray binaries. X-ray binaries are systems composed of a compact object (black hole or neutron star) and a stellar companion. A detailed description of these systems is given in Chapter 6. Three high mass X-ray binaries have been detected as VHE emitters. The emission mechanisms are not yet well understood, but for at least one system (PSR B1259-63), it probably comes from the shock between the pulsar wind of the compact object and the stellar wind of the companion.

Young star clusters

Two young star clusters have been detected at TeV energies: Westerlund 1 [136] and Westerlund 2 [14]. These two clusters are populated by massive stars, including

Wolf-Rayet stars. It is still unclear what is responsible for the VHE gamma-ray emission. In the case of Westerlund 1, the PWNe from the pulsar PSR J1648-4611 could contribute. In the case of Westerlund 2, containing a Wolf-Rayet binary system, a part of the emission could come from the colliding winds. In both cases, the emission could be explained by shocks between the winds from massive stars.

1.2.3 More astrophysics in the VHE range

The source classes discussed previously are all well established. While scientists try to develop and improve models to explain the emission from these known classes, others dedicate efforts to discover new classes of sources. Indeed, a considerable part of the efforts from TeV experiments is dedicated to indirect dark matter searches. For example, neutralinos annihilating into gamma rays could potentially be detected by TeV experiments. Gamma-ray bursts, short flashes of intense ($\sim 10^{52}$ erg) luminosity in the soft and HE energy bands, are also investigated at TeV energies. No GRBs have been detected to date in the VHE range, but efforts are made to improve the telescopes to respond faster to GRB alerts, in order to perform observations in the seconds following the alert.

CHAPTER 2
Gamma-ray detection technique

VHE gamma-ray astrophysics uses observation techniques that are quite different from observations at any other wavelength. In this chapter, the detection technique will be described, including the imaging and gamma-ray identification methods. In Chapter 4, more details on the latter will be given where the analysis of VERITAS data is described.

2.1 Extensive air showers

At gamma-ray energies, photons are absorbed by the atmosphere. Therefore, telescopes need to be placed outside the atmosphere in order to receive the particles. Satellites are used to detect X-rays and low energy gamma rays. Nevertheless, satellites cannot be used for VHE gamma rays, simply because the TeV gamma-ray rates are too low. For example, the most powerful steady source in the northern hemisphere is the Crab Nebula, which produces $\sim 10^{-7}\gamma\mathrm{s}^{-1}\mathrm{m}^{-2}$ in the TeV regime. A satellite, with an area of a few m^2, would not be efficient to detect them, detecting $\sim$15 γs per year.

Fortunately, a particularity of VHE gamma rays allows us to detect them. Indeed, at TeV energies, gamma rays induce extensive air showers in the atmosphere and it is by detecting the Cherenkov radiation produced by these showers that gamma rays are detected. Details on the phenomena are given below.

2.1.1 Gamma-ray induced air showers

When gamma rays enter the atmosphere, the main radiative process that occurs is pair production. At high energy, the pair production process dominates over all others. As shown in Figure 2–1, the secondary particles (electrons and positrons) in the shower will then produce gamma rays via Bremsstrahlung radiation and these gamma rays will again undergo pair production. These chain reactions, cascades, will continue, producing lower and lower energy particles, until the radiative processes are dominated by ionization for the electrons and positrons and Compton scattering for the gamma rays.

There is a moment in the shower development when the number of particles present is a maximum: the shower maximum. The position of the shower maximum in the atmosphere depends on the energy of the incoming photon; photons with higher energy will create shower maximum deeper in the atmosphere. Gamma rays with energies of 100 GeV and 1 TeV will produce showers with the maximum at altitude (above sea level) of approximately 10 km and 8 km, respectively [173].

One characteristic of the pair production process is that the electrons and positrons are produced at a small angle relative to the incident gamma ray. Therefore, the electromagnetic shower is small in lateral size (see discussion below in Section 2.1.3) and the primary gamma-ray direction is preserved by the shower.

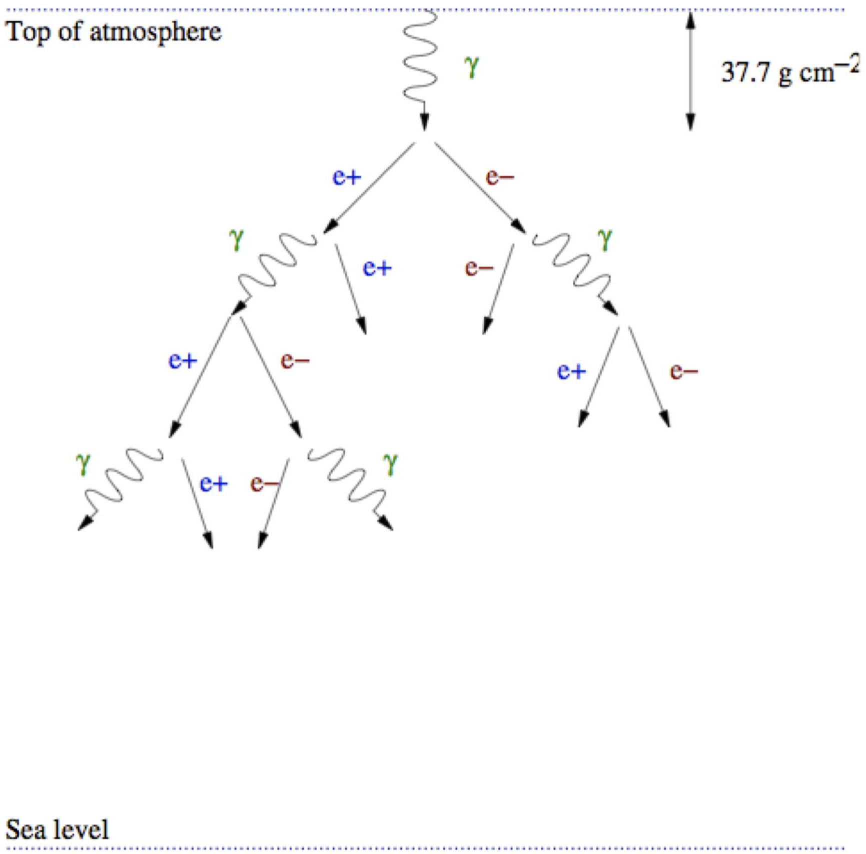

Figure 2–1: Schematic of the development of a gamma-ray induced shower. Figure taken from [63].

2.1.2 Cosmic-ray induced air showers

Cosmic rays are charged particles, such as protons, electrons, or ions. In the context of gamma-ray astrophysics, protons are of primary interest since they constitute around 90% of the cosmic rays. Electrons represent only 1% of the cosmic rays and their arrival directions are distributed isotropically. Heavier nuclei are also rare (less than 1%) and isotropic and they produce showers that are much more spread on the ground and they cannot be detected efficiently with the technique described in this chapter. Therefore, only proton-induced showers will be discussed.

When protons enter the atmosphere, they interact with other protons or nuclei present in the atmosphere. The interactions will create charged and neutral pions and other particles, such as muons, electrons and light atomic nuclei. Figure 2–2 illustrates schematically an example of a cosmic-ray induced shower.

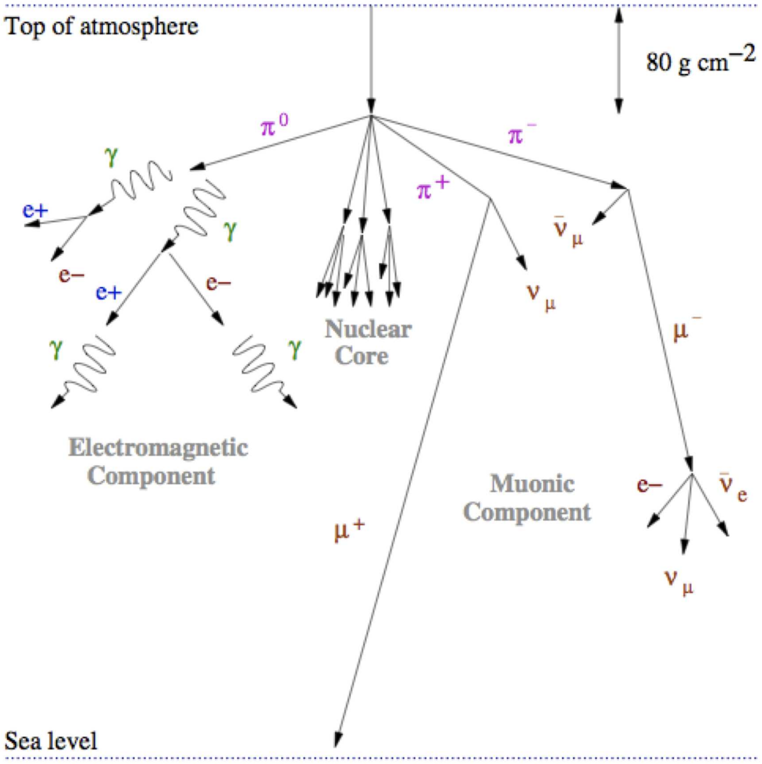

Figure 2–2: Schematic of the development of a cosmic-ray induced shower. Figure taken from [63].

The pions are responsible for electromagnetic sub-showers. Neutral pions will decay into two gamma rays, and the charged pions will decay into muons and neutrinos. In the first case, the secondary gamma rays will induce the pair creation process and in the second case, the muons will decay to electrons or positrons or propagate to the ground. Compared to gamma-ray induced showers, the cosmic-ray showers are much broader (see discussion below in Section 2.1.3).

2.1.3 Comparing cosmic-ray and gamma-ray induced air showers

The main observational characteristic that differentiates the air showers produced by gamma rays and cosmic rays is the lateral size of the showers. As shown in Figure 2–3, gamma-ray showers are much more compact. This can be seen as well in Figure 2–4, where a view of the Cherenkov photons on the ground is shown (Cherenkov radiation will be discussed in more detail in Section 2.1.4).

2.1.4 Cherenkov radiation from extensive air showers

When a particle passes through a medium while traveling faster than the speed of light (in the medium), Cherenkov radiation is emitted. In vacuum, light travels at a speed c, which is, from relativity principles, the maximum speed that a particle can reach. However, in a medium different than vacuum, light travels slower, with a speed indicated by Equation 2.1, where v_{light} is the speed of light in the medium, c the speed of light in vacuum and n the index of refraction of the medium:

$$v_{light} = c/n \tag{2.1}$$

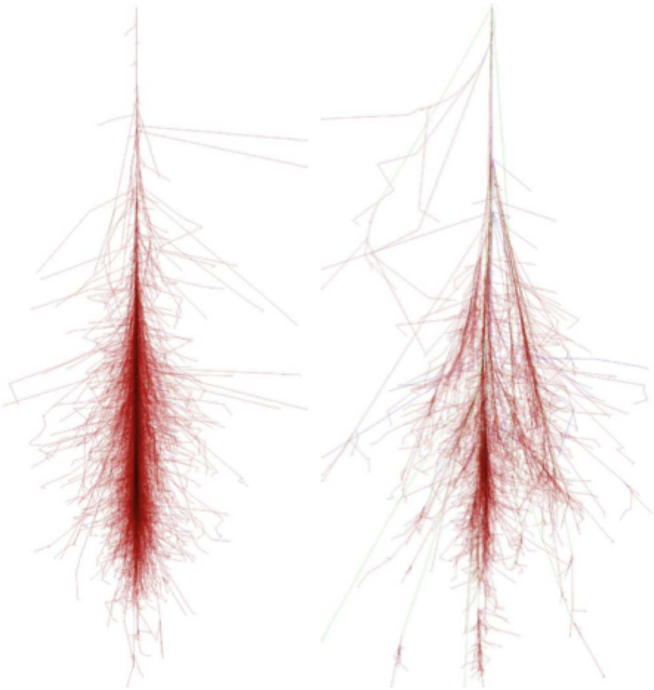

Figure 2–3: Simulated air showers produced by a 100 GeV gamma ray (left) and a 100 GeV proton (right). The vertical scale is 30 km and the horizontal scale is ±5 km around the shower core. Figure taken from [96].

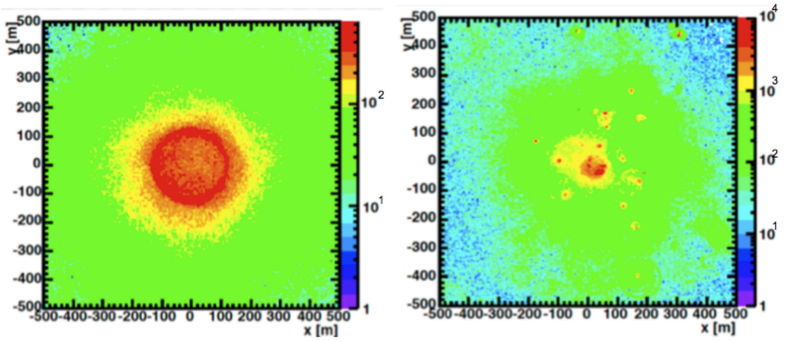

Figure 2–4: Left panel: Distribution of the Cherenkov photons on the ground for a gamma-ray induced shower. Right panel: Distribution of the Cherenkov photons on the ground for a cosmic-ray induced shower. The color scale represents the number of photons on the ground. Figures produced by Dr. G. Maier.

Thus, it is possible that the speed at which the particle is traveling is greater than the speed of light in the medium.

When a charged particle travels through a dielectric medium, the atoms of the surrounding medium become polarized. Once the particle has passed, the polarized atoms will relax by emitting a light pulse which lasts for a very short time (of the order of tens of ns). Depending on the speed of the traveling particle, the emitted light will differ. If the traveling particle is moving slowly ($v < v_{light}$), the polarization will be symmetrical along the path of the particle (see left panel in Figure 2–5). In this case, the radiation produced by the relaxation is not coherent and the radiation does not travel long distances. If the particle is moving fast ($v > v_{light}$), the polarization will become asymmetric along the path of the particle, as shown in the right panel of Figure 2–5. In this case, the emitted radiation is coherent, permitting emission over long distances. The coherent radiation emitted during the relaxation mentioned here is called Cherenkov radiation.

The coherent Cherenkov radiation is emitted as a wavefront, as shown in Figure 2–6. The wavefront is emitted at an angle θ_C with respect to the traveling particle. Since the particle is traveling at a speed $v > v_{light}$, in a time t, the particle will have reached a distance of vt, but the wavefront, traveling at v_{light}, will have reached $v_{light}t$, where $v_{light}t < vt$ (see Figure 2–6). It is geometrically easy to deduce the angle θ_C, expressed in Equation 2.2, where β is v/c:

$$cos\theta_C = \frac{1}{n\beta} \tag{2.2}$$

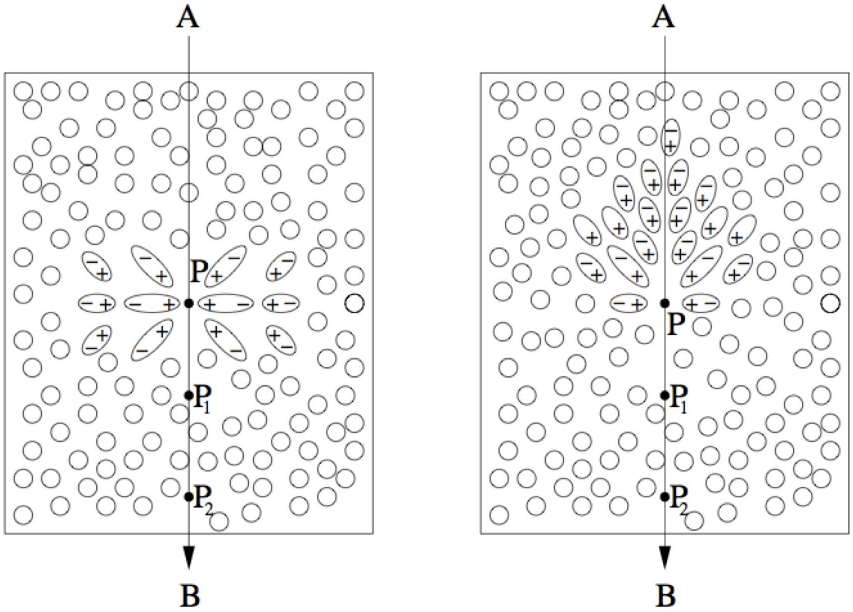

Figure 2–5: Polarization of the surrounding atoms from a particle traveling in a medium. Left panel: Case of a slow moving particle. Right panel: Case of a fast moving particle. Figure taken from [82].

From Equation 2.2, for a particle traveling in a medium of constant index of refraction, θ_C will stay constant. In addition, from the same equation, the energy threshold for a particle to create Cherenkov radiation can be deduced. Indeed, just below the threshold, $\theta_C = 0$ and $\beta = \frac{1}{n}$. The energy of the particle is therefore given by:

$$E_{threshold} = \gamma m_p c^2 = \frac{m_p c^2}{\sqrt{(1 - \frac{1}{n^2})}} \tag{2.3}$$

In the context of extensive air showers, Cherenkov radiation will be emitted by the shower particles as long as they have a speed $v > v_{light}$. In the case of gamma-ray induced air showers (see Section 2.1.1), since only electrons and positrons are

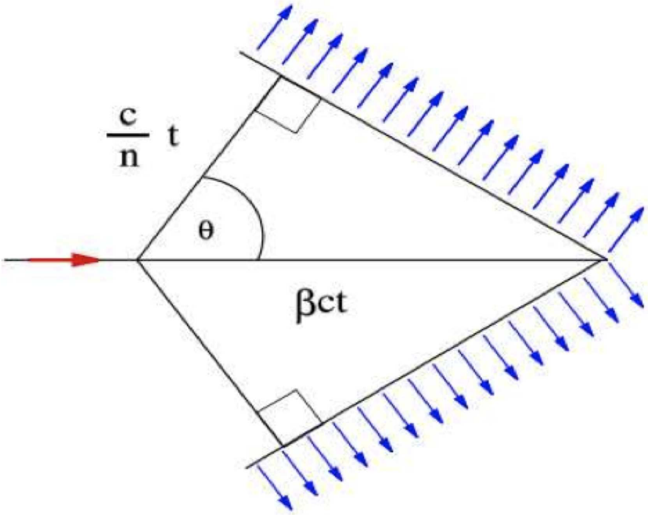

Figure 2–6: Schematic of the Cherenkov radiation emitted along the path of a fast moving particle.

produced in a compact shower, the Cherenkov emission will be compact, as seen in Figure 2–4. In the case of cosmic-ray induced showers (see Section 2.1.2), since several sub-showers are created, the Cherenkov radiation will be emitted along the main shower and sub-showers, leading to a less uniform distribution on the ground, as shown in Figure 2–4.

Since the density of the atmosphere changes with the height (being smaller at higher altitudes) the atmosphere's index of refraction changes as well. The index of refraction is smaller at higher altitudes. From Equation 2.3, it can be deduced that $E_{threshold}$ is higher at higher altitudes. Also from Equation 2.3, we see that $E_{threshold}$ increases with the mass of the particle. Therefore, more massive particles, such as muons or protons, necessitate higher energies to produce Cherenkov radiation when compared to electrons.

In opposition to radio or optical telescopes where photons are directly detected, Imaging Air Cherenkov Telescopes (IACTs) detect the Cherenkov radiation produced in the air showers induced by photons or cosmic rays, as shown in Figure 2–7.

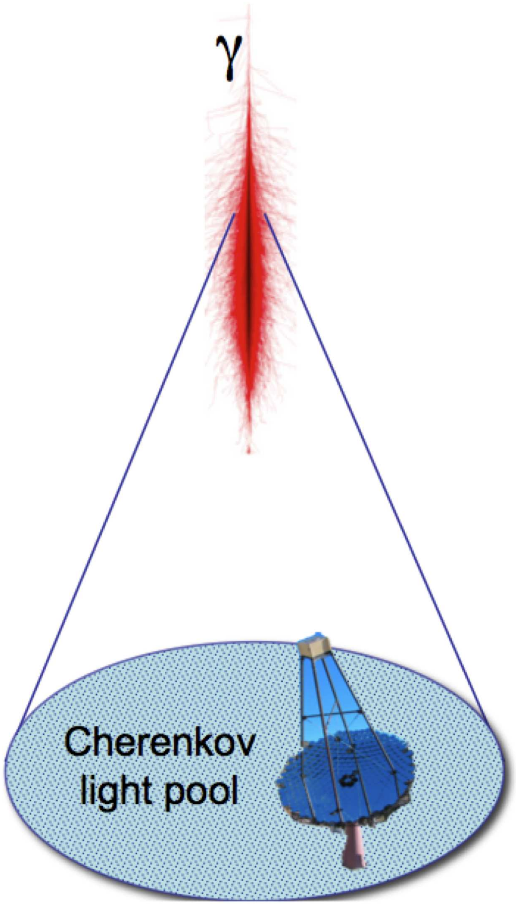

Figure 2–7: Schematic of a Cherenkov light pool created by a gamma-ray induced air shower with an air Cherenkov telescope.

The number of Cherenkov photons produced by a charged particle in the wavelength range [λ_1, λ_2] can be expressed by the following equation:

$$N = 2\pi\alpha l \left(\frac{1}{\lambda_2} - \frac{1}{\lambda_1}\right)\left(1 - \frac{1}{\beta^2 n^2}\right) \tag{2.4}$$

where α is the fine structure constant and l is the path length, assuming n constant. Typical values of interest for λ_1 and λ_2 for IACTs are approximately between 350 nm and 500 nm. These photons will be emitted along the shower in a cone of angle θ_C, as explained above. Figure 2–8 shows the Cherenkov emission schematically along an air shower. Most of the Cherenkov light is emitted at the shower maximum (between 6 km and 10 km), as seen in the lower panel of Figure 2–8. The Cherenkov light pool created has a radius of ~120 m. Therefore, a single incoming gamma ray can be detected in an area of~50 000 m^2. By detecting the Cherenkov radiation from air showers, IACTs have the immense advantage of increasing the effective collection area by several orders of magnitude, compared to satellites.

2.2 Imaging techniques

The flux of photons from the night sky background is $\sim 10^{12}$ photons $m^{-2}s^{-1}sr^{-1}$ [166]. In this background, the few hundred Cherenkov photons (see Equation 2.4) would be practically impossible to detect. However, the very short duration of the Cherenkov radiation makes the detection by telescopes possible. By looking for signals during a short time window, of order of tens of nanoseconds, and by selecting a small field of view, of the order of one or two degrees (which is comparable to the Cherenkov angle θ_C), the signal-to-noise ratio improves. Equations 2.5 and 2.6 give the number of detected Cherenkov photons from an air shower (S) and the number of photons detected from the night sky background (B).

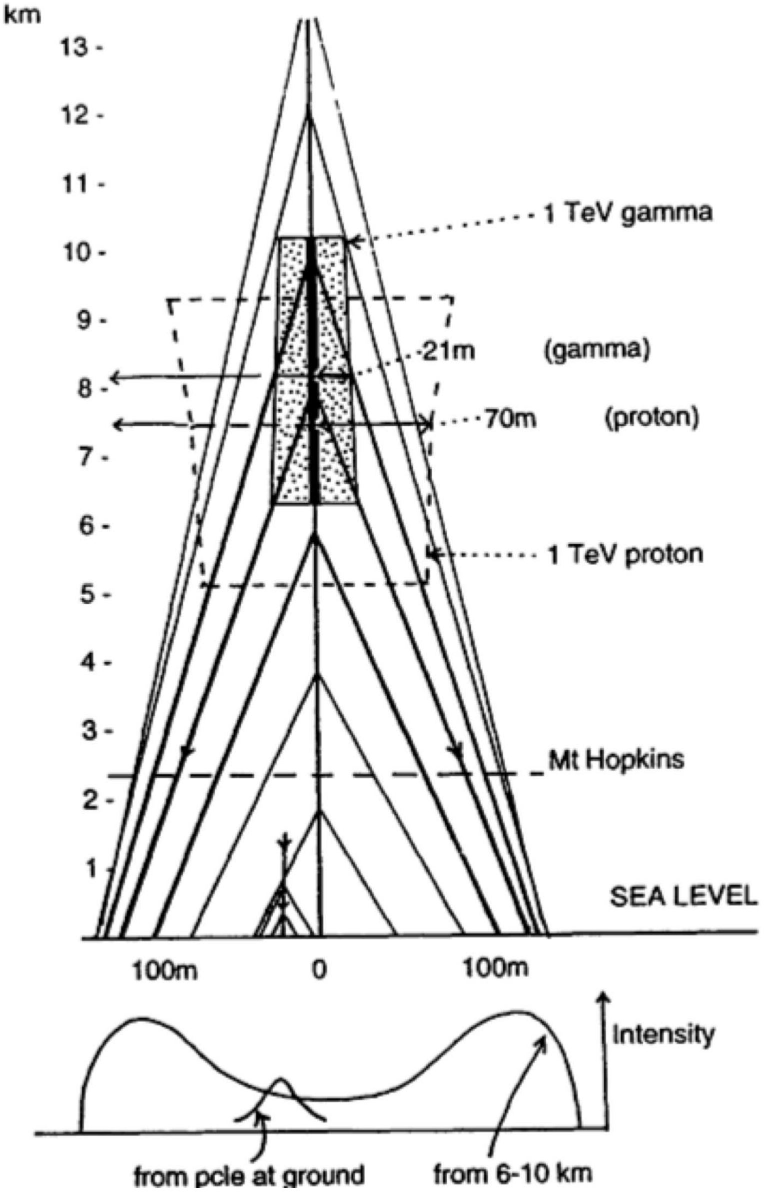

Figure 2–8: Cherenkov light distribution from an air shower. The grey box represents the region where the maximum of light is emitted by a gamma-ray shower. The dashed-line box represents the maximum emission region for a cosmic-ray shower of the same energy. The bottom panel shows the intensity of the Cherenkov light on the ground. Figure taken from [78].

$$S = \int_{\lambda_2}^{\lambda_1} C(\lambda)\eta(\lambda)A d\lambda \tag{2.5}$$

$$B = \int_{\lambda_2}^{\lambda_1} B(\lambda)\eta(\lambda)\tau A\Omega d\lambda \tag{2.6}$$

where $C(\lambda)$ is the Cherenkov photon flux, A is the collection area of the detector, $\eta(\lambda)$ is the efficiency of the photon detection, τ is the integration time and Ω the solid angle. From these two equations, the signal-to-noise ratio can be calculated:

$$\frac{S}{N} = \frac{S}{\sqrt{B}} = \sqrt{\frac{A}{\tau\Omega}} \frac{\int_{\lambda_2}^{\lambda_1} C(\lambda)\eta(\lambda)d\lambda}{\int_{\lambda_2}^{\lambda_1} B(\lambda)\eta(\lambda)d\lambda} \tag{2.7}$$

The last equation shows that minimizing the integration time (τ) and the solid angle (Ω) can increase considerably the signal-to-noise ratio up to detectable levels. In addition, the night sky background intensity is more important at longer wavelengths. Therefore, it is also an advantage to use photomultiplicator tubes (PMTs) that are sensitive to smaller wavelengths, where the peak of emission of Cherenkov radiation from air showers is located.

2.2.1 Imaging an air shower

It has been discussed previously how the Cherenkov photons are emitted along the air shower, having a maximum of emission intensity around 10 km altitude. Figure 2–9 shows an illustration of how an air shower is imaged by a telescope. The Cherenkov photons are collected by the reflector of the telescope and reflected and focused onto the focal plane of the camera, where PMTs will detect them.

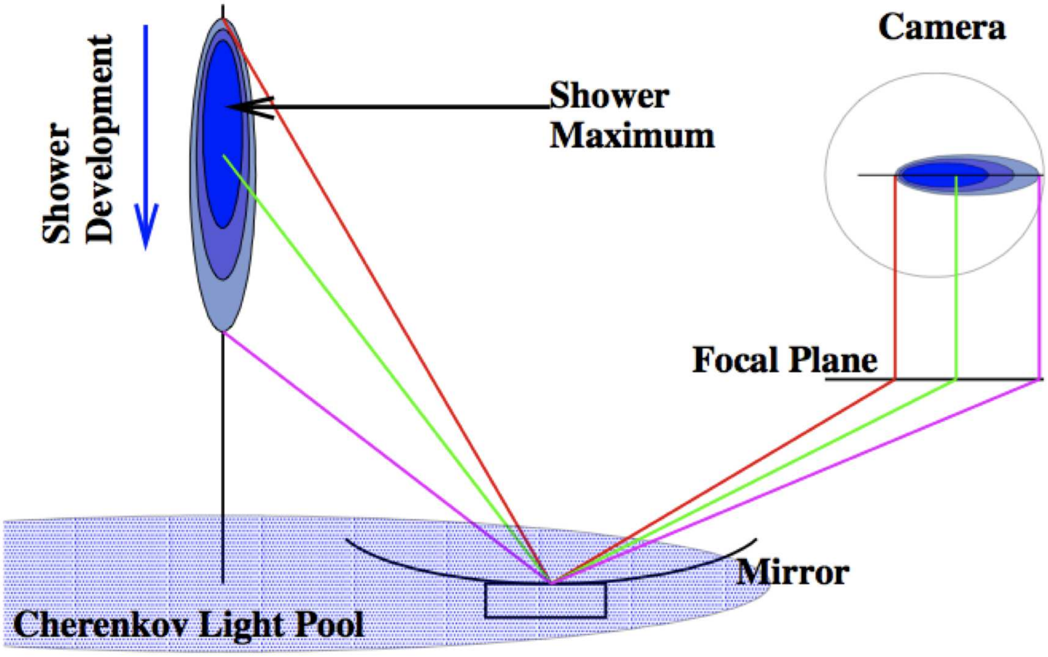

Figure 2–9: Illustration of how gamma-ray air showers are imaged by IACTs. The Cherenkov light is collected by the reflector and focused onto the focal plane of the camera. Figure taken from [32].

2.2.2 Characterization of the images

As mentioned in section 2.1, both gamma rays and cosmic rays induce extensive air showers that produce Cherenkov radiation. The flux of cosmic rays is several orders of magnitude higher than the gamma-ray flux. It is therefore crucial to be able to distinguish between images from gamma rays and those from cosmic rays. Qualitatively, since air showers produced by gamma rays and by cosmic rays are different (see Section 2.1.3), distinctions between the two images can be made. Figure

2–10 shows a cartoon illustrating images from a cosmic-ray air shower and from a gamma-ray air shower. The image from the gamma-ray shower is much more compact and shaped like an ellipse. The cosmic-ray image is broader and less uniform.

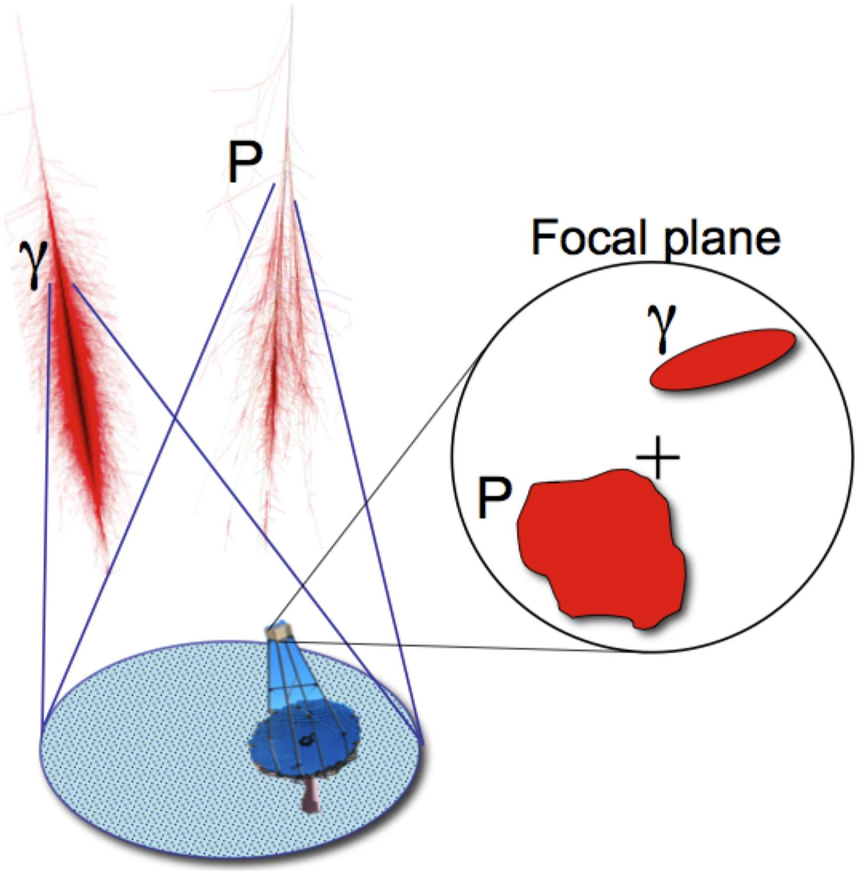

Figure 2–10: Schematic illustration of the appearance of gamma-ray and cosmic-ray (proton (p)) induced showers in a IACT camera.

In order to distinguish the cosmic-ray images from gamma-ray images, a technique has been developed to characterize the images. This technique consists of fitting an ellipse to the recorded images; as mentioned above, the gamma-ray images have roughly elliptical shapes. From the fitted ellipse, a set of parameters, called Hillas parameters [77], are defined. Figure 2–11 shows the different parameters. The source position can be determined using the fitted major axis. Indeed, with arrays of more than one telescope, the intersection of the major axes from the images of all telescopes indicates the position of the source in the camera (more details in Section 2.2.3).

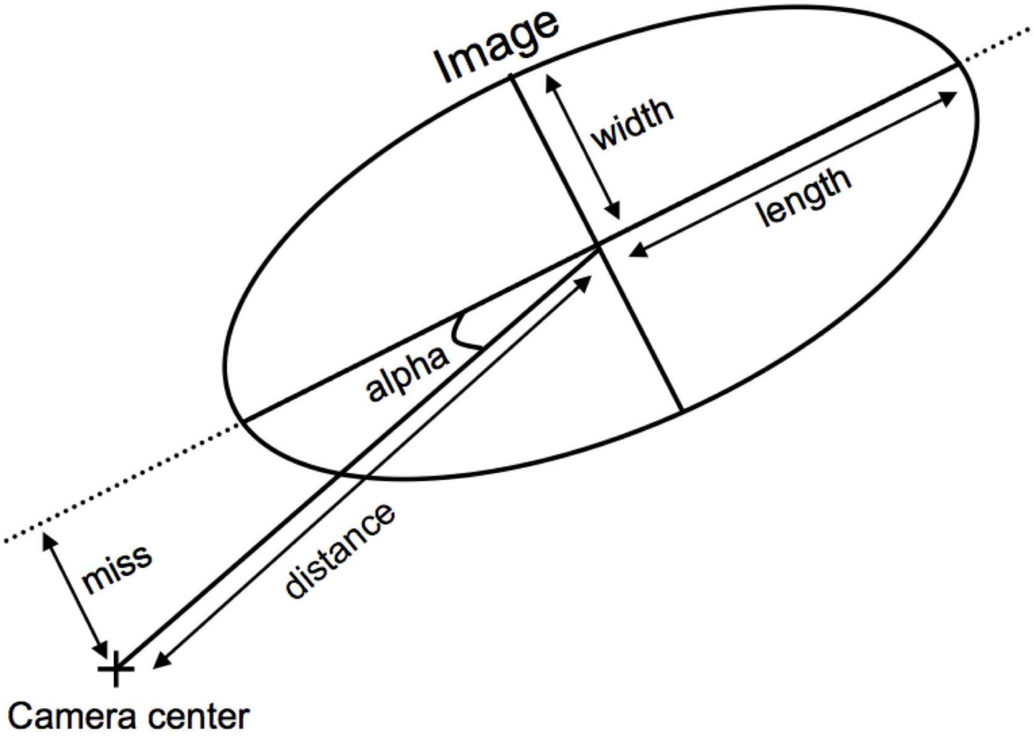

Figure 2–11: Schematic representation of the Hillas parameters of an image fitted by an ellipse.

Here is a description of each Hillas parameter:

size: Total integrated charge of all the pixels in the fitted ellipse (not shown in Figure 2–11). It corresponds to the size of the shower (measured either in digital counts or photo-electrons), and therefore relates to the energy of the incoming particle.

distance: Angular distance (in °) between the center of the camera and the fitted image centroid.

width: Angular length (in °) of the semi-minor axis of the fitted ellipse. It represents the spread of the image along the minor axis and corresponds to the lateral size of the shower as viewed from the ground.

length: Angular length (in °) of the semi-major axis of the fitted ellipse. It represents the spread of the image along the major axis and corresponds to the vertical size of the shower as viewed from the ground.

alpha: Angle (in °) between the fitted major axis and the direction to the center of the field of view.

miss: Perpendicular (angular) distance between the fitted major axis and the center of the camera.

Each of these parameters has a role to play in the discrimination against background (cosmic-ray induced) events. The first cuts to be applied to reject cosmic-ray events use the *length* and the *width* parameters. Figure 2–12 shows the distributions of the *length* and the *width* parameters for gamma-ray events and for cosmic-ray events from simulations[1] and data. In fact, the distributions show the mean scaled parameters, which relate directly to the *length* and the *width* parameters (see Section 4.2.6 for details on the mean scaled parameters). The distributions are different and cuts can be applied to reject a substantial part of the cosmic-ray background while accepting most of the gamma-ray events.

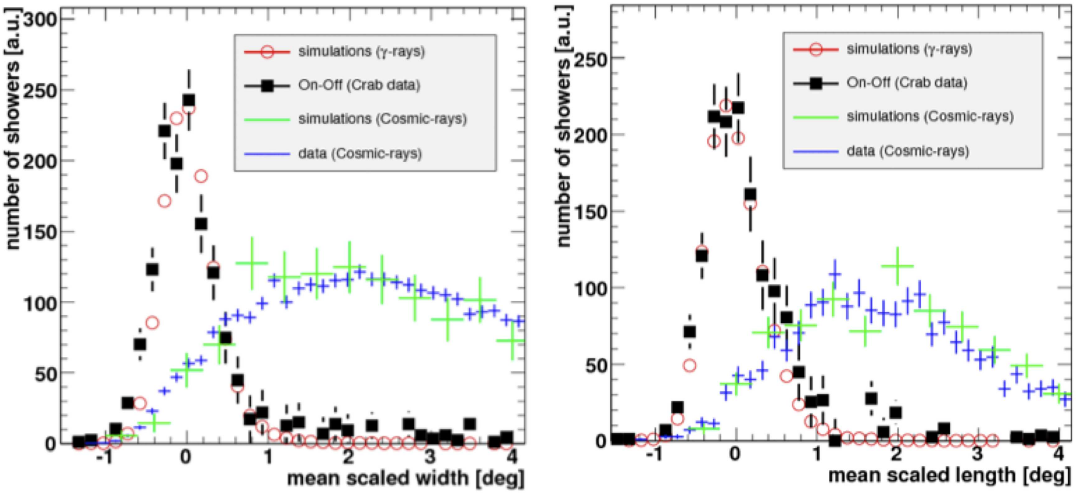

Figure 2–12: Distributions for the *width* parameter (left panel) and the *length* parameter (right panel) from cosmic-ray simulations (green crosses) and data (blue crosses), gamma-ray simulations (red open circles) and data (black squares). Note that it is the mean scaled parameters that are shown here (see Section 4.2.6 for details).

The *alpha* parameter can be used to further reject cosmic-ray events that pass the two previous cuts. This parameter allows one to cut images that do not align with the expected position of the source, from the fitted major axis direction. As

---

[1] Details on the simulations used by TeV experiments will be given in Chapter 3.

shown in Figure 2–9, the major axis of the ellipse fitted to the image reconstructs to the direction of the shower. During observations, the telescopes are pointed to an astrophysical source; thus, the incoming gamma rays from the source lead to ellipses pointing (in the camera) towards the source. In the case they do not, the event is rejected. Figure 2–13 shows an example of an *alpha* distribution produced from simulated protons and gamma rays.

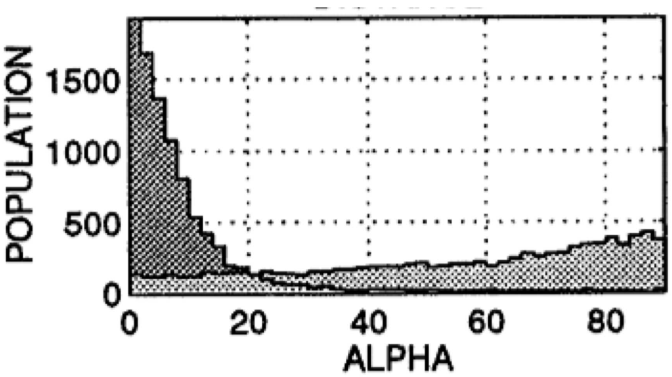

Figure 2–13: Typical alpha distribution from simulations of gamma rays (black histogram) and cosmic rays (grey histogram). Figure taken from [55].

2.2.3 Images from arrays of telescopes

The detection and identification of gamma-ray showers are improved by using an array of telescopes (called a "stereo"array even if there are more than two telescopes). By having more than one telescope, the reconstruction of the source position in the camera is much easier and more accurate. Figure 2–14 shows an illustration of how a shower is reconstructed in an array of telescopes that detect the shower. The multiple images in the combined camera all point towards the same location: the source position. A better reconstruction will affect several characteristics of the experiment performance. These characteristics are described below, as well as how they are improved by stereo observations.

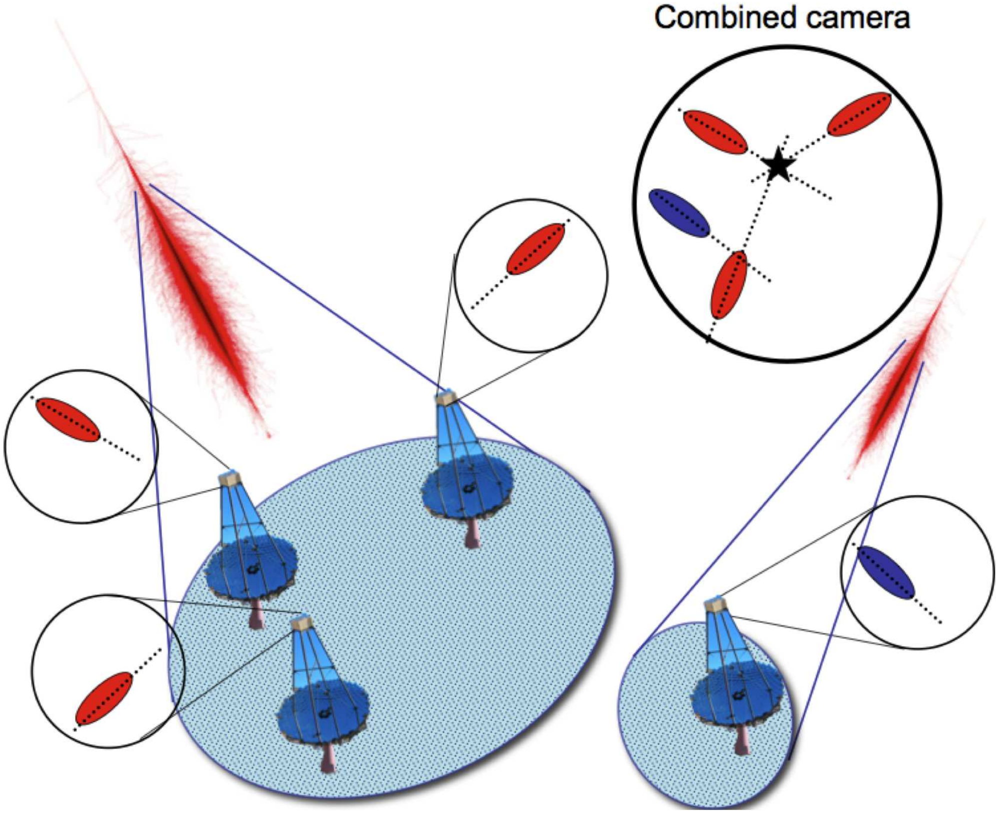

Figure 2–14: Illustration of how multiple telescope array images are seen in the cameras. Note that the blue image does not come from the same shower as the red images; the fitted major axis does not intersect with the others. The combined camera shows how the major axes of the three red fitted ellipses coming from the same shower intersect at a point (star), giving the position of the source in the camera.

Angular resolution

The angular resolution represents the capacity to resolve the position of the gamma-ray source. A gamma ray emitted from an astrophysical source does not deviate from its trajectory (magnetic fields do not affect gamma rays). In addition, as explained in Section 2.1.1, the air shower produced by the gamma ray conserves the direction of the trajectory. Therefore, from the images recorded by the telescopes, the direction of the gamma ray can be reconstructed (using the major axis of the ellipse, as described above). By having more than one telescope, the angular resolution is improved considerably. Indeed, Monte Carlo simulations show that one telescope of the VERITAS design can achieve an angular resolution of about $0.1°$ while an array of four telescopes can achieve around $0.05°$.

Energy resolution

The energy of an incoming gamma ray can be determined by using the *size* of the shower, *i.e.* the amount of light produced in the shower. More energetic gamma rays will produce bigger (therefore brighter) showers. This is because the number of secondary particles produced in a shower (and therefore the number of Cherenkov photons) is proportional to the energy of the incoming particle. In the analysis, the energy is determined by comparing the recorded images with Monte Carlo simulations (see Section 4.2.7). The energy resolution, which is the capacity of reconstructing the energy from the shower, is improved as more light from the shower is collected. By using stereo observations, the light collected is increased, and therefore, the energy resolution is improved. In addition, since the position of the shower is better reconstructed by the telescope array (see previous section), the relation between the size of the shower and the energy is better defined. Indeed, a small size shower could be produced either by a low energy shower or a higher energy shower that is more distant. Energy resolution for a single telescope (such as the Whipple telescope) is of the order of 30% [130], while for a telescope array, such as VERITAS, the energy resolution is $\approx$ 10-20% [123].

Muon background rejection and energy threshold

By convention, the energy threshold of a Cherenkov telescope is defined as the energy at which the differential rate (γ rays per minute per unit of energy) of reconstructed gamma-ray showers is at its maximum. One difficulty in the energy reconstruction is the presence of muons (sub-products of cosmic-ray showers). These muons, produced in the showers at altitudes less than a few km, travel at a constant high speed in the atmosphere. At these low altitudes the index of refraction of the atmosphere is almost constant, and Cherenkov light is emitted with a constant angle θ_C. The images produced by muon showers look like rings (see Figure 2–15). The problem with muons is that when they impact the ground far from the telescope (but close enough that part of the Cherenkov light pool is detected), the ring will be truncated. This truncated image might in some cases look similar to a small gamma-ray shower and will pass the selection cuts. Therefore, one has to raise the trigger or analysis threshold to reject them. Figure 2–15 illustrates how a muon falling further and further from the telescope appears in the camera. Stereo observations are very efficient at discriminating the muons. Indeed, a truncated image from a muon in one telescope, looking like a small gamma-ray shower, will look like a more complete ring in a telescope located closer to the impact point of the muon, and therefore will be rejected by the selection cuts. In the case of a muon falling outside the array, where only one telescope can detect the Cherenkov light, a trigger system requiring that an event be seen in more than one telescope will reject the shower (see Section 3.2.1 for more details of the VERITAS array trigger). The energy threshold of a single telescope is around 200 GeV while for an array like VERITAS, it is around 100 GeV, showing clearly the advantage of stereo observations.

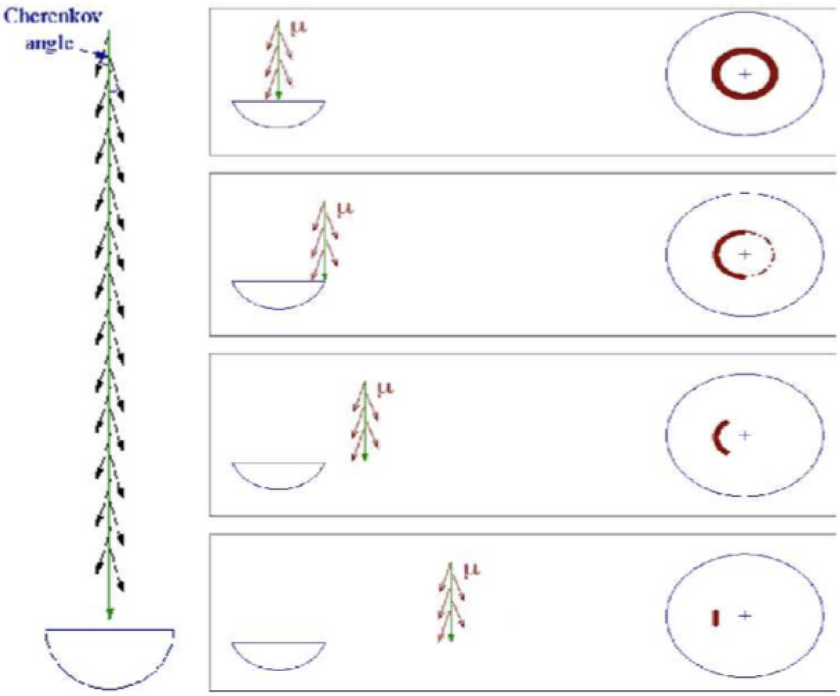

Figure 2–15: Illustration of images produced by muons. When the muon impacts the ground outside the telescope, the ring appears truncated in the camera, to a point where identification as a ring is impossible. Figure taken from [82].

CHAPTER 3
The VERITAS experiment

The VERITAS experiment is an array of four telescopes designed to detect VHE gamma rays using the detection technique described in the previous chapter. The array is located at the basecamp of the Fred Lawrence Whipple Observatory in Arizona, USA (latitude +31°40'30", longitude -110°57'7"). Figure 3–1 shows a picture of the VERITAS array in late 2009. The first telescope was built in early 2005, the second one in early 2006 and the third one at the end of 2006. The array of four telescopes became fully operational in Fall 2007. In the summer of 2009, one of the telescopes was moved to provide a more symmetrical array and a higher sensitivity. Figure 3–2 shows a schematic illustration of the new array layout. In this chapter, the telescopes as well as some measurements performed to monitor the experiment will be described in detail.

3.1 The telescopes

3.1.1 The reflector

The VERITAS telescopes are 12 m diameter Davies-Cotton reflectors [35], composed of several mirror facets and are spherical in order that all the individual focus points (F) of the facets are focusing at the same point, which is 2F. The right panel

Figure 3–1: View of the VERITAS array with the new array layout. Photo credit: S. Criswell, FLWO.

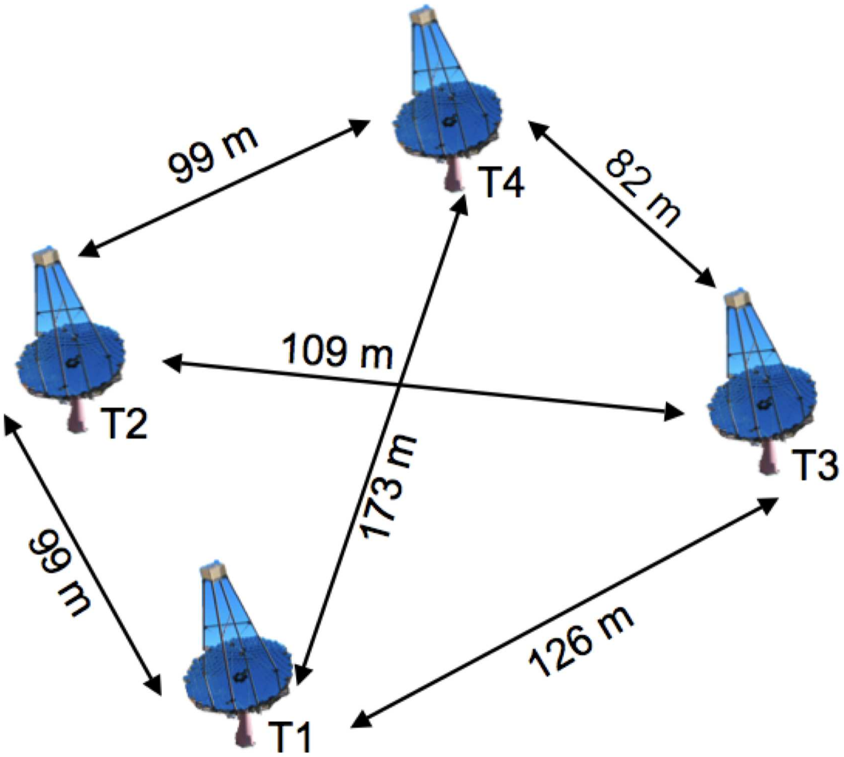

Figure 3–2: Illustration of the new VERITAS array layout.

of Figure 3–3 shows a diagram of the Davies-Cotton design. The mirror facets are attached to a 12 m diameter optical support structure (OSS), as shown in the left panel of Figure 3–3. The OSS is supported by an altitude-azimuth positioner mount. The positioners have a pointing accuracy of $\leq 0.005^\circ$ and can be driven at speeds up to 1°/s.

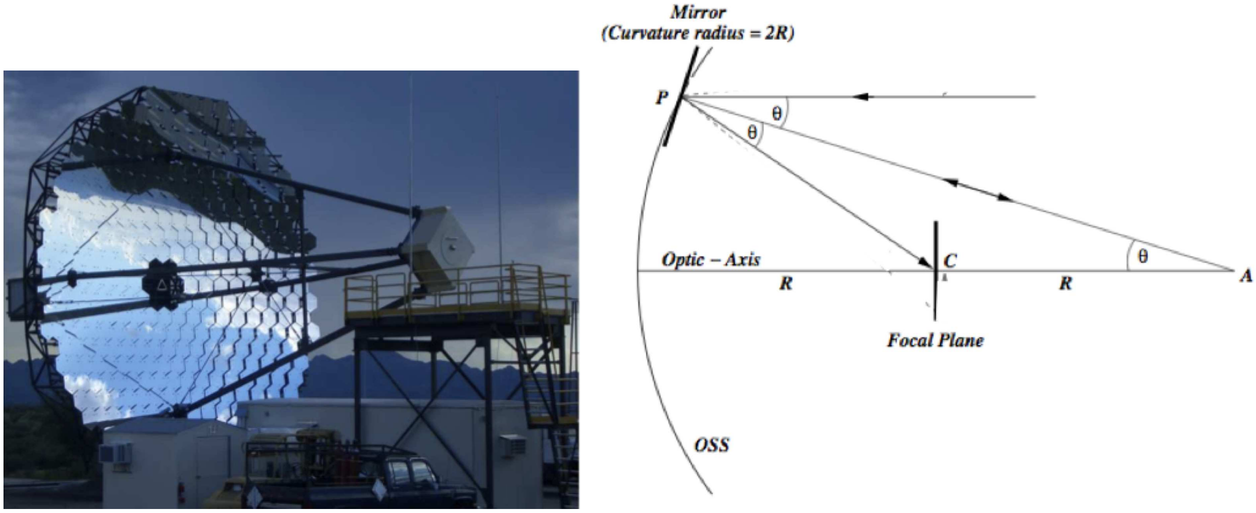

Figure 3–3: Right: Diagram of the Davies-Cotton reflector design. Figure taken from [113]. Left: View of one of the VERITAS telescopes (T4).

The VERITAS reflectors are composed of 345 hexagonal mirror facets (61 cm diameter and 11.5 mm thickness) fixed to the OSS with three sets of screws to allow alignment. This gives a total reflector area of 110 m^2. The mirrors are front-aluminized (180 nm thick layer of aluminum) and anodized (80 nm thick layer). The anodization consists of converting the top layer of aluminum into aluminum oxide. The front coating is necessary to avoid absorption of the UV light by the glass of the mirrors and the anodizing, in addition to protecting the mirror against degradation from the ambient conditions, allows the peak of reflectivity to be in the region where Cherenkov emission is higher (see left panel in Figure 3–4). The reflectivity of the facets at a wavelength of 320 nm is around 92% (see right panel in Figure 3–4). The facets are cleaned every few months. The mirrors lose around 3% reflectivity per year at 320 nm [148]. To ensure optimal operation of the array, the mirrors are re-coated and re-anodized periodically. The mirror facets need to be aligned every time they are taken off the OSS. In Section 3.3.1, the mirror alignment method is described.

Each mirror facet has a nominal radius of curvature (C) of 24 m [148] (see right panel of Figure 3–4). Therefore, the focal length f of the facets is 12 m ($f = C/2$). The focal length of the whole reflector is 12 m (see Figure 3–3).

3.1.2 The camera

The cameras are located at the focal points of the telescopes (12 m from the center of the reflectors). On each telescope, the Cherenkov light focused by the reflector is collected by 499 PMTs (pixels) (see Figure 3–5). Each PMT has a diameter of 29 mm, corresponding to a field of view of 0.15° on the sky. The entire camera has a field of view (FOV) of 3.5°. The PMTs (Photonis XP2970/02) have a quantum efficiency of ∼25% at a wavelength of 320 nm. They are operated at a gain of $\sim 2 \times 10^5$ (typical voltage is ∼850 V). The PMTs are attached to preamplifiers which provide an amplification factor of 6.6.

A set of light cones, such as the ones shown in Figure 3–6, is placed in front of each camera, covering the entire camera. This is to increase the light collection (by a factor of up to 75%), since the PMTs are round in shape and the tiling creates many

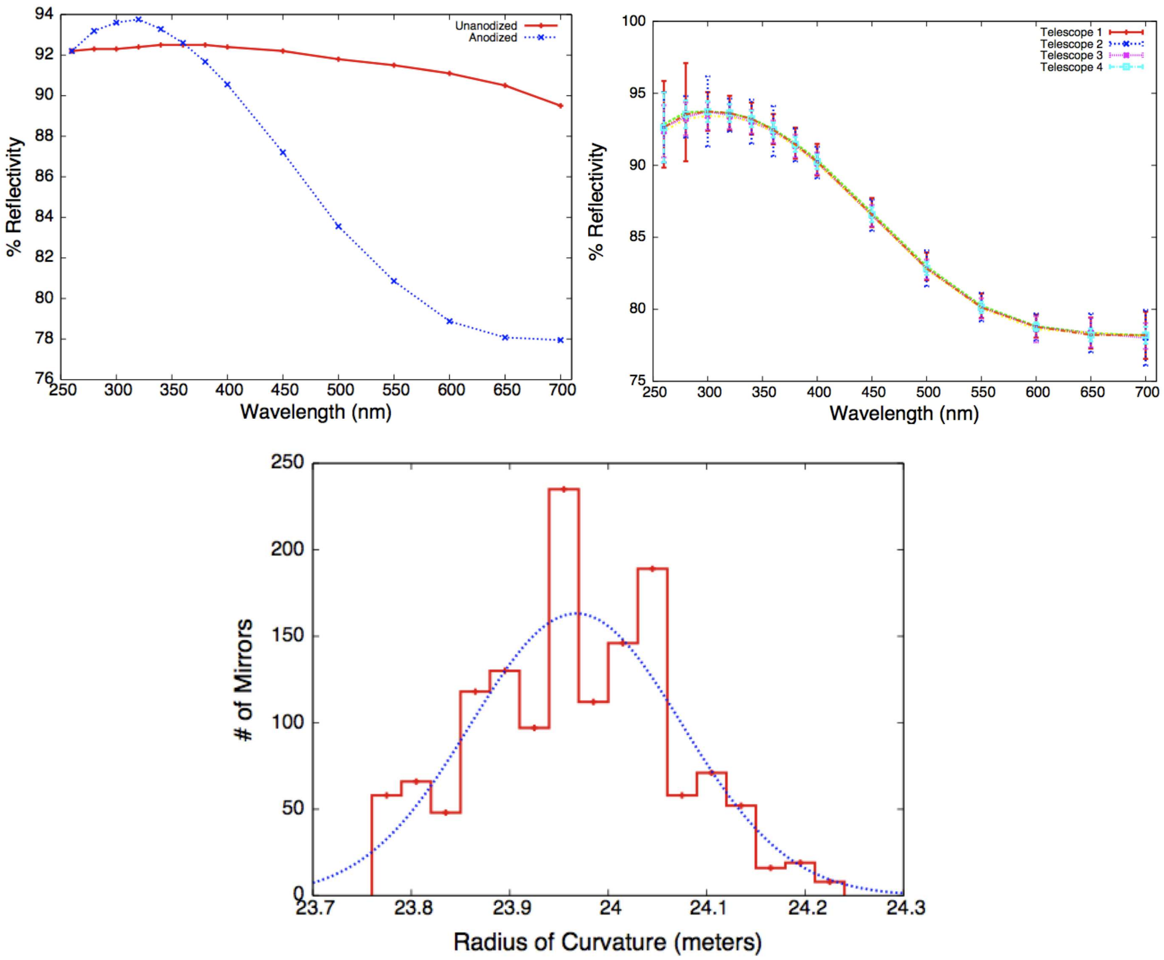

Figure 3–4: Upper left panel: Mirror reflectivity as a function of wavelength. The red curve (+ points) show un-anodized mirror reflectivity and the blue curve (× points) show the anodized mirror reflectivity. Upper right panel: Mirror reflectivity of each VERITAS telescope as a function of wavelength. Lower panel: Histogram of the radius of curvature of the VERITAS mirrors. The mirrors have an average radius of curvature of 23.97 ± 0.01 m (from the Gaussian fit (dotted curve)). Figures taken from [148].

gaps (see Figure 3–5). The light cones have a reflectivity higher than 85% above 260 nm. They are cleaned approximately every month.

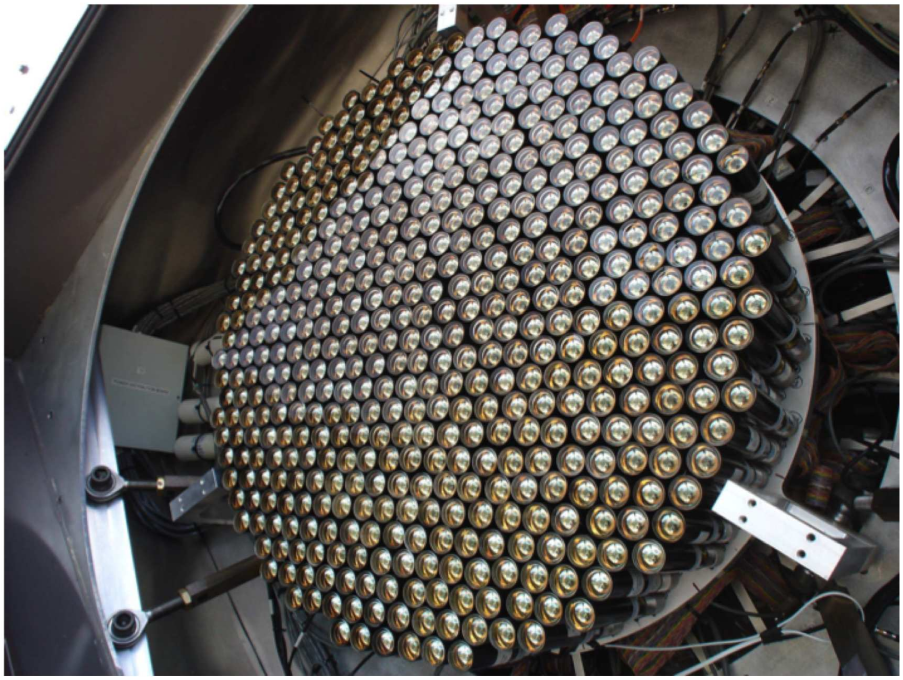

Figure 3–5: A VERITAS camera, composed of 499 PMTs. Picture taken from [166].

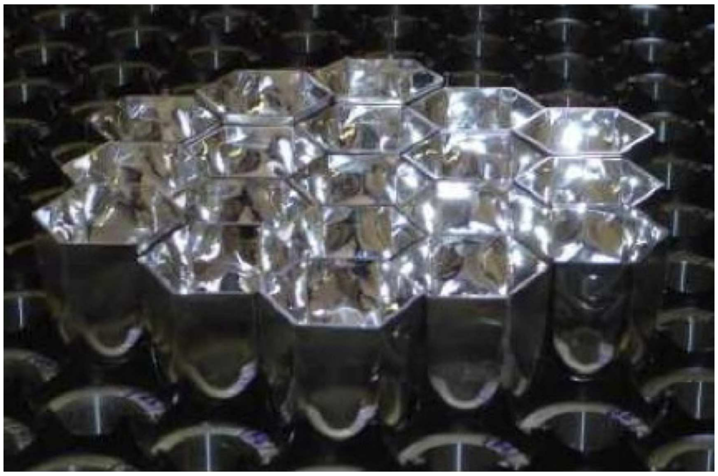

Figure 3–6: A group of light cones placed over the PMTs.

3.2 The data acquisition system

When the photons hit the PMTs, an analog electrical signal is produced. The signal is sent directly to the Flash Analog to Digital Converter (FADC) boards where it is stored, until a trigger decision is made to record or reject the event. A copy of the signal sent to the FADCs is sent to the trigger system for acceptance or rejection. If the event passes the trigger decision, a signal is sent to the FADCs to record the event. This process takes less than 100 ns. The FADCs have a rate of 500 MHz (2 ns samples). The readout window is typically 20 to 24 samples long, to ensure that it contains the whole Cherenkov pulse (a typical Cherenkov pulse lasts less than 20 ns). The 499 pixels of each telescope are read out by 50 FADC boards.

In order to record only events that might be of interest for the analysis (*i.e* no night sky background fluctuations), a three level trigger system, described below, is used to select the events. Figure 3–8 shows a schematic illustration of the trigger system

3.2.1 The 3-level trigger system

L1 trigger: CFD

The L1 trigger is at the pixel level. In order to pass the first level trigger, a pixel has to detect an amount of light (pulse height) higher than a defined threshold (see Section 3.3.2). This threshold is in units of voltage. The L1 decision is made by the Constant Fraction Discriminators (CFDs); every pixel has its own CFD. The decision is made on the copy of the signal sent to the FADCs.

The signals received by the CFDs are split into three copies. One copy is sent to the discriminator, to test if the pulse amplitude is above the threshold (this threshold is discussed further in Section 3.3.2). The two other copies of the signal are used to time the signal trigger. For example, two pulses having different amplitudes will cross the voltage threshold at different times, and therefore the trigger time will be different for the two pulses. The trigger time needs to be the same for all pulses in order to record the event in all pixels. This is done using the two copies. One copy is delayed and inverted and the other copy is attenuated. These two signals are sent to a Zero Crossing Discriminator (ZCD) which combines the pulses and finds the time where the two pulses cancel, as shown in Figure 3–7. It is at the point of zero crossing that the CFD trigger is sent.

L2 trigger: Pattern trigger

Night sky background fluctuations could trigger the CFD threshold on some pixels. It is therefore important to have criteria that will reduce the probability of triggering on such random fluctuations in the night sky. The fluctuations can appear anywhere in the camera, contrary to an air shower signal which would typically trigger pixels close to each other. The L2 trigger is designed to identify regions where at least 3 adjacent pixels have triggered the CFDs in a given time window (usually 6 ns). The L2 modules receive the L1 signals and look through pre-loaded pixel patterns of adjacent pixels. The L2 system divides the camera into 19 patches and searches through all possible 3-pixel patterns for each patch. When all the pixels corresponding to a specific pattern have triggered their corresponding L1 CFDs, an L2 trigger is generated. Each telescope has a separate L2 trigger system.

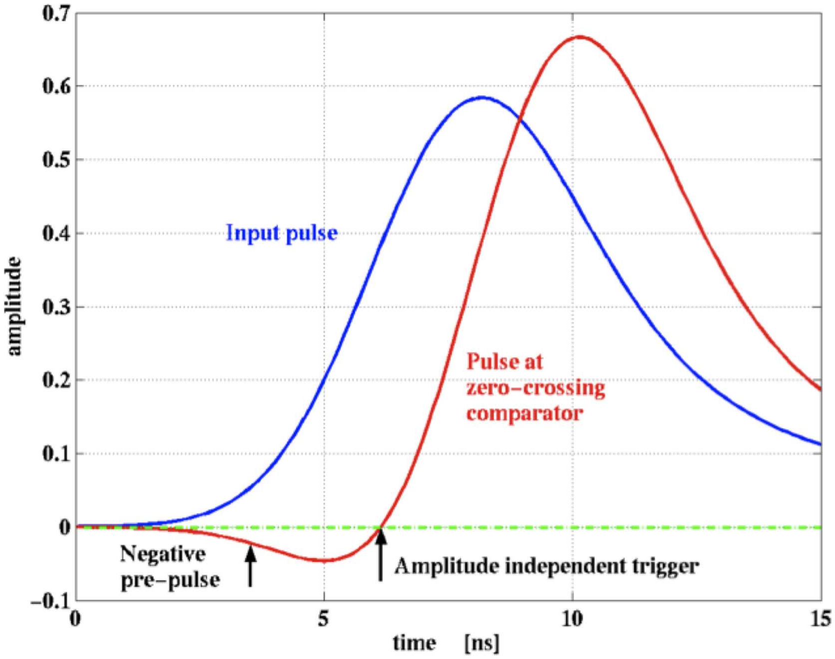

Figure 3–7: Illustration of the ZCD principle. The attenuated copy of the signal is added to the delayed and inverted copy (creating the red pulse, magnified here for clarity). The point of zero crossing is indicated by the second arrow. The input pulse (blue curve) is shown for comparison. Figure taken from [97].

L3 trigger: Array trigger

In Section 2.2.3, it was shown that isolated muons can generate Cherenkov light that can mimic gamma-ray showers. The muons Cherenkov cone generally satisfy the L2 trigger of a telescope when the impact parameter of the muon is small (∼25 m). However, the muon usually trigger the L2 of only one telescope at a time (the distances between the telescopes being $\gtrsim$ 80 m (see Figure 3–2)). The L3 trigger is designed to avoid triggering on muons. By using an array trigger that requires more than one telescope to generate a L2 trigger, a large fraction of the muons do not trigger the data acquisition system.

In order to pass the L3 trigger, at least two telescopes must generate a L2 trigger. All L2 trigger signals are sent to the L3 computer and are delayed by an amount of time that accounts for different cable lengths and different Cherenkov light arrival times between the telescopes. The L3 computer looks for coincidences between L2 triggers in a defined and programmable time window (usually 100 ns). When at least two telescopes have coincident L2 signals, the L3 trigger is generated and sent to all telescopes, and the event is recorded by all telescopes. During the time when the telescopes are receiving the L3 trigger and recording the event, the trigger system is stopped (dead-time). The experiment dead-time is of the order of 10% to 15%.

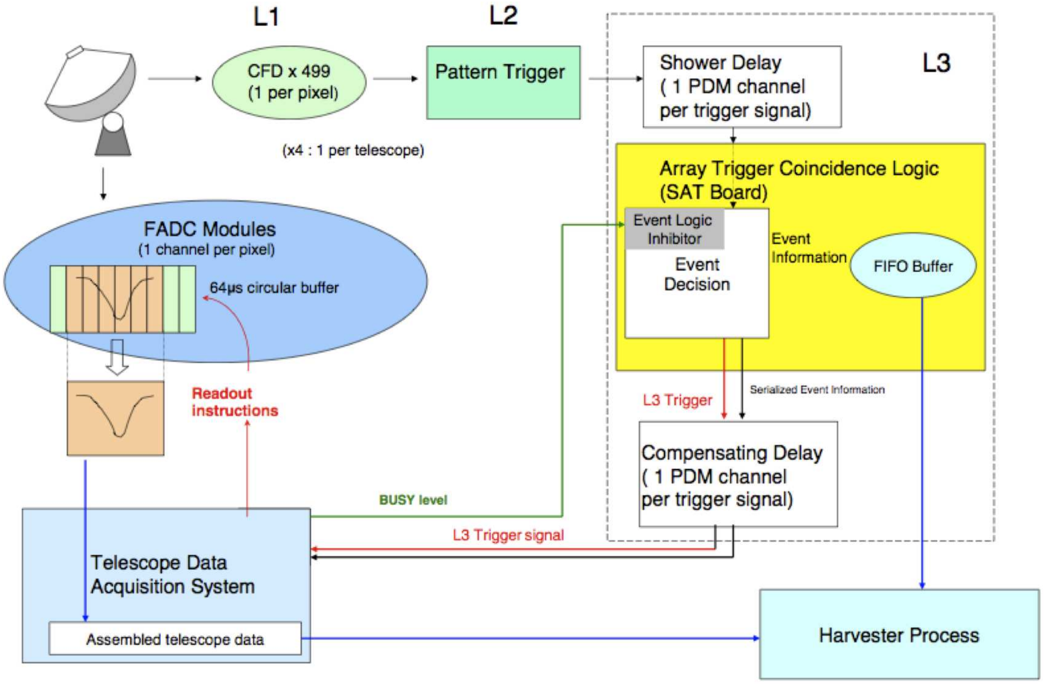

Figure 3–8: Schema of the VERITAS 3-level trigger system. Figure taken from [175].

3.2.2 Data processing

For each telescope, the data acquisition system is completed by four VME crates holding the 50 FADC modules and by an auxiliary crate. The latter holds the clock trigger module and the Global Positioning System (GPS) clock. A set of Pulse Delay Modules (PDMs), which add delays to the L2 or L3 trigger signals, and a SubArray Trigger (SAT) board, which performs the majority of the critical array trigger functions, are also part of the data acquisition system. The VME crates retrieve the data recorded by the FADCs by extracting data from a window of programmable length (typically 20 to 24 2-ns samples). The telescope information is then sent to the event builders (one per telescope), which assemble the data (pulses from each crate and time stamp information from the auxiliary crate) to create a telescope event and write it on disk. Figure 3–8 shows a schematic summary of the system.

Finally, the harvester computer takes the telescope events from each event builder to create a single data file for the array. The harvester stores the information in a format custom designed for VERITAS data, VERITAS Bank Format (VBF). These files are then sent to the data archive for offline analysis.

3.3 Calibrations for VERITAS

In order to understand the telescopes and to maintain their performance, a series of measurements and calibrations are performed regularly. In this section, some of these measurements will be described as well as their impact on VERITAS performance.

3.3.1 Mirror alignment

Since the VERITAS reflectors are composed of hundreds of mirror facets, it is crucial, in order to collect as much Cherenkov light as possible, that the facets be well aligned. Until 2009, the alignment was done using a helium-neon laser that was placed at a distance of twice the focal point of the facets (*i.e* 24 m). The laser was directed at each facet individually. To do the alignment, each facet was adjusted (using the three sets of mirror-alignment screws) until the reflected beam of light was coincident with the incident beam. This process was tedious and needed to be done everytime the facets were removed.

At the beginning of 2009, a new alignment tool was developed by A. McCann and D. Hanna [127]. This new tool consists of a digital camera mounted at the center of the telescope focal plane. To perform the mirror alignment, successive images of the reflector are taken by the digital camera, while the telescope performs a raster scan centered on a bright star. The analysis gives precise adjustment values for each set of mirror-alignment screws for each facets.

Figure 3–9 shows the point spread function (PSF) before and after the mirror alignment with the new tool. The improvement in the size of the PSF is considerable, and very important for gamma-ray analysis. A smaller PSF results in a superior angular resolution, important for source identification in crowded fields, and for extension measurements of non-point astrophysical sources, such as supernova remnants.

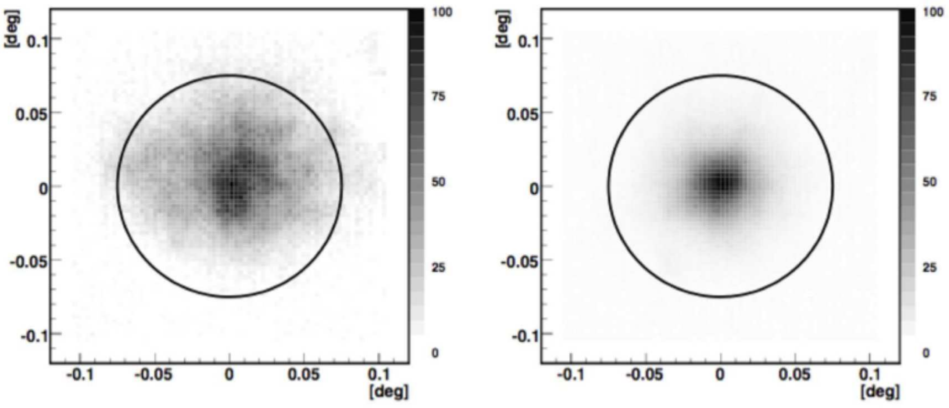

(a) PSF image before

(b) PSF image after

Figure 3–9: PSF of one of the VERITAS telescopes measured at ∼70° elevation, before (a) and after (b) the mirror alignment. Figure taken from [127].

3.3.2 Bias curves

As discussed in the trigger Section (3.2.1), a threshold for passing the L1 trigger must be determined for the pixel. This is done by performing bias curve measurements.

A bias curve measurement is done by taking data, pointing to a relatively dark patch of sky, without known gamma-ray sources and at an elevation comparable to the elevation of gamma-ray observations, and by studying the trigger rates as a function of the CFD threshold. A typical bias curve is shown in Figure 3–10. In order to determine the appropriate CFD threshold for gamma-ray observations, it is important to identify the threshold where the night sky background fluctuations no longer dominate the trigger rates. This is in the region where the trigger rate curves flatten (around 35 mV for the L3 rate in Figure 3–10). To make sure that the running conditions remain stable (*i.e.* even if the sky field is brighter), the CFD threshold value is chosen to be above the inflexion points of the L2 trigger rates (around 50 mV in Figure 3–10). The standard CFD threshold chosen for most VERITAS observations is 50 mV.

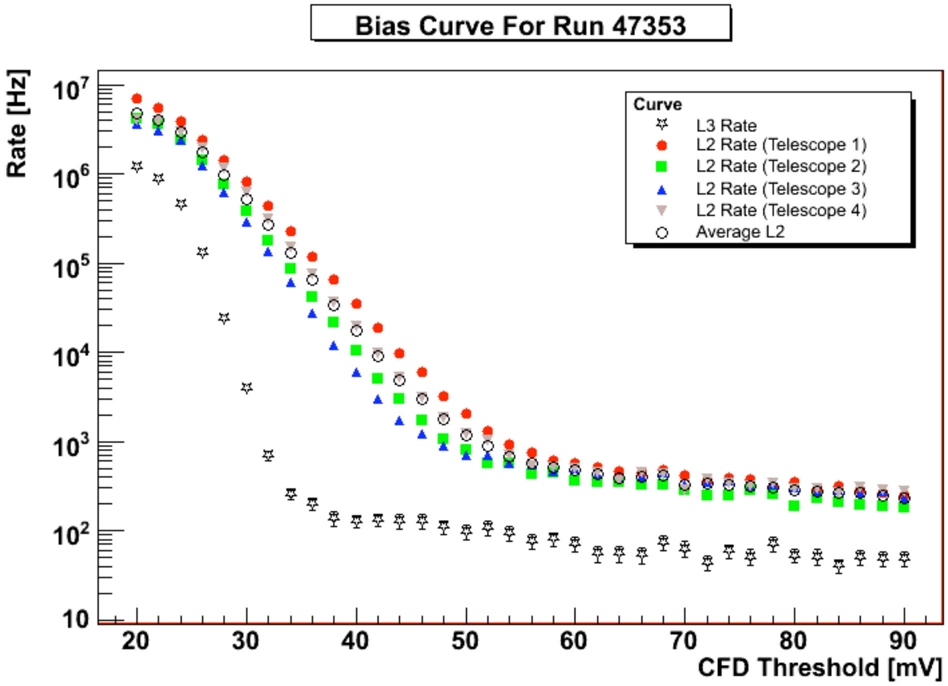

Figure 3–10: Example of a bias curve. The L2 rates for each telescope are shown as well as the L3 trigger for the array. Up to ∼35 mV for the L3 trigger and ∼50 mV for the L2 triggers, the night sky background (NSB) dominates the rates. After the inflection point of the curves, the rate curves flatten and are dominated by the Cherenkov signal.

3.4 Monte Carlo simulations

At several points in this thesis, references are made to Monte Carlo simulations. These Monte Carlo simulations involve a complex chain of simulations. A brief overview is given here.

The gamma-ray-induced and proton-induced air showers are simulated using the air shower simulation package CORSIKA [74]. From these simulations, the Cherenkov photons produced in the air showers are stored on disk. The response of the VERITAS array is also simulated, by using the Cherenkov photons which hit the mirrors. The photons are ray-traced from the mirror to the camera, using the measured quantities mirror and light cone reflectivity. For the camera, the quantum efficiency and the PMT response functions are put into to the simulation code. The simulated PMT outputs are then read by a trigger simulation which determines which events trigger the array. The last step in these simulations is the production of the FADC traces, at which point the simulated data can be analyzed in the same way as the real data.

CHAPTER 4
VERITAS analysis

The principles and techniques of gamma-ray detection by VERITAS have been described in Chapter 2. In this chapter, a detailed description of the VERITAS data analysis chain will be presented. Every step of the analysis will be described, as well as the results on the gamma-ray standard candle: the Crab Nebula.

4.1 Data calibration

The primary data recorded by VERITAS are FADC traces, time stamps of the events and L2 trigger information. As described in Chapter 3, once the trigger requirements are passed, the the events are recorded by storing the charge measured in the PMTs of all telescopes, digitized by the FADCs. A typical FADC trace is shown in Figure 4–1.

These traces are related to the amplitude of the Cherenkov pulse in digital counts (d.c.). Note that in reality, the response from the PMTs is complex, depending on wavelength, gain, etc. It is also possible to associate the value in d.c. to a number of photoelectrons (pe). Since every PMT is different, a set of calibration values are required to analyze the traces. Indeed, the gains of the PMTs are slightly different from each other and the length of their cables varies as well, changing the time of arrival of

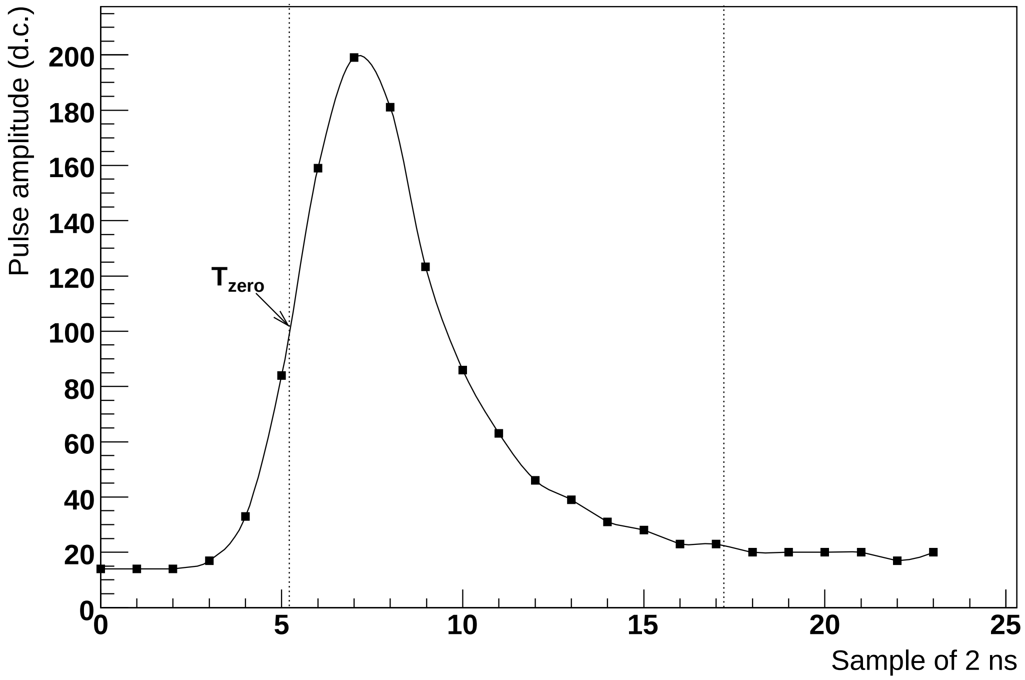

Figure 4–1: A typical FADC trace. The inclusive integration window (of 12 samples) is shown by the two vertical lines. The solid line is meant to guide the eye. Note that the pulse amplitude has been multiplied by -1, since the pulses are in negative voltages. The T_{zero} is also indicated.

the pulses and their attenuation. To calibrate, laser pulses are fired at the cameras, hitting all the PMTs at approximately the same time and with similar intensity. The laser used is a 337 nm nitrogen laser. Optical fibres are used to carry the light to each telescope; diffusers placed at the end of the fibers ensure that the intensity of light is approximately uniform over the camera (the intensity over the camera varies on the order of 10-15%). Usually a 5 minute laser calibration run, with the laser pulsed at 10 Hz, is taken each night to accommodate for any changes in the PMTs over time.

4.1.1 Pedestals

During data taking, the individual PMT rates are largely due to night sky background (NSB). Since every pointing in the sky potentially has a different NSB, we monitor this noise, by periodically recording the fluctuations in all PMTs. The outputs from the PMTs are in negative voltages. They are AC coupled and we adjust the baseline to be slightly negative to allow small positive fluctuations to be recorded while keeping an adequate range for large negative pulses. The value of the output signal of the PMTs, when no Cherenkov light is detected, is called the *pedestal*. The pedestal baseline is set to approximately 16 digital counts. To quantify the NSB, the pedestal and its standard deviation (*pedvar*) are calculated every 3 minutes during data taking. To allow the pedestal events to be read, a 1 Hz artificial trigger is sent to all telescopes, because pedestal events by design do not meet the requirements of the trigger system (see Section 3.2.1). The pedvar is correlated to both the NSB and the variability of the NSB. For a PMT response to be considered as a potential Cherenkov signal, it has to trigger a signal much bigger than the pedestal plus its pedvar. A pedestal FADC trace is shown in Figure 4–2.

The pedestal and pedvar values are averaged over 3 min intervals and are calculated for different FADC integration window sizes. The final values stored are the averages of all window sizes over all independent time windows of 3 min. These values are used to calculate the total charge in a pixel. This is done for each pixel in each camera.

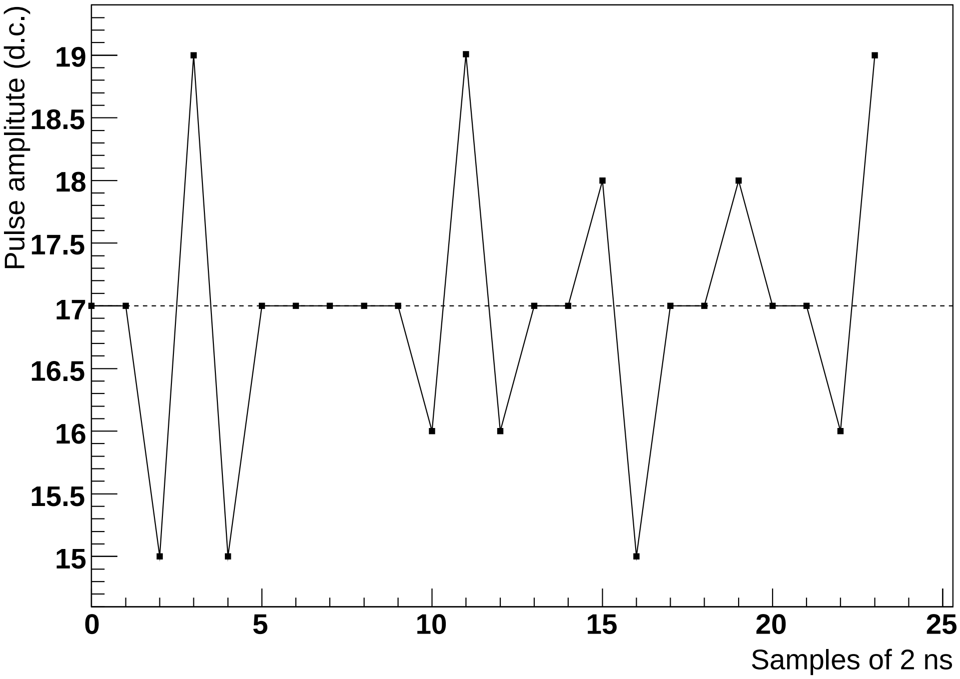

Figure 4–2: A typical pedestal FADC trace. The pedestal value is indicated by the dashed line. The solid line is meant to guide the eye.

4.1.2 $\mathbf{T}_{offset}$

As mentioned before, because the cables from the PMTs to the data acquisition system have different lengths and PMT rise time may be different, the recorded laser pulses do not all arrive at the same time in the FADC, and a time calibration must be performed, as follows. The timing calibration for each pixel is done by calculating the time of arrival (T_{zero}) of each laser pulse. The T_{zero} is defined as the time when the rising edge of the trace reaches 50% of its total height (see Figure 4–1). The position of T_{zero} is recorded for each laser pulse and for each event. An average T_{zero} over all events is then calculated for each pixel; thus the time offsets between pixels are known. An example of a T_{zero} distribution for one pixel is shown in Figure

4–3. The mean of the distribution is used as the time offset for the pixel. The offsets will be applied to that pixel for each data trace in order to be able to compare pixels.

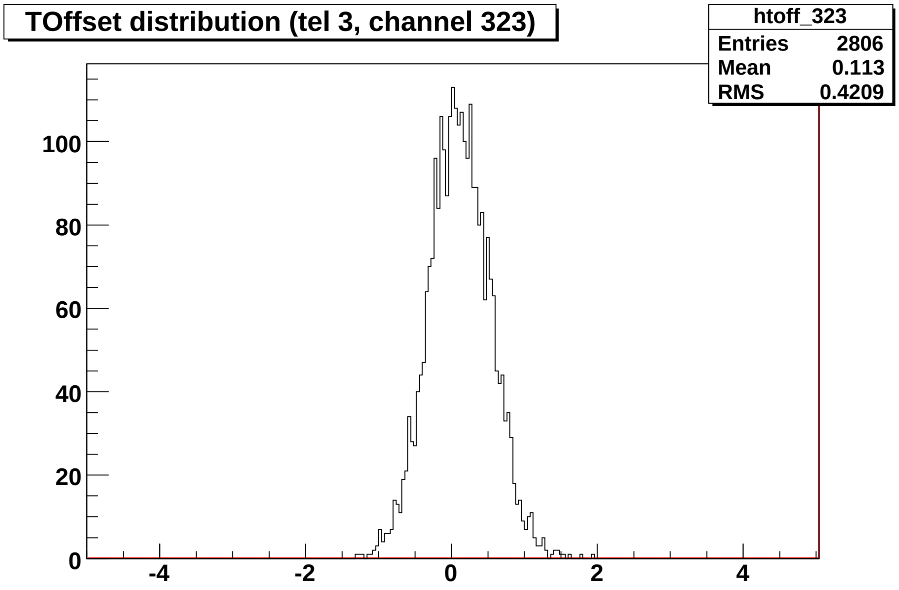

Figure 4–3: Example of a T_{zero} distribution for a single pixel over one laser run. The horizontal scale is in FADC samples (of 2 ns).

4.1.3 Gains

The relative gain calibration is also done using laser pulses. This calibration step calculates the relative gain between pixels. The intensity of the laser pulses received by the PMTs is assumed to be the same in all pixels because of the diffusers; therefore, the charge collected by the pixels measures the relative gains. An example of a relative gain distribution for one pixel is shown in Figure 4–4. These values are used to adjust the intensity of the data traces. The relative gains are adjusted (flatfielding) so that the pixels have approximately the same relative gain (within 10-20%) in order to keep the trigger rates similar in all pixels. The flatfielding of the cameras is done using a laser run. The voltage of each PMT is then adjusted to have the relative gain around 1.

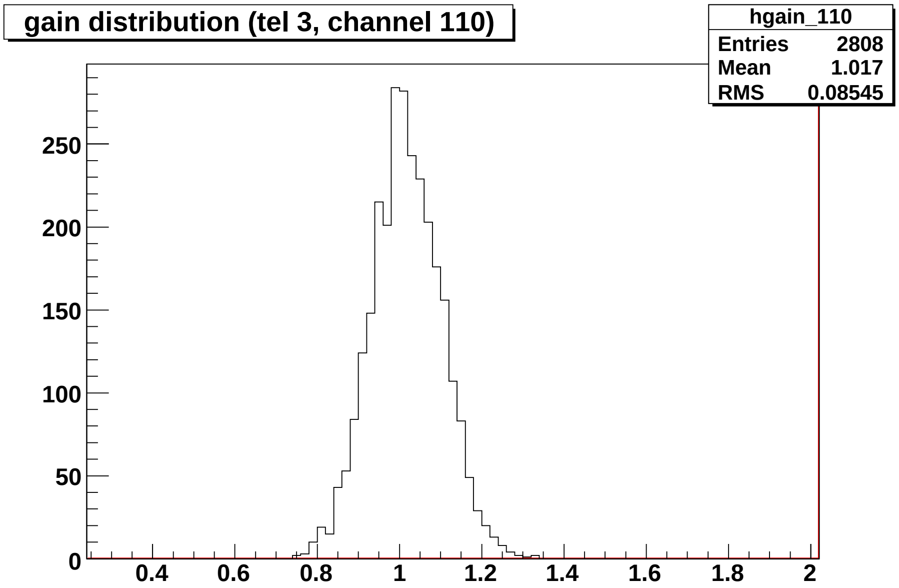

Figure 4–4: Example of a gain distribution for a pixel. Note that the mean of the distribution is around 1 because the cameras are flatfielded in order to have all the relative gains at the same value.

4.2 Shower reconstruction

4.2.1 Integrated charge

In order to obtain the total charge in each pixel, an integration of the FADC trace is done over a selected time window. An example of the integration window is shown in Figure 4–1. The integration window is defined using a double-pass method. A first pass is needed in order to find the start of the pulse, T_{zero}, defined above. After this, the time gradient across the major axis of the image in the camera is fitted to a linear function. Time gradient is present in all events due to the emission of Cherenkov photons along the shower development and to the distance from the shower core. The start of the pulse for each pixel is then extracted from the fit, which is effectively finding the relative T_{zero} for a pixel compared to the linear interpolation of the other image pixels. Finally, a second pass through the data integrates the FADC trace over a predetermined window starting at the fit-predicted pulse start. In all the analysis presented in this thesis, the window size is 12 samples of 2 ns. This size ensures that the pulses are fully contained in the integration window.

Once the charge in digital counts is calculated, the pedestal value for the same integration window size is subtracted, and the relative gains are used to calibrate the charge. This results in a calibrated integrated charge, in d.c. or in photoelectrons, for all triggered pixels for each recorded event. Dead or bad pixels are also identified in this step. Pixels for which the relative gain is too far from the mean gain of the camera are excluded from the analysis for the entire run.

4.2.2 Quality cuts

Quality cuts are applied to the data in order to have events where the reconstruction is robust. To identify which pixels contribute to an air shower image, some pixel "cleaning" is required. Pixels containing a signal consistent with the pedestal value ("noise pixels") are discarded from the image analysis. One way to do so is to apply a set of *quality cuts*. Quality cuts are cuts which are applied to the images themselves, in order to identify air showers (gamma-ray or cosmic-ray induced). These quality cuts vary according to which energy threshold is desired. The cuts described here are the *standard* cuts and they are summarized in Table 4–1 in Section

4.3. These cuts are intended for gamma-ray sources which have spectra similar to the Crab Nebula and have moderate strength (around 5% of the Crab Nebula flux). The cuts have been optimized using the Crab Nebula itself, scaled to 5% of its flux. The cuts mentioned here are applied to all events in all telescopes.

- For a pixel to be considered as containing a signal, the integrated charge must be greater than the value of the pedestal plus 5 times its pedvar ($ped + 5 \times pedvar$).
- To be considered as an image, at least 4 adjacent pixels have to reach the signal level.
- Once 4 adjacent pixels are identified as containing a signal, a looser requirement is applied to identify boundary pixels. These pixels, which must have a neighboring signal pixel, are required to have an integrated charge greater than the pedestal plus 2.5 times its pedvar ($ped + 2.5 \times pedvar$).
- It is required that less than 20% of the total image charge be contained at the edge of the camera (the edge is defined as those pixels having fewer than 6 neighboring pixels). This is to cut showers that have a large fraction of the image lying outside the camera.

For an array of telescopes, stereo reconstruction improves the performance considerably (see Section 2.2.3). Therefore, another set of quality cuts is applied to take advantage of stereo observations. These cuts add the requirement that at least two telescopes have images that have successfully passed the quality cuts. After this selection, remaining events can be analyzed.

4.2.3 Image parameterization

As explained in Section 2.2.2 in order to identify gamma-ray air showers, the recorded images are fitted with an ellipse and parameterized according to the Hillas parameters. These parameters are used in the gamma/hadron separation cuts. At this step in the analysis, all images are fitted and the Hillas parameters are extracted.

4.2.4 Source location reconstruction

It was shown in Chapter 2 that the major axis of the fitted ellipse indicates the shower direction, pointing toward the source location. It was also shown that the major axis intersection of all images in the combined camera image (superposition of all the cameras) is an estimation of the source position. When using more than two telescopes, there can be multiple intersection points. In this case, a single point is chosen by minimization of the perpendicular distances. Figure 4–5 shows a view of the major axis intersections with the perpendicular distances. The distances are weighted by the size of the image and by the ratio *width*/*length* to give bigger showers (which are imaged more accurately) more weight in the minimization. Once the intersection point, and hence the arrival direction of the event, is obtained, it is possible to create a skymap. The coordinates of the reconstructed events are in camera coordinates. To account for apparent rotation of the sky during an observation, and to combine data from different runs, the position of the events must be converted to standard astronomical coordinates (equatorial coordinates J2000): right ascension (RA) and declination (dec). This is done by first derotating the camera coordinates and then by calculating the RA and Dec. using the location of the observatory and the time of the observation. This analysis step results in a 2-dimensional histogram (skymap) of all received events in celestial coordinates. A skymap example is given further in Figure 4–14 for the Crab Nebula.

The number of reconstructed events in a 20 minute run is very low and the bin size in a skymap is small ($0.01^{\circ 2}$). This is why the skymaps are smoothed. To do so, an area, the size of the theta square value (see Table 4–1), is used around each pixel. The number of events in each pixel corresponds to the integrated number of events in that area. The final skymap, now smoothed, is called correlated skymap. During the analysis, both skymaps, correlated and uncorrelated are produced.

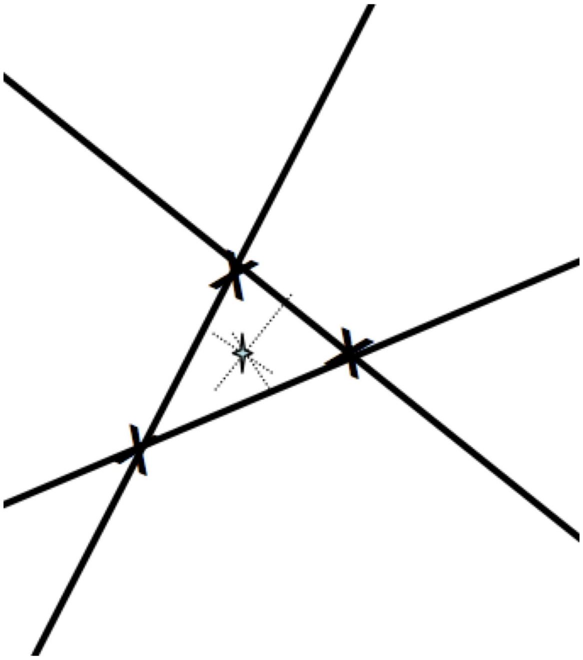

Figure 4–5: Example of how the source position (star) is found by minimizing the perpendicular distances (dotted lines) from the major axes (solid lines).

4.2.5 Core location reconstruction

While the source position is reconstructed at the intersection of the major axes in camera coordinates, the core location of the shower (where it hits the ground) can be reconstructed in spatial coordinates. This is done by using the major axis of each image, working in spatial coordinates (see Figure 2–9). The axes are projected in a plane perpendicular to the telescope pointing direction. Since the source position has already been identified (see above), axes passing through the centroid of each ellipse and the reconstructed source location are used instead of the fitted major axes; this increases the robustness of the fit on the core location. Figure 4–6 shows the intersection of the axes in the plane described above, and the reconstruction the shower core location.

4.2.6 Mean scaled parameters

As described before, the Hillas parameters are used to differentiate cosmic-ray images from gamma-ray images. In particular, the *length* and *width* parameters are useful to identify if the image is shaped like an elongated ellipse or if it is less regular. However, depending on the distance between the shower impact on the ground and the telescopes, the image will look more or less bright in the telescopes. The closer the shower is to a telescope, the brighter will be the image. Therefore, it is crucial to correlate the parameters of the ellipse with the impact parameter of the shower on the ground. To do so, Monte Carlo simulations are used. A large number of gamma rays are simulated at several zenith angles. These simulated gamma rays are reconstructed and then parameterized by *length*, *width*, *size* and impact parameter.

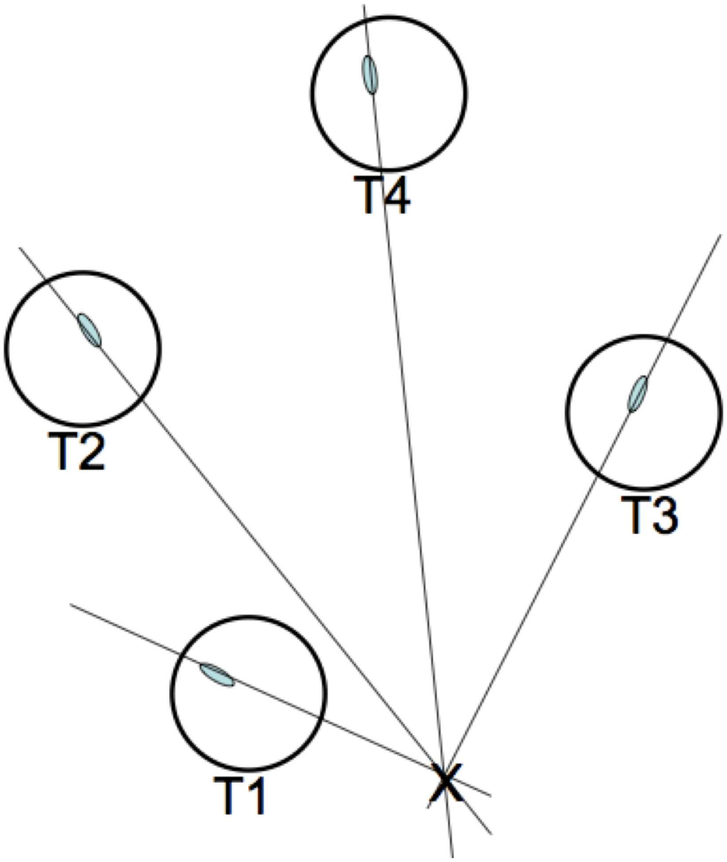

Figure 4–6: Example of how the core location is determined in the plane perpendicular to the telescope pointing direction (in spatial coordinates).

The values are stored in lookup tables that will be used later to reconstruct the shower parameters. Figure 4–7 shows an example of lookup tables for the *width* and *length* parameters where the median value of these parameters is plotted as a function of reconstruction shower impact parameter and image size.

From these lookup tables, scaled parameters (SW: scaled *width* and SL: scaled *length*) can be calculated. A scaled parameter means that the reconstructed image parameter is divided by the mean of the simulated image parameter:

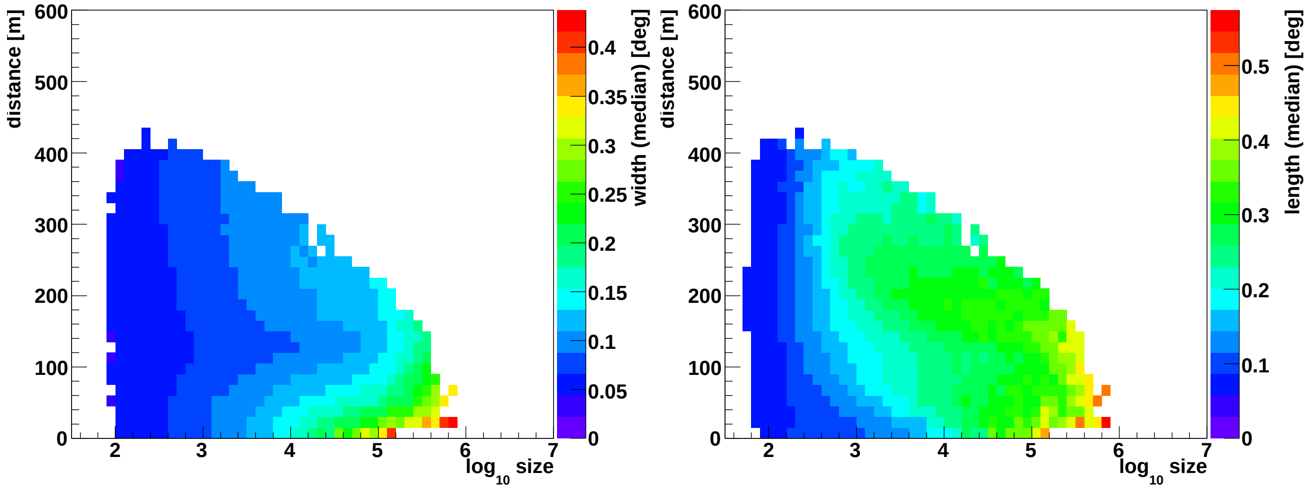

Figure 4–7: Lookup tables for the median of the *width* parameter (left) and for the *length* parameter (right) produced from Monte Carlo simulations as a function of shower impact parameter and image size (in d.c.).

$$SW = \frac{w(S,D)}{\langle \hat{w}(S,D) \rangle} \tag{4.1}$$

$$SL = \frac{l(S,D)}{\langle \hat{l}(S,D) \rangle} \tag{4.2}$$

where S is the image *size*, D is the impact parameter, w(S,D) (l(S,D)) is the *width* (*length*) of the image and $\hat{w}(S,D)$ ($\hat{l}(S,D)$) is the mean or median of the image *width* (*length*) of the simulated images. With multiple telescope data, these parameters (SW and SL) can be averaged over all telescopes that have an image:

$$MSCW = \frac{1}{n}\left(\sum_{i}^{n}\frac{width_i - \hat{w}(S,D)}{\sigma_{width,MC}(S,D}\right) \tag{4.3}$$

$$MSCL = \frac{1}{n}\left(\sum_{i}^{n}\frac{length_i - \hat{l}(S,D)}{\sigma_{length,MC}(S,D)}\right) \tag{4.4}$$

where $MSCW$ is the reduced Mean Scaled Width and $MSCL$ is the reduced Mean Scaled Length, n is the number of telescopes and $\sigma_{width,MC}(S,D)$ and $\sigma_{length,MC}(S,D)$ are the errors on the values from the Monte Carlo simulations. It is these mean scaled parameters that will be used in the cuts to reject cosmic-ray showers (see Section 4.3).

4.2.7 Energy reconstruction

A last parameter that can be extracted from the shower image is the shower energy. This quantity is linked to the image *size* and the impact parameter. Again, close showers will appear bigger (more energetic) than far showers, which will look smaller (less energetic). In this case again, Monte Carlo simulations are needed. The Monte Carlo simulations are done for several zenith angles and noise levels. An example of a lookup table for energy reconstruction is shown in Figure 4–8.

4.3 Separation between gamma-ray images and cosmic-ray images

Once the images have been fitted and parameterized, the location of the shower core and the source can be identified, and the energy of the shower can be measured. The next analysis step is to reject cosmic-ray images. First of all, it is important to

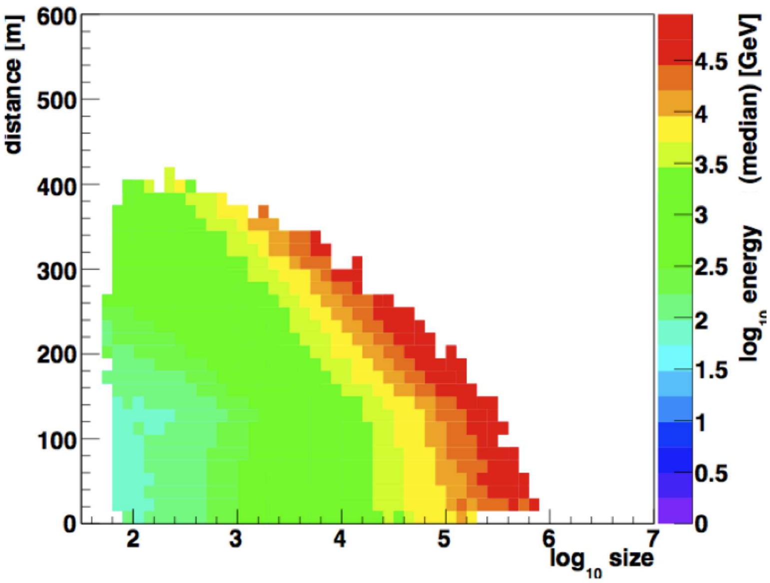

Figure 4–8: Lookup table for the energy of a shower as a function of the image *size* (in d.c.) and the impact parameter, produced from Monte Carlo simulations.

discard showers that have landed too far from the telescopes (> 250 m) because those images have major axes that are almost parallel, generating a large uncertainty on the reconstructed core location. In addition, images that fall far from the center of the camera (> 2.0°) must be rejected to avoid loss of the image outside the camera.

As explained in Section 2.2.2, the distributions of the Hillas parameters, such as *width* and *length* are very different for gamma-ray images and cosmic-ray images[1] . Another parameter often used in the analysis is theta squared (θ^2). This parameter represents the angular distance between the arrival direction of a shower and the

---

[1] Note that in the analysis the MSCW and MSCL are used instead of the *width* and *length* (Section 4.2.6).

putative source location. The further away the arrival location is from the source position, the greater the chance that the shower was not produced by a gamma ray emitted by the source. Since cosmic rays arrive isotropically from the sky, this parameter is useful to reject events that are not related to the source, like cosmic rays.

At this step, a set of cuts on MSCW, MSCL and θ^2 is applied to the data. Table 4–1 summarizes the cuts used in the *standard* analysis where N_{tel} is the number of telescopes having images that pass the quality cuts. The core distance is the distance between the telescope and the shower core on the ground and the fiducial cut is how far from the camera center an image centroid is allowed.

Table 4–1: Quality cuts applied in the *standard* analysis. See text for details.

Cut quantity	Value
Loss	$< 20\%$
Size	> 500 d.c.
N_{tel}	> 2
θ^2	$< 0.1^{\circ 2}$
MSCW	$-1.2^\circ <$ MSCW $< 0.5^\circ$
MSCL	$-1.2^\circ <$ MSCL $< 0.5^\circ$
Core distance	< 250 m
Fiducial cut	$< 2^\circ$

4.4 Signal extraction

To this point, the selection criteria have been designed to reject images that are different than the elliptically-shaped gamma-ray images. However, sub-cosmic-ray showers, produced by π^0s, will produce small gamma-ray showers and some low energy cosmic-ray showers can look like small ellipses; that is, they appear gamma-ray like. This background is irreducible with the methods applied here. Therefore, in order to extract a potential gamma-ray signal, an accurate background estimation has to be performed, as described in the next section. Once the background has been estimated, the significance of a gamma-ray signal can be calculated.

The significance calculation is done following the Li & Ma equations [116]. These equations require the number of counts in the test region (N_{on}) and the number of background counts (N_{off}). From these two, the gamma-ray excess (N_{excess}) can be calculated by $N_{excess} = N_{on} - \alpha N_{off}$, where α is a normalization factor representing the ratio in acceptance between the test region and the background region for the given exposure time, zenith angle and position in the camera (see Section 4.5.1). Equation 4.5 gives the expression for α:

$$\alpha = \frac{\int_{on} \epsilon^{\gamma}_{on}(\theta_x, \theta_y, \phi, t) d\theta_x d\theta_y d\phi_z(t)}{\int_{off} \epsilon^{\gamma}_{off}(\theta_x, \theta_y, \phi, t) d\theta_x d\theta_y d\phi_z(t)} \tag{4.5}$$

where ϵ^{γ}_{on} is the camera acceptance of gamma-ray like events for the test region and ϵ^{γ}_{off} is the camera acceptance of gamma-ray like events for the background region, θ_x and θ_y are the x and y camera coordinates, ϕ_z is the zenith angle of the observation and t is the exposure time of the test or background region (if different).

The statistical significance (S) of a gamma-ray excess can be calculated according to Li and Ma equation 17 [116] as follows:

$$S = \sqrt{2}\left(N_{on}ln\left(\frac{(1+\alpha)N_{on}}{\alpha(N_{on}+N_{off})}\right) + N_{off}ln\left(\frac{(1+\alpha)N_{off}}{\alpha(N_{on}+N_{off})}\right)\right)^{1/2} \tag{4.6}$$

.

N_{on} is easily calculated, since it is simply the number of counts in a defined region. However, N_{off} must be estimated in a way that the significance will be minimally affected by any statistical fluctuations in the field of view. To do so, several methods have been developed. Section 4.5 presents the details of two of these methods.

It is conventional to require an excess of 5 σ for a new source to be considered a “discovery”. In the case where a source is not detected, an upper limit on the gamma-ray flux can be calculated, as discussed below in Section 4.5.4.

4.5 Background estimation

In the past, in order to get an estimation of the background, On source and Off source data were taken. The Off source observations were taken at similar zenith angle and noise level of the NSB as the On data but at a different position in the sky, and the data sets would be compared: an excess in the On source would be taken to be a gamma-ray signal. A more efficient method has been used with the bigger FOVs of the new generation of Cherenkov telescopes: *wobble* observations. In this mode, observations are taken with the telescopes pointed a certain distance away (usually 0.5°) from the source position in the four cardinal directions: North, East, South and West. The background is then extracted from regions in the FOV but away from the source. The enormous advantage of this technique is that there is no need for Off observations. All the data can be used for both On and Off regions. In addition, this observation mode ensures that the background will have similar characteristics (zenith angle, NSB noise level, etc) to the signal data.

In this section the details of two different background models used with the wobble observation mode are given. Before going into these details, the gamma-ray like event acceptance in the camera must be introduced since most background models use the acceptance of the camera in their background evaluation.

4.5.1 Acceptance in the camera

The principle of the camera acceptance correction to gamma-ray-like events is straight forward. Showers having directions near the pointing direction have a large probability of being reconstructed properly because more of the Cherenkov image is collected by the camera. In the case where the shower origin is far from the pointing, the camera will record only part of the shower for many events. Therefore the further away from the camera center an event is reconstructed, the lower the probability that it will meet the selection criteria. To determine the camera acceptance, all events passing the gamma-ray selection cuts (except the θ^2 cut) are plotted in angular-distance-squared bins. Figure 4–9 shows the acceptance curve for the *standard* cuts averaged over all zenith angles, azimuths and energies. The data used to produce an acceptance curve is usually a large set of data (containing no gamma-ray sources) that has been taken at zenith angles similar to normal gamma-ray observations (*i.e* between 20° and 35°).

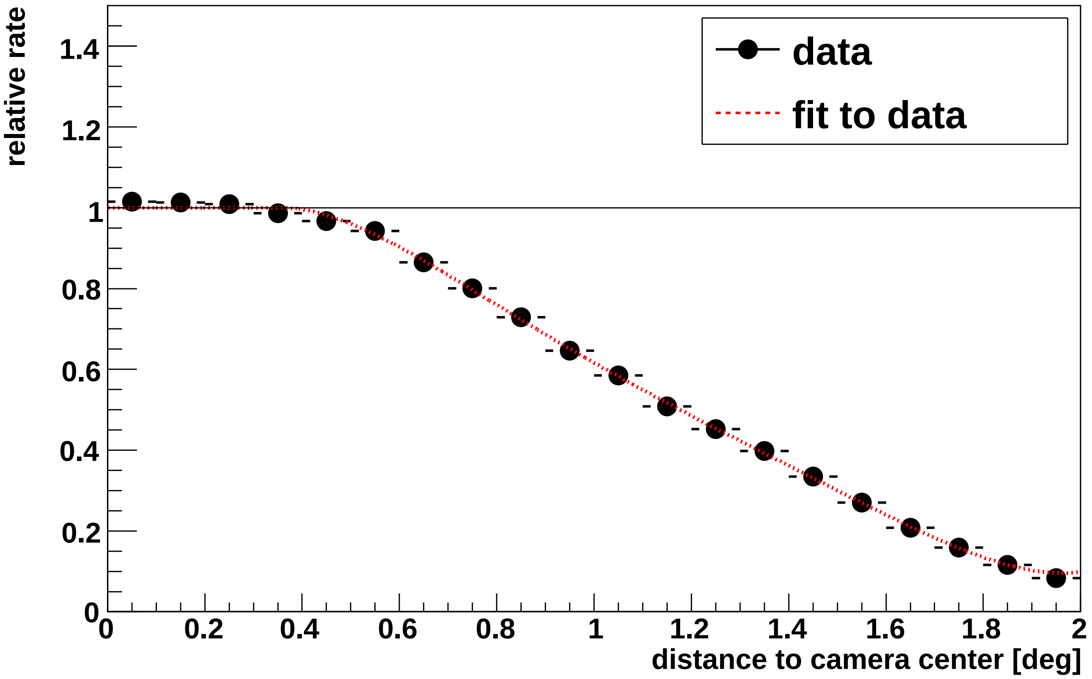

Figure 4–9: Acceptance of gamma-ray-like events in the camera in arbitrary units as a function of the distance in degrees squared from the camera center. The solid black line represents the level of full acceptance and the dotted red line shows the fit to the data.

Although the main effect on the camera acceptance is the position in the field of view, several other parameters play a role: zenith angle, azimuth and energy of the primary gamma-ray. The zenith angle affects the acceptance by favoring reconstruction of events coming from larger zenith angles, because the collection area is larger for showers coming from larger zenith angles. The azimuth affects the acceptance mainly because of the Earth's magnetic field, which goes from south to north with an inclination angle of 58° downward (at the VERITAS location). Electrons and positrons from showers are scattered more or less depending on the direction they are moving. Showers coming from the south, almost parallel to the magnetic field lines, will be less affected (scattered) by the magnetic field than showers coming from the north, which are perpendicular to the field lines. Therefore, showers coming from the south will be more accurately reconstructed by the camera. Finally, the energy of the shower also affects the acceptance. High energy showers, producing brighter images, have a smaller probability to be reconstructed if they are far from the center of the field of view. These large showers will be truncated by the camera's limited field of view resulting in them failing to pass the loss cut described above. Studies have been performed to understand the different effects mentioned above and the results are presented in Appendix 1.

4.5.2 The ring background model

In this model, the background is estimated for each bin of the skymap by using an annulus (ring) region around the bin. The ring size and width are predetermined. Usually these parameters can be optimized in order to give the best signal-to-noise ratio, and adjusted for point sources or extended sources. The analyses presented here use a ring radius of 0.5° and a ring width of 0.07°. Figure 4–10 illustrates a ring used to estimate the background around two points in the camera.

Since the ring crosses different regions of the camera, the background values for each point must be weighted by the acceptance curve (see Section 4.5.1). It is important that any gamma-ray source in the field of view be excluded from the background estimation region to avoid contamination. In addition, bright stars (magnitude < 6) are excluded from the background estimation. In the presence of bright stars, either the pixels are turned off (when the current in the pixel is too high) or the background

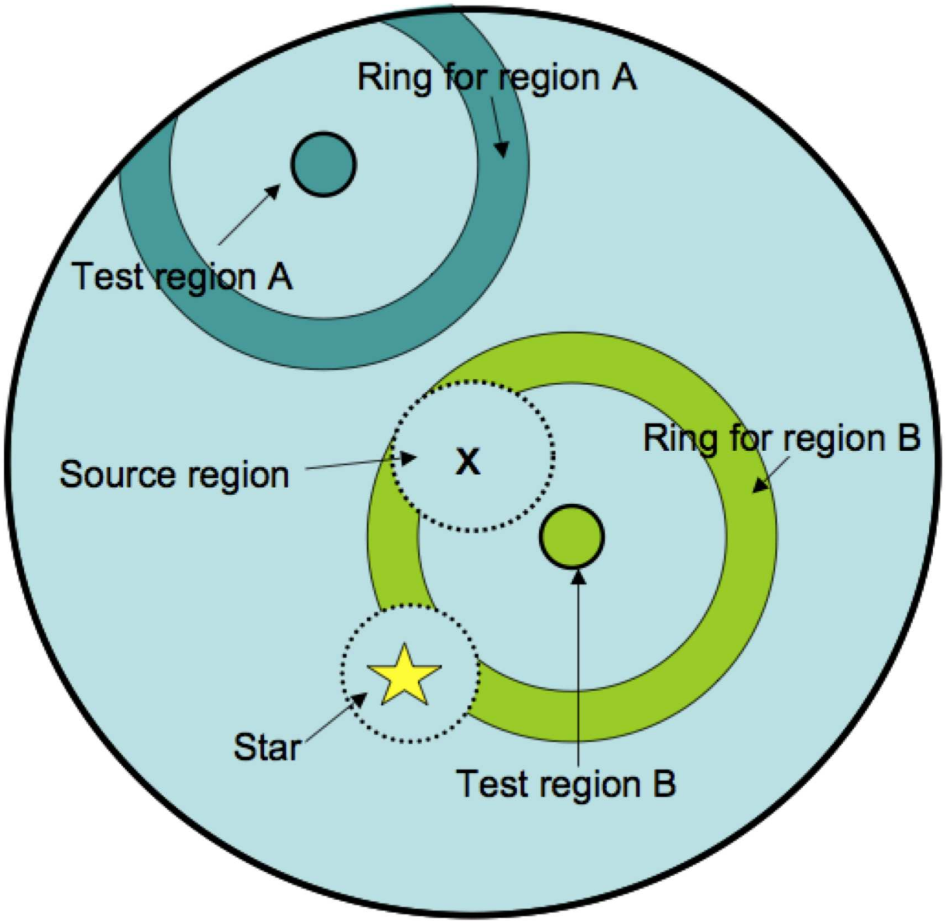

Figure 4–10: Example of rings used to estimate the background for two test regions A and B. The gamma-ray source at the center of the field of view, as well as the star region, are excluded from the background estimation.

photons received by the pixel are more numerous; therefore, the count rate of these pixels will be systematically different than the rest of the camera, and they should not be used in the background estimation.

4.5.3 The reflected region background model

In this model, the background is estimated using several background regions at the same angular distance from, and of the same size, as the test region. Figure 4–11 illustrates an example of the regions used to estimate the background of a test region.

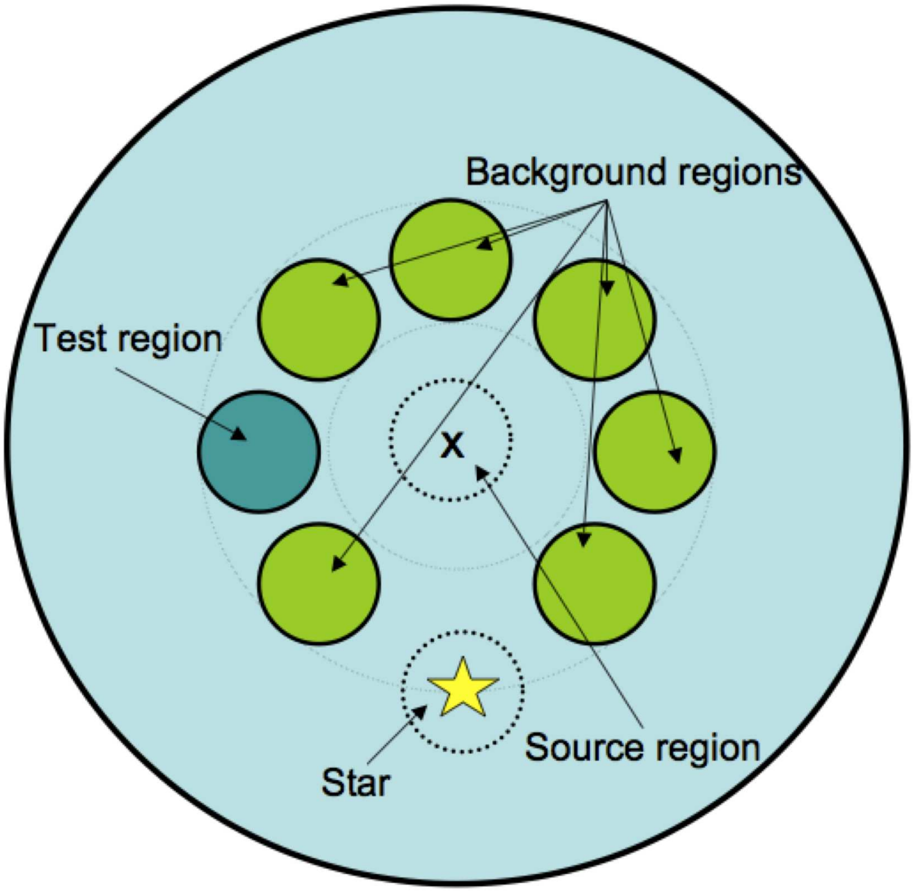

Figure 4–11: Example of reflected regions (in yellow) used to estimate the background for the test region (in green). The star region is excluded from the background estimation.

An advantage of this background model is that, since the background estimation regions are at the same angular distance from the camera center as the test region, there is no need to correct for the camera acceptance. Therefore, there are fewer sources of systematic uncertainties in the background estimates. The size and the number of background regions can be optimized to get the best signal-to-noise ratio. In this case again, known gamma-ray sources and bright stars must be excluded from th background estimation. The analyses presented here use regions with radius of 0.1°. The number of regions is set between 10 and 20. The number is determined as the maximum number of regions that can be fitted around the source depending on the source exclusion radius and the number and size of exclusion regions (like bright stars).

4.5.4 Energy flux and spectrum

When a gamma-ray source has been detected, a measurment of its energy spectrum may be possible. The energy spectrum provides information on the physical processes taking place in the source. The energy spectrum is presented as the flux of gamma rays (ϕ_γ) as a function of the energy E. We measure the number of events (N_γ) observed in an energy bin per unit of time, per unit of area: $\phi_\gamma(E) = \frac{dN_\gamma}{dtdAdE}$.

The energy determination is performed as explained in Section 4.2.7. To calculate a flux, the number of gamma rays observed for each energy bin must be divided by the live time (time of data recording, after correction for dead-time) and the effective collection area. The collection area of the detector is not a constant. Indeed, it varies with the energy of the showers, the zenith angle, the angular distance from the pointing position of the incoming particle, and with the noise level of the night sky background during the observations. We estimate the collection area as a function of these parameters, using Monte Carlo events to generate effective area tables. Gamma rays of energies between 30 GeV and 30 TeV are generated out to a maximum impact parameter (R_0) of 750 m from the array and propagated through the atmosphere. The collection area (A) is then calculated as follows:

$$A(E) = A_0 \frac{n_E}{N_E} \tag{4.7}$$

where A_0 is the area simulated (from πR_0^2), n_E is the number of simulated events of energy E that are detected and N_E is the initial number of simulated events of energy E. Figure 4–12 shows the effective area curves for the *standard* analysis.

Once the appropriate collection area is determined, the flux can be calculated. Note that usually, the reflected region model is used to determine the spectrum since it does not depend on the acceptance curve of the camera.

4.5.5 Flux upper limit calculation

In the case where the analysis reveals no gamma-ray emission, a flux upper limit can be calculated once the significance at the object position has been calculated. This is done following the Helene method [75]. In this method, the probability density functions for the gamma-ray flux (g) and the background flux (B) are assumed to follow Gaussian distributions. The background distribution has a mean B_0 and standard deviation σ_B. The function for the gamma-ray flux is assumed Gaussian as expressed by Equation 4.8:

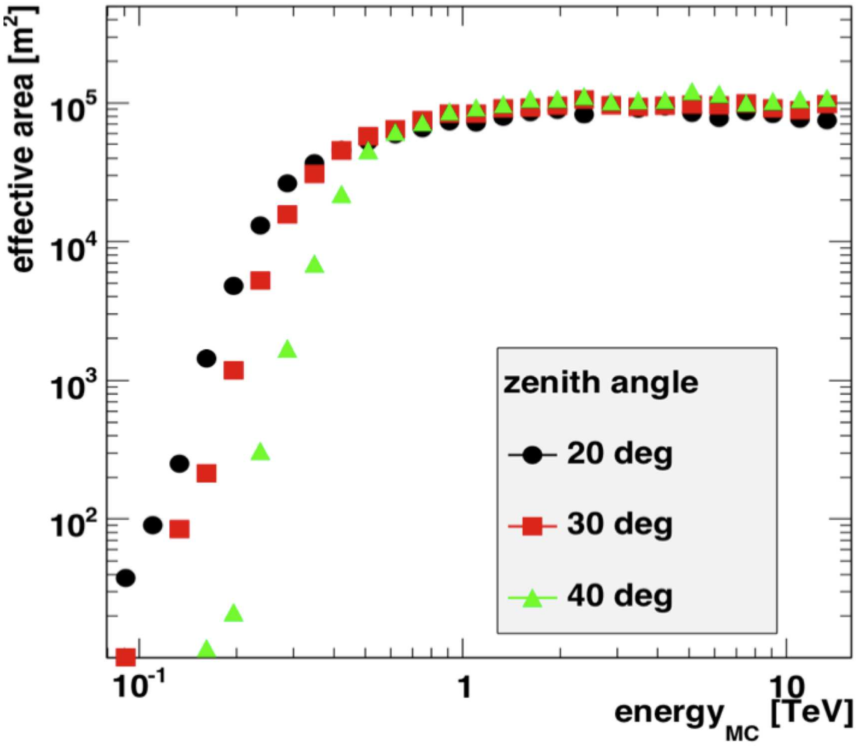

Figure 4–12: Effective areas produced from Monte Carlo simulations for *standard* cuts for three different zenith angles.

$$g(a) \cong n \frac{e^{-(a-\bar{a})^2/2\sigma^2}}{\sqrt{2\pi}\sigma} \tag{4.8}$$

where n is a normalization factor, a is the gamma-ray flux, $\bar{a} = C - B_0$ (with C being the total gamma-ray excess counts), and $\sigma^2 = \sigma_B^2 + C$. From equation 4.8, the gamma-ray flux upper limit A can be extracted as follows:

$$\alpha = \int_A^\infty g(a)da \tag{4.9}$$

where α is the probability desired for the upper limit (the confidence level of the upper limit is $(1-\alpha)$).

4.6 Crab Nebula

The details of the analysis chain have been presented above. Here, the analysis of the Crab Nebula, the VHE gamma-ray standard candle, is presented in order to give an example of the results produced by the analysis chain.

4.6.1 Crab observations

The data used here were acquired in fall 2009, with the updated VERITAS array configuration. A total of 3.84 h of observations has been analyzed. Table 4–2 summarizes the observations.

Table 4–2: Details on the Crab Nebula data.

Run number	Date yy/mm/dd	Wobble direction	Elevation (°)
46883	09/09/18	W	60
46884	09/09/18	N	64
46927	09/09/19	N	64
46960	09/09/20	S	61
46961	09/09/20	E	66
46962	09/09/20	W	71
46992	09/09/21	N	65
46993	09/09/21	S	69
46994	09/09/21	E	72
47027	09/09/22	W	67
47028	09/09/22	N	71
47029	09/09/22	S	74

4.6.2 Crab analysis

The runs presented in Table 4–2 were analyzed. The *standard* cuts (see Table 4–1) were used. There are two bright stars (magnitude 2.81 and 4.73) in the field of view of the Crab Nebula that have been excluded from the background estimation (with an exclusion radius of 0.15°).

4.6.3 Crab results

The results of the analysis using both the ring background model and the reflected region model are summarized in Table 4–3. Parameters useful for interpretation of the results are also presented in Table 4–3.

Figure 4–13 shows the MSCW and MSCL distributions for the Crab Nebula analysis. Note that the cuts shown in Table 4–1 are applied on these distributions and that the gamma-ray peak is clearly visible between the values of -1.2 and 0.5.

Table 4–3: Results of the Crab Nebula analysis.

Background model	N_{On}	N_{Off}	α	N_{Excess}	Significance (σ)	γ-ray rate (γs/min)
Ring	1049	217	0.17	1013	54.7	4.39 ± 0.14
Reflected regions	1049	445	0.08	1014	61.2	4.39 ± 0.14

Figure 4–14 shows the skymaps for the ring model (top) and reflected regions (bottom). Figure 4–15 shows the significance distributions for both background models. The signal from the Crab Nebula is clearly visible in the distributions (note that the distributions have been truncated at 10σ in order to have a good view of the

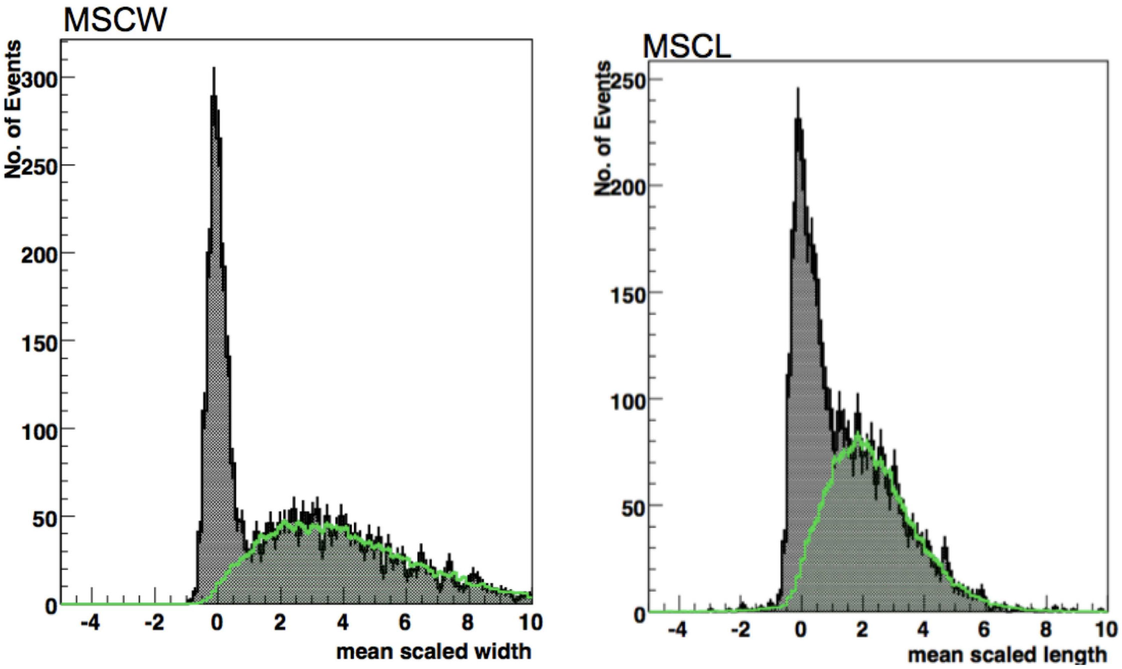

Figure 4–13: MSCW (mean scaled width) (left plot) and MSCL (mean scaled length)(right plot) distributions for the Crab Nebula analysis. The grey-filled histograms show the parameters for On events and the light green histograms show the parameters for the Off events.

Gaussian distribution of the rest of the map, where no gamma-ray signal is present).

4.6.4 Crab spectrum

Finally, the data points for the Crab spectrum produced by the reflected region analysis are shown in Figure 4–16. The spectrum is well fitted with a power law of the shape $dN/dE = I(E/TeV)^{-\Gamma}$, where I is the normalization constant and Γ is the spectral index. The power law fit parameters are presented in Table 4–4.

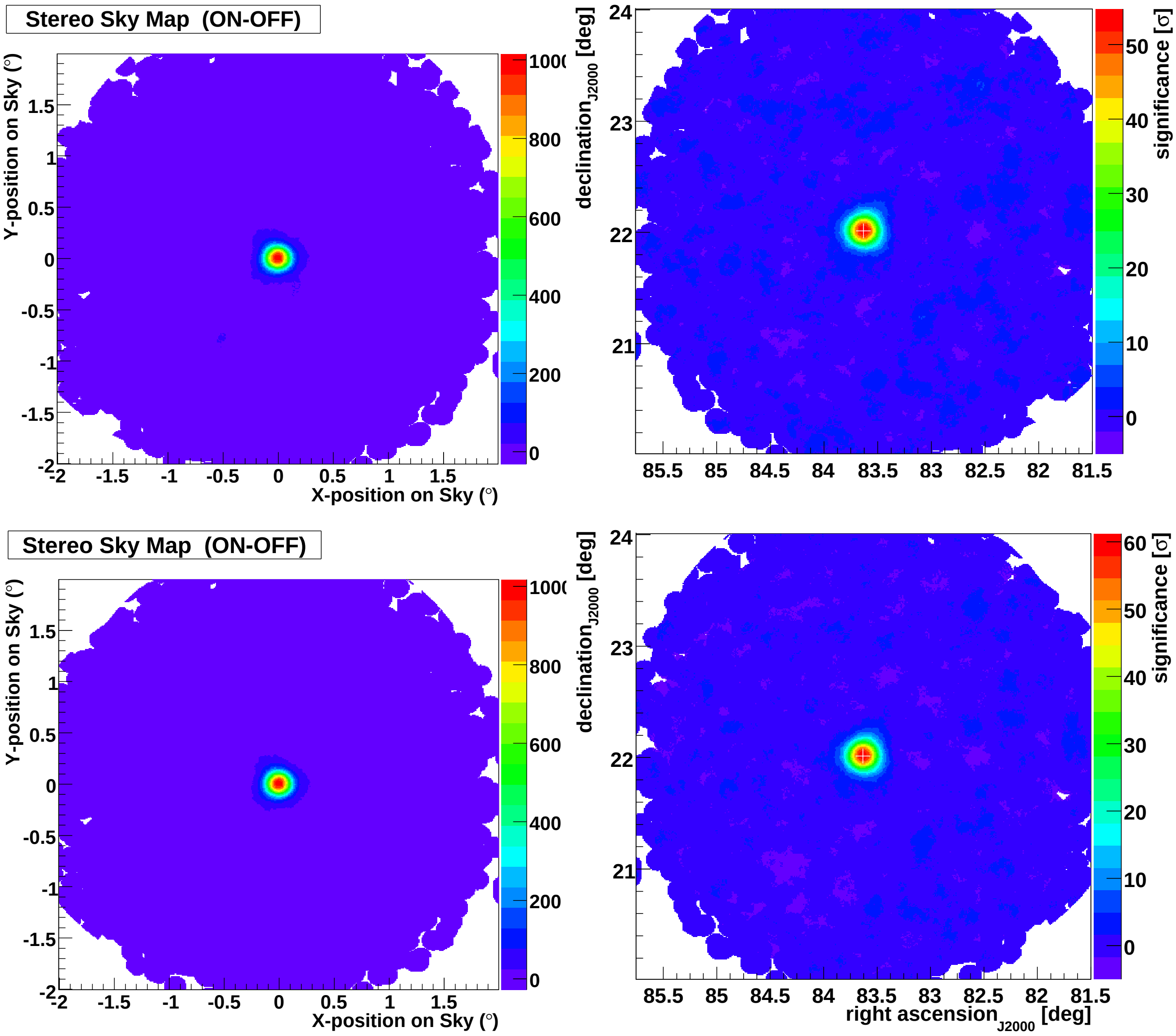

Figure 4–14: Results of the Crab Nebula analysis for the ring model (top row) and the reflected region model (bottom row). The left plots show the excess count maps in camera coordinates and the right plots show the significance skymaps in equatorial J2000 coordinates.

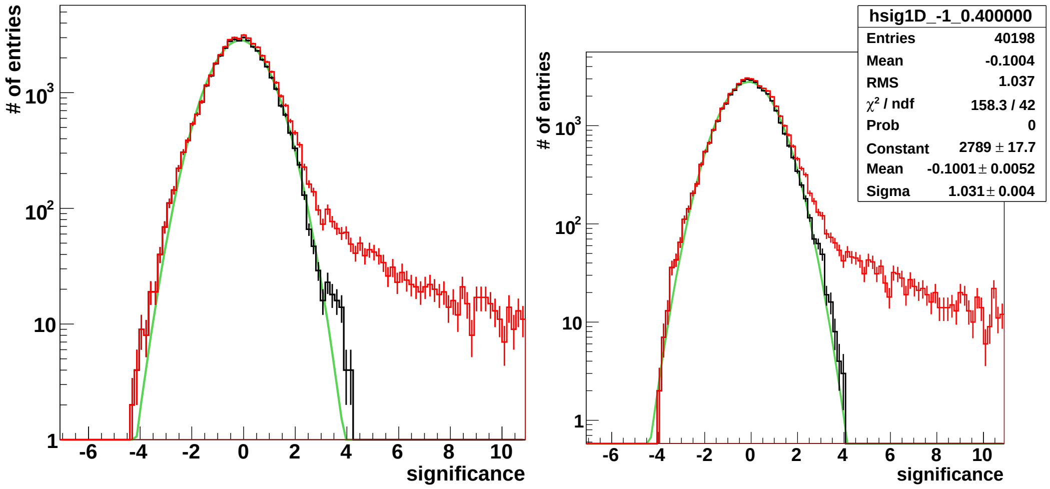

Figure 4–15: Significance distributions from the significance maps (see Figure 4–14) for the ring model (left) and the reflected region model (right). The black curves show the significances for the bins excluding the source region. They are well-fitted by Gaussian distributions of mean 0 and standard deviation of 1. The red curve shows the significances for all the bins in the skymap.

Table 4–4: Results on the Crab Nebula data.

Fit parameter	Value
Normalization constant at 1 TeV	$(3.50 \pm 0.14)\times 10^{-11}$ cm^{-2}s^{-1}TeV^{-1}
Spectral index	2.52 ± 0.05
Reduced χ^2	1.87

From the results shown in Table 4–4, obtained from the power law fit on the data points from Figure 4–16, the integrated flux can be calculated. This gives an integrated flux, at energies above 1 TeV, of $(2.30 \pm 0.10) \times 10^{-11}$ cm^{-2}s^{-1}.

4.6.5 Discussion of the Crab results

The Crab Nebula was first detected in VHE gamma rays in 1989 by the Whipple collaboration (see Section 1.1.3). Since then, this source has been extensively

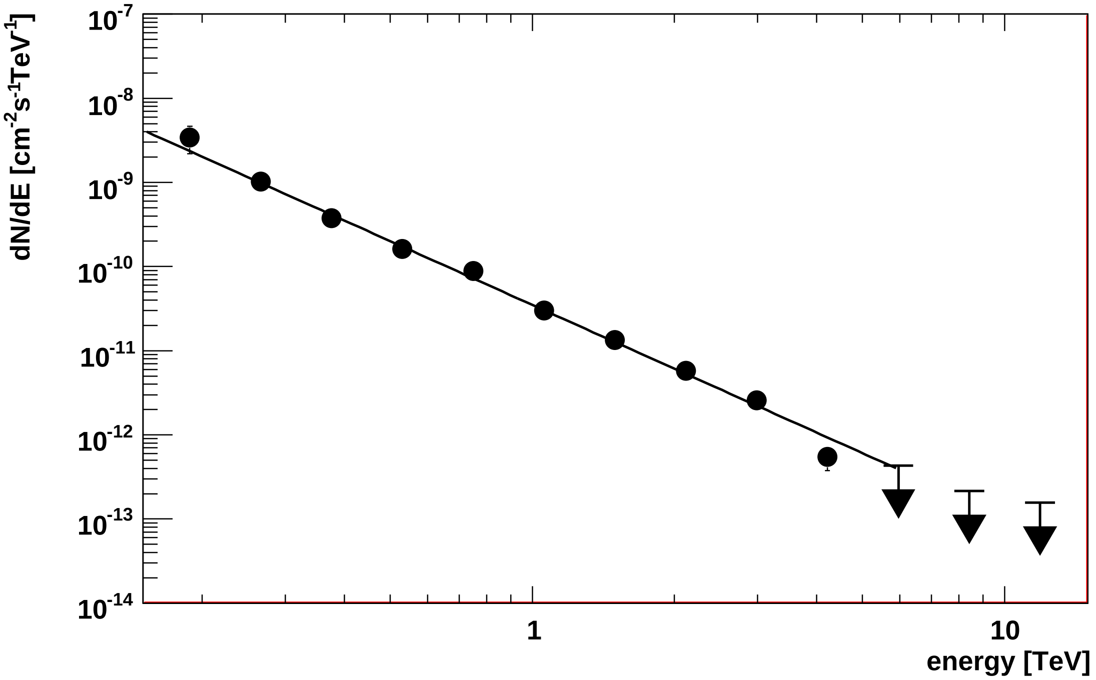

Figure 4–16: Differential Crab spectrum produced from the reflected region analysis. The results from the fit are presented in Table 4–4.

observed and it has become the VHE standard candle. All TeV experiments have published their results on the Crab in order to compare between each other, since no variability has ever been observed in the Crab Nebula flux. Table 4–5 shows the fluxes obtained for several TeV experiments.

Table 4–5: Values obtained for the power law fit to the Crab spectrum for different TeV experiments.

Experiment	Spectral Index	Integrated flux above 1 TeV ($\times 10^{-11}$ cm^{-2}s^{-1}TeV^{-1})
Whipple[67]	2.64 ± 0.03	1.94 ± 0.05
HEGRA[9]	2.62 ± 0.07	1.74 ± 0.39
H.E.S.S.[112]	2.60 ± 0.01	2.20 ± 0.02
VERITAS [29]	2.54 ± 0.05	2.35 ± 0.12
This work	2.52 ± 0.05	2.30 ± 0.10

Note that the systematic uncertainties have not been taken into account here. The agreement between the analysis presented in this thesis and the results from other TeV experiments demonstrates that the analysis chain gives results consistent with expectations.

CHAPTER 5
Magnetars

Magnetars are rotating neutron stars with extremely strong magnetic fields. In this chapter, these objects will be described in detail, as well as the reasons why observations in the VHE regime can improve the understanding of these peculiar neutron stars. To date, VERITAS has observed three magnetars. Results from these observations will be presented along with the physical interpretation of these results.

5.1 The physics of magnetars

5.1.1 The magnetar model

Magnetars are a subclass of neutron stars characterized by ultra-high magnetic fields ($10^{14} - 10^{15}$ G). They are young neutron stars, as seen in Figure 5–1, with ages of the order of $10^3 - 10^4$ years. Their young age is indicated by the fact that several magnetars are associated with young supernova remnants. They have properties distinguishing them from the bulk of regular radio pulsars, as shown in Figure 5–1. They all have persistent X-ray luminosity of the order of $10^{34} - 10^{36}$ erg/s, slow X-ray pulsations between 2 s and 12 s and large spin-down rates between $10^{-10} - 10^{-12}$ ss^{-1}. Their persistent X-ray luminosity exceeds the spin-down luminosity (see Equation

5.2), implying that the X-ray emission cannot be explained by rotational energy losses alone. As of early 2010, there are 14 confirmed magnetars and 5 candidates[1] .

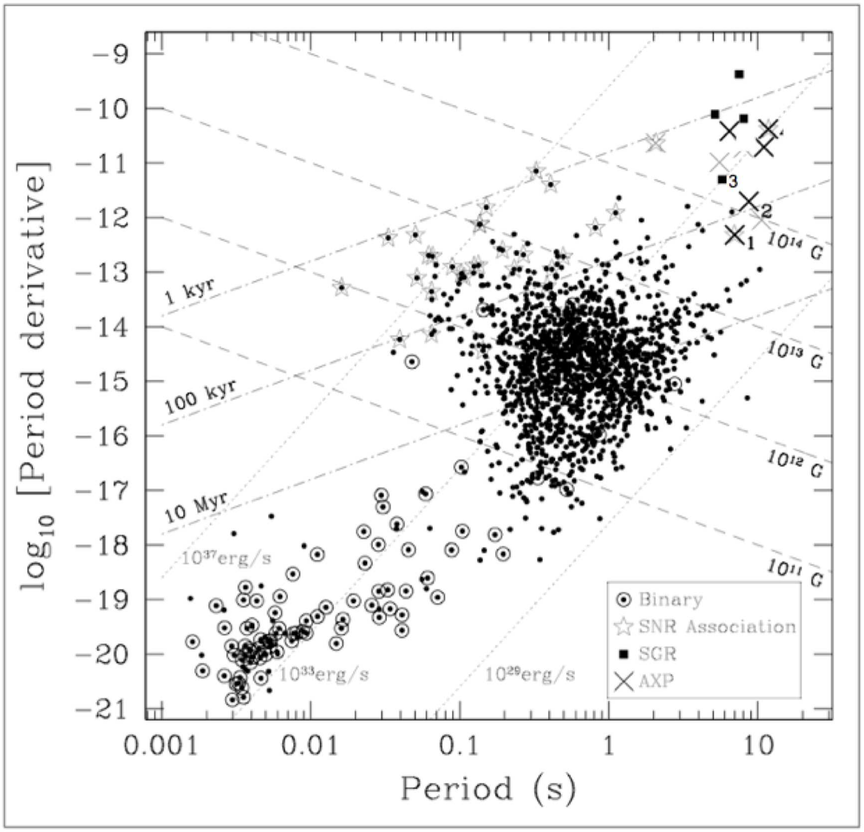

Figure 5–1: The $P - \dot{P}$ diagram for 1629 pulsars in the ATNF catalog. AXPs are indicated with crosses and SGRs with solid squares. Lines of constant magnetic field (dashed line), spin-down luminosity (dotted line) and characteristic age (dot-dashed line) are shown. The magnetars presented in this chapter are identified by the numbers 1 (1E 2259+586), 2 (4U 0142+61) and 3 (SGR 0501+4516). Figure adapted from [39].

---

[1] http://www.physics.mcgill.ca/∼pulsar/magnetar/main.html and [71].

Magnetars are subdivided into two categories: Anomalous X-ray Pulsars (AXPs) and Soft Gamma-ray Repeaters (SGRs). The distinction is mainly historical. SGRs were discovered during major outbursts and display hard X-ray and soft gamma-ray spectra. AXPs were discovered from pulsations in their soft X-ray emission.

The origin of the high magnetic field

Magnetars are neutron stars. They are created in processes similar to other neutron stars. At the end of the star's life, it collapses on itself in a supernova explosion. The remains of this phenomenon are known as a supernova remnant, with a compact object at its center. When the mass of the progenitor star is between 1.4 $M_\odot$ and $\sim$5 $M_\odot$, the compact object is a neutron star. The details of their formation are outside the scope of this thesis; however, the particularities in the formation that allow a neutron star to become the special case of a magnetar will be described below.

Magnetars have very high magnetic fields (B) as shown by Equation 5.1, which gives the magnetic field for a rotating magnetic dipole.

$$B \sim 3.2 \times 10^{19} (\dot{P} P)^{1/2} \tag{5.1}$$

where P is the rotation period and $\dot{P}$ is the period derivative. There are different theories to explain the origin of the extreme magnetic field in magnetars. One model postulates that in neutron stars born with periods on the order of 1 ms, an efficient dynamo can be supported [48]. In such a case, the increase of magnetic stresses in the outermost parts of the star reduces the differential rotation. Intense convection in these layers amplifies the magnetic field.

Another model is based on the hypothesis that massive stars are the progenitors of magnetars [134]. In fact, four magnetars (CXO J164710.2-455216, SGR 1806-20, SGR 1900+14 and 1E 1048.1-5937) are located (or suspected to be) in star clusters. For example, CXO J164710.2-455216 lies in the well-known massive star cluster Westerlund 1 [152][133] and has a progenitor star of mass $> 40M_{\odot}$. These associations between magnetars and star clusters support the fact that magnetars can be formed from massive stars.

In the case of a highly magnetized massive star, with magnetic fields of the order of $\sim$1 kG [40, 41, 42], the magnetic field would be given by the progenitor itself. By compressing this field to the size of the neutron star during the collapse, the field can reach $\geq 10^{14}$ G [56]. In the case where the massive star's magnetic field is lower, internal magnetic fields of the order of $\sim 10^{15} - 10^{16}$ G are created in the collapse of the star [21]. These magnetic fields are generated in the strong interactions in the neutron star interior. With time, the magnetic field energy of the core will be dissipated, increasing the magnetic field at the stellar surface up to the observed intensities.

X-ray emission of magnetars in quiescence

One of the main characteristics of magnetars is that their X-ray luminosity (of the order of $10^{34} - 10^{36}$ erg/s) is much higher than the spin-down luminosity. Assuming that the rotational energy of the pulsar is $E_{rot} = \frac{1}{2}I\Omega^2$ (with I being the angular momentum and Ω the angular velocity), the rotational energy loss as a function of time is $\frac{dE_{rot}}{dt}$. Equation 5.2 shows the rate of loss of rotational energy ($\dot{E}$) in the dipole spin-down model:

$$\dot{E} \sim (4\pi^2 I)\dot{P}P^{-3} \tag{5.2}$$

where P is the period, $\dot{P}$ is the period derivative and the moment of inertia $I = 10^{45}$ g cm^2. For a magnetar with P $\sim$5 s and spin-down rate $\sim 10^{-11}$ ss^{-1}, the spin-down luminosity, $\dot{E}_{rot}$ is of the order of $\sim 10^{33}$ ergs/s. This shows that the rotation alone cannot power the observed luminosity in magnetars.

It is believed that the magnetic field decay provides the necessary power for the persistent X-ray luminosity [163]. The strong magnetic field diffuses out of the core of the magnetar. The energy is conducted from the heated core to the surface and powers the intense X-ray flux. The persistent non-thermal emission may also be induced by a twisted magnetosphere [160]. The currents produced in the twisting may flow everywhere inside the magnetosphere. The energy created from these currents is dissipated outside the star and efficiently accelerates particles along the field lines, producing the non-thermal X-rays [159]. Figure 5–2 illustrates the twisted magnetosphere lines. Similar processes occur in the Sun on a smaller scale.

X-ray emission of magnetars in bursting state

The magnetar model was originally designed to explain the major outbursts responsible for their discovery. The outburst intensity is a distinctive characteristic

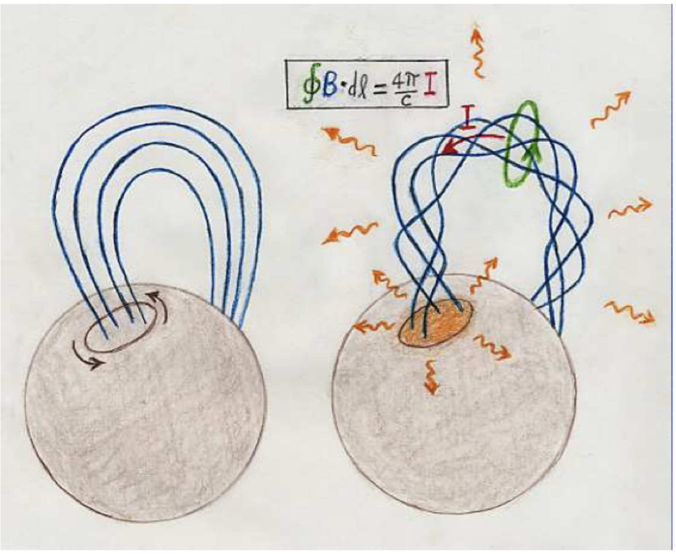

Figure 5–2: Magnetic twists give rise to X-ray emission from magnetar. Figure produced by R. Duncan [47].

proper to magnetars. Indeed, during such flares, the X-ray flux can be on the order of 10^6 to 10^9 times larger than the quiescent flux.

It is unlikely that these outbursts are powered by accretion, as is the case for compact objects in binary systems; the energy intensity and the spectrum hardness of major magnetar outbursts suggest otherwise (e.g. [126]). The hard spectrum suggests that there is no disk around the magnetar; if a disk were present, the spectrum would be softened by interaction with the surrounding particles [162].

A natural explanation that emerges from the magnetar model is that the flares are powered by the magnetic field [162]. The strong magnetic field of magnetars can cause the neutron star crust to break [161], which is not the case for regular neutron stars. The diffusion of the magnetic field in the neutron star, as explained previously, may induce sudden and large-scale instabilities. These instabilities can displace the footpoints of the external magnetic field, causing catastrophic reconnections [48]. The rare large flares observed from different SGRs can be explained by a large-scale readjustment of the stellar magnetic fields. The more frequent smaller bursts from SGRs are then described by the cracking of the magnetar crust.

5.1.2 Very high energy emission from magnetars

In the GeV and TeV regimes, magnetars have not yet been detected. Theories have been developed to model potential high-energy emission. Because there is non-thermal emission at lower energies, it is natural to think that high-energy photons could also be emitted. Four models that describe high-energy emission from magnetars are presented here.

Model for fast-spinning magnetars

This model [120] studies the emission from newly born magnetars (note that newly born magnetars have not been detected yet) that have rotational periods on the order of ms [48]. Such a short period induces an enormous spin-down luminosity, (see Equation 5.2). The spin-powered luminosity (L_{sd}) for magnetars can be described by the following equation:

$$L_{sd} \sim 10^{49}(B/10^{15}G)^2(P/1ms)^{-4}ergs^{-1}. \tag{5.3}$$

where P is the magnetar's period and B the magnetic field. Using typical magnetar magnetic fields of $10^{14} - 10^{15}$ G and a newborn magnetar period of $\sim$1 ms, the luminosity calculated is on the order of 10^{49} erg/s. This enormous spin-down power provides power for strong particle acceleration in the magnetosphere and wind of the magnetar. If we consider that the outflow particles are mainly protons, their acceleration can lead to hadronic processes, which would produce gamma-rays. Pions are mainly produced through the following processes:

$$p + \gamma \rightarrow \Delta \rightarrow n + \pi^{+}. \tag{5.4}$$

$$p + \gamma \rightarrow \Delta \rightarrow p + \pi^{0}. \tag{5.5}$$

The neutral pions decay to high-energy γ rays with energies $E_\gamma \sim 0.1 E_p \sim 10^3$ TeV (where E_p is the energy of the initial proton in Equation 5.5). However, these gamma rays are subject to pair production through interaction with surrounding thermal ultra-violet radiation. These interactions will result in e^+/e^- cascades. These cascades are a chain reaction between the inverse Compton scattering (ICS) from the e^+/e^- pairs on the other photons, which will then pair produce, etc... The estimated characteristic length for pair production is of the order of 10^8 cm. This value is much smaller than the size of the emission region, which is of the order of 10^{14} cm [121]. Therefore, most TeV photons will not escape and will be reprocessed through ICS. In order to avoid pair production, the gamma-ray energy must be below the pair production threshold. The latter can be determined by

$$E_{ph} E_\gamma \approx 2(m_e c^2)^2/(1 - cos\theta) \tag{5.6}$$

where E_{ph} is the energy of the ambient photon, m_e is the mass of the electron and θ is the incident angle of the primary gamma with the ambient photon. The characteristic energy is estimated to be:

$$E_\gamma \sim 2(m_e c^2)^2/E_{ph} \tag{5.7}$$

which gives ~25 GeV, using $E_{ph} \sim 10$ eV (from the estimated emission region temperature of $\sim 10^5$ K [142]). Photons with energy $E_\gamma \simeq 25$ GeV cannot be detected by any current ground-based Cherenkov telescopes, but could be detected by the *Fermi* satellite.

Note that very high energy gamma rays could be produced from the ultra-relativistic neutrons created in the process shown in Equation 5.4. These neutrons propagate through the wind and may interact with the material from the ejecta. Neutrons escaping the ejecta without interactions, can produce TeV electrons through $n \rightarrow p + e^- + \bar{\nu_e}$. The decay time is long enough to occur outside the ejecta because the neutrons are ultrarelativistic, with decay time in the observer's frame of 886 γ_n ~300 yr. The TeV electrons may subsequently upscatter photons up to TeV energies through ICS on the ambient photons (from CMB, IR or optical background). Nevertheless, since the flux of TeV electrons produced is $\sim 10^{-3}$ times the flux of the neutrons, the resulting TeV gamma-ray flux would be very small.

Model for SGR giant flares

A model has been proposed to describe TeV gamma-ray emission from SGR giant flares [72]. SGRs produce non-thermal radiation during bursts (small or large).

The energetics and the non-thermal spectra observed in giant flares support the idea of efficient particle acceleration. During a major flare, the large-scale magnetic field configuration is changed suddenly (see Section 5.1.1), and this change could accelerate protons which would induce TeV gamma-ray production through neutral pion decay. Note that gamma rays could also be produced via electromagnetic processes (ICS from VHE electrons), assuming there are sufficient low energy photons available.

From Beppo-SAX observations of the SGR 1900+14 giant flare, the observed spectrum (during the first 68 s of the flare) can be fitted with an optically thin thermal bremsstrahlung law and a power law over the 40-700 keV range [69]. Varying the index of the power law between -0.73 and -2.0 does not affect dramatically the fit [72]. Therefore, an extrapolation (from the first 68 s) to TeV energies can be done. Here, only the most conservative case will be described using a power-law index of -2.0. At TeV energies, the predicted differential flux then becomes $F_\gamma = 3.29 \times 10^5$ $\mathrm{cm^{-2}s^{-1}TeV^{-1}}$. Since most of the energy is emitted in the first ~ 0.3 s of the burst, the flux is derived for this time interval. At energies above 400 GeV (energy at which VERITAS is sensitive), the integrated flux is 8.23×10^{-7} $\mathrm{cm^{-2}s^{-1}}$. This corresponds to 8000 times the Crab Nebula flux in this energy range.

Such intensity would be easily detectable by ground-based Cherenkov telescopes. The problem is the short duration of the most energetic part of the flare. To catch a flare lasting less than one second is practically impossible for Cherenkov telescopes due to their small field of view and their relatively long slewing time. However, if the outbursting SGR happened to be in the field of view of the telescope, this flare would definitely be detectable, even if the flare is extremely short.

Model for magnetars in binary systems

The third model presented here is for the case of a magnetar in a binary system [20]. Such a system has not been observed to date, but recent observations in the LSI +61 303 system show indications of SGR behavior from the compact object [46]. If confirmed, this would give strong support to this theoretical model. Indeed, LS I +61 303 has been detected at TeV energies (see Section 6.2.3) and none of the TeV emission theoretical models have been validated yet.

This model considers a compact binary system containing a magnetar and a massive stellar companion of spectral type O or B. The companion star matter can be accreted onto the magnetar (see Section 6.1 for details on accretion). The accreting matter interacts with the rotating neutron star magnetosphere (pulsar wind) creating a very turbulent and magnetized transition region. This region offers good conditions for particle acceleration to high energies.

In this model, only leptonic acceleration is considered. The electrons are accelerated up to a maximum energy $E_{max} = m_e \gamma_{max}$. Near E_{max}, electrons lose energy mainly by synchrotron radiation (X-ray emission) in the magnetic field in the transition region. There is also ICS of the thermal photons from the massive star (TeV emission) occurring in the region although at high energy (near E_{max}), the synchrotron radiation dominates over the ICS. However, at lower energies, the latter starts to dominate. In some cases, the IC gamma rays have large enough energy to initiate pair production on the massive star's ambient radiation. These pairs will then create cascades that will develop and secondary particles will radiate through the synchrotron process.

It is important to mention that in this model, the accretion phase, in which the accreting matter causes the neutron star to lose rotational energy (which is different from the phase where the accretion spins up the magnetar), lasts only of the order of thousands of years [20].

A feature of this model is that, in the case of LS I +61 303, the model predicts no strong modulation along the orbit at GeV energies for most of the parameter sets modeled. However, *Fermi* does see such modulation [2]. Nevertheless, in two particular sets of parameters used in the model, such a modulation is allowed.

Model for pulsar wind nebula powered by magnetars

Finally, the last model for VHE emission from magnetars presented here is based on recent observations. Two magnetar candidates, CXOU J171405.7-381031 and XMMU J173203.3-344518, have been found in TeV-emitting supernova remnants [71].

We have seen that magnetars are not powered by rotational energy loss alone. Instead, the strong magnetic fields responsible for the spin-down luminosity, have increased magnetar's rotational periods to the order of seconds (see Section 5.1.1). Therefore, they are not expected to power TeV pulsar wind nebulae (PWNe) as millisecond pulsars do. Indeed, the spin-down power of magnetars is of the order of $10^{34} - 10^{36}$ erg/s. Millisecond pulsars can provide $10^{36} - 10^{38}$ erg/, enough energy to power TeV emission.

It is possible that particle-dominated winds flow out of the magnetar through the open magnetic field lines, resulting in a shocked PWN. A young magnetar, still having a short period (of the order of 1 ms) and a high spin-down luminosity, could energize a PWN. In such a case, high-energy electrons could escape the intense magnetic field region and radiate TeV gamma rays through ICS of ambient low-energy photons.

It is clear from these different models that VHE emission from magnetars does not emerge naturally from the general magnetar model. However, the VHE emission models presented here show that in some specific stages of the magnetar life or in some particular outburst states, very efficient particle acceleration might occur. Only a handful of magnetars are known. The particular conditions required in the described models might be realized in a larger population of objects.

5.2 VERITAS observations

VERITAS obtained data on three magnetars; 4U 0142+61, 1E 2259+586 and SGR 0501+4516. An overview of these objects is presented here. The main characteristics are summarized in Table 5–1. The details of the VERITAS observations are also given below.

Table 5–1: Characteristics of the magnetars presented.

Object	4U 0142+61	1E 2259+586	SGR 0501+4516
Magnetic field (G)	1.3x10^{14}	6.3x10^{13}	3x10^{14}
Characteristic age (y)	7.0x10^{4}	2.3x10^{5}	1.8x10^{4}
Distance (kpc)	3.6	4.0	1.5
Period (s)	8.69	6.98	5.76
Period derivative (10^{-13} ss^{-1})	20	4.84	67

5.2.1 4U 0142+61

4U 0142+61, the brightest known AXP, is an isolated magnetar located at a distance of 3.6 kpc [49]. The magnetar's period is 8.69 s and the period derivative is 0.2 x 10^{-11} ss^{-1} [37][70]. Its magnetic field is 1.3 x 10^{14} G and its characteristic age is 7 x 10^{4} years* . This magnetar entered a state of X-ray bursting activity in April 2006 that lasted until February 2007 [64]. During this active state, several bursts were detected: one in April 2006, four in June 2006 and one in February 2007. The top panel of Figure 5–3 shows the X-ray light curve during the six bursts. Furthermore, this magnetar is surrounded by a gaseous fallback disk [171][52].

The VERITAS observations of 4U 0142+61 were part of a successful proposal for the first dedicated TeV observations of a magnetar within VERITAS. This particular magnetar was chosen for several reasons. First, it is the brightest AXP in the X-ray band. Second, since this magnetar is isolated, any potential emission could be dissociated from a surrounding supernova remnant. Finally, the presence of the fallback disk may provide material for efficient acceleration. The observations were performed from 2008 October 7 to October 22 for a total of 6 h of exposure time under moderate moonlight. On October 24, gamma-ray burst (GRB) observations were triggered 0.75° away from 4U 0141+61, adding 3.25 h of dark time data to our dataset.

---

[*] Using the relation $\tau_c = P/2\dot{P}$. This equation comes from the assumption of a constant magnetic field and that the period at birth is considerably smaller than the actual period.

5.2.2 1E 2259+586

1E 2259+586, the first AXP discovered [19], is a magnetar surrounded by a large (0.5°) supernova remnant (CTB 109) at a distance of 4 kpc [164]. The magnetar's period is 6.98 s, its period derivative is 4.84 x 10^{-13} ss^{-1} and its magnetic field is 6.3 x 10^{13} G. Its characteristic age is 2.3 x 10^{5} years. The magnetar was observed by *RXTE* and *XMM* during a major X-ray outburst in June 2002 which lasted for 4 h [111][181]. During this burst, significant changes from the persistent emission were observed in the spectra and in the timing. The middle panel of Figure 5–3 shows the X-ray light curve during the burst on 2002 June 18.

VERITAS 1E 2259+586 dark time observations were dedicated to the supernova remnant surrounding the magnetar, CTB109. A total of 7 h of data was taken, although only 4.3 h were usable after quality selection.

5.2.3 SGR 0501+4516

SGR 0501+4516 has been recently (August 2008) discovered [81][18]. The period of this magnetar is 5.76 s [66], its period derivative is 6.7 x 10^{-12} ss^{-1} and its magnetic field is 3 x 10^{14} G [180]. It has been shown that the magnetar was probably born in the supernova HB9 [58], in which case its distance would be 1.5 kpc. In August 2008, at the time of its discovery, the SGR was in a bursting state that lasted over four months. The bottom panel of Figure 5–3 shows the X-ray light curve during the burst on the 2008 August 26.

VERITAS data on SGR 0501+4516 were obtained from dark time observations dedicated to a blazar 1.9° away from the SGR, although observations further than

1.5° away from the SGR were not used due to the low camera acceptance at these distances (see Section 4.5.1). A total of 1.3 h of data were usable for the SGR analysis.

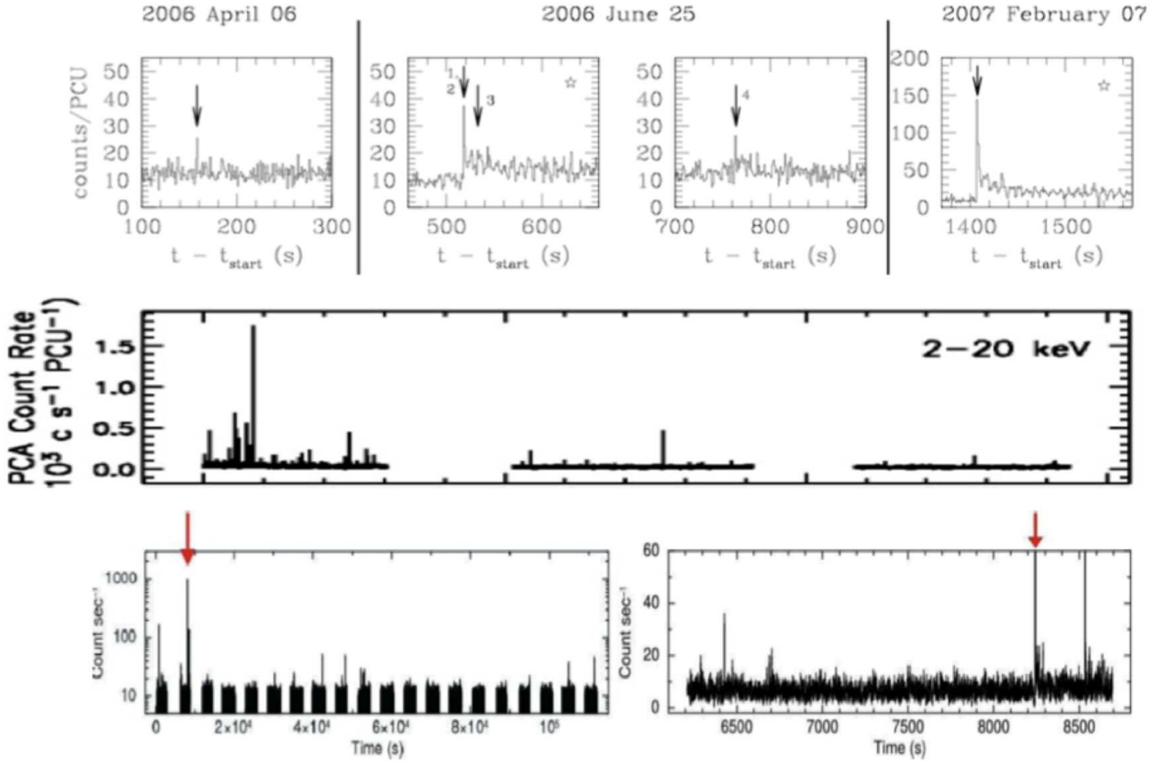

Figure 5–3: Top panel: Light curve of 4U 0142+61 in the 2-20 keV band from RXTE during its bursting activity of 2006-2007. Figure taken from [39]. Middle panel: Light curve for 1E 2259+586 in the 2-20 keV band from RXTE during the 2002 June 18 outburst. Figure taken from [111]. Bottom panel: Light curve of SGR 0501+4516 in the 0.4-10 keV band from SUZAKU for the burst of 2008 August 26. The right panel is a zoom in around the burst. The arrows indicate the same time. Figure taken from [51].

The details of the VERITAS magnetar observations are presented in Tables 5–2, 5–3 and 5–4; each run is 20 min long. The angular distance between the object and the telescope pointing is indicated in order to show how the exposure time is weighted by the camera acceptance (see Section 4.5.1).

Table 5–2: Details of 4U 0142+61 observations.

Run number	Date yyyymmdd	Elevation (°)	Dark/moonlight	Angular distance between object and pointing (°)
42046	20081007	53	moonlight	0.5
42047	20081007	54	moonlight	0.5
42048	20081007	57	moonlight	0.5
42079	20081007	53	moonlight	0.5
42080	20081007	56	moonlight	0.5
42081	20081007	57	moonlight	0.5
42082	20081007	59	moonlight	0.5
42104	20081007	59	moonlight	0.5
42105	20081007	59	moonlight	0.5
42106	20081007	59	moonlight	0.5
42107	20081007	60	moonlight	0.5
42225	20081007	56	moonlight	0.5
42226	20081007	58	moonlight	0.5
42227	20081007	59	moonlight	0.5
42252	20081007	59	moonlight	0.5
42253	20081007	59	moonlight	0.5
42254	20081007	60	moonlight	0.5
42308	20081007	60	moonlight	0.5
42309	20081007	59	moonlight	0.5
42391	20081007	58	dark	0.6
42392	20081007	60	dark	1.1
42393	20081007	60	dark	1.2
42394	20081007	60	dark	0.4
42395	20081007	59	dark	0.6
42396	20081007	60	dark	1.1
42397	20081007	58	dark	1.2
42398	20081007	56	dark	0.4
42399	20081007	55	dark	0.6

Table 5–3: Details of 1E 2259+586 (CTB 109) observations.

Run number	Date yyyymmdd	Elevation (°)	Dark/moonlight	Angular distance between object and pointing (°)
38184	20071204	61	dark	0.5
38219	20071205	61	dark	0.5
38220	20071205	60	dark	0.5
38254	20071206	62	dark	0.5
38256	20071206	61	dark	0.5
38510	20071230	52	dark	0.5
38529	20071231	56	dark	0.5
38530	20071231	53	dark	0.5
38531	20071231	51	dark	0.5
38550	20080101	56	dark	0.5
38552	20080101	52	dark	0.5
38708	20080111	48	dark	0.5
38750	20080112	46	dark	0.5

Table 5–4: Details of SGR 0501+4516 observations.

Run number	Date yyyymmdd	Elevation (°)	Dark/moonlight	Angular distance between object and pointing (°)
41957	20081003	76	dark	1.43
42368	20081023	66	dark	1.43
42480	20081026	67	dark	1.23
42482	20081026	57	dark	1.23

5.3 Results of VERITAS magnetar observations

5.3.1 Results

The analysis was performed using EVNDISP-330 for 4U 0142+61 and 1E 2256+586 and EVNDISP-346 for SGR 0501+4516, using the *Ring Background Model* and *standard cuts* (see Chapter 4 for details on the analysis, background models and cuts). *Standard* cuts are used to search for VHE gamma-ray emission when assumption of a Crab-like source is made on the flux and spectrum of a source.

4U 0142+61

No gamma-ray emission was detected by VERITAS. The significance skymap is shown in Figure 5–4. The significance at the magnetar position is -2.6 σ.

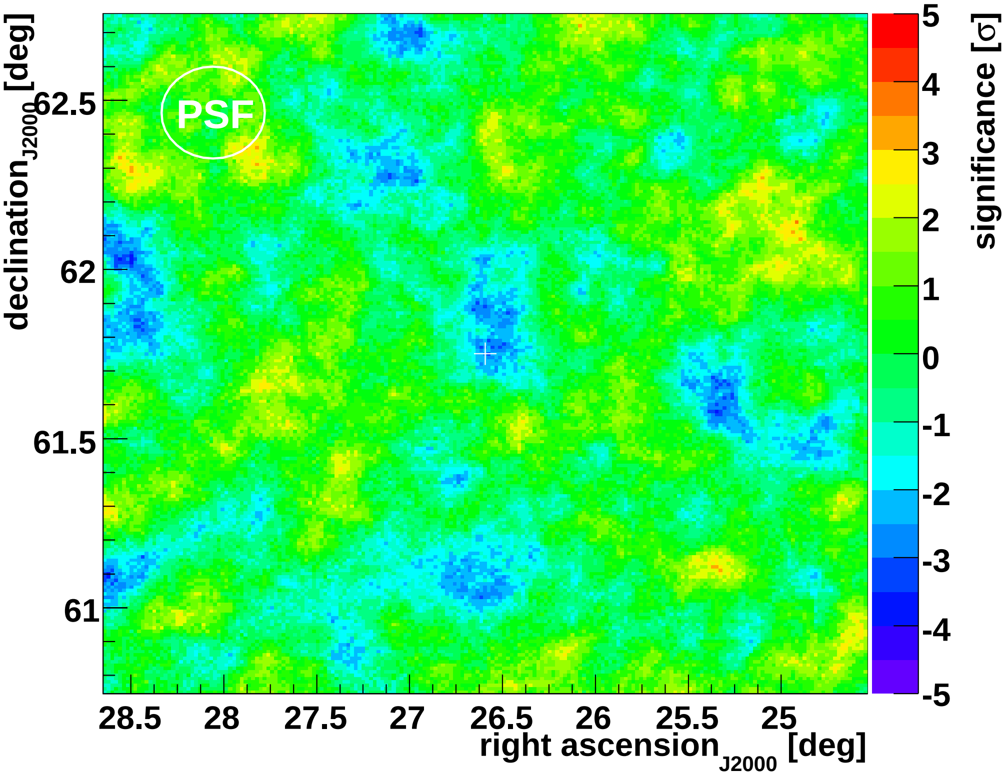

Figure 5–4: Significance skymap for 4U 0142+61 in J2000 equatorial coordinates. The white cross shows the object nominal position and the white circle at the top left represents the point spread function (PSF) of the instrument.

The significance distribution, shown in Figure 5–5, is well fitted by a Gaussian of mean 0 and sigma of 1, corresponding to a null hypothesis (no signal). From this result, a 99% confidence level (C.L.) flux upper limit, for energies above 400 GeV, of

8.68 x 10^{-13} cm^{-2} s^{-1} was calculated, assuming a Crab-like spectrum. This represents less than 0.9% of the Crab Nebula flux. This result is for the X-ray quiescent phase, since the magnetar has not been detected in an active state since 2007. More details on the results are summarized in Table 5–5.

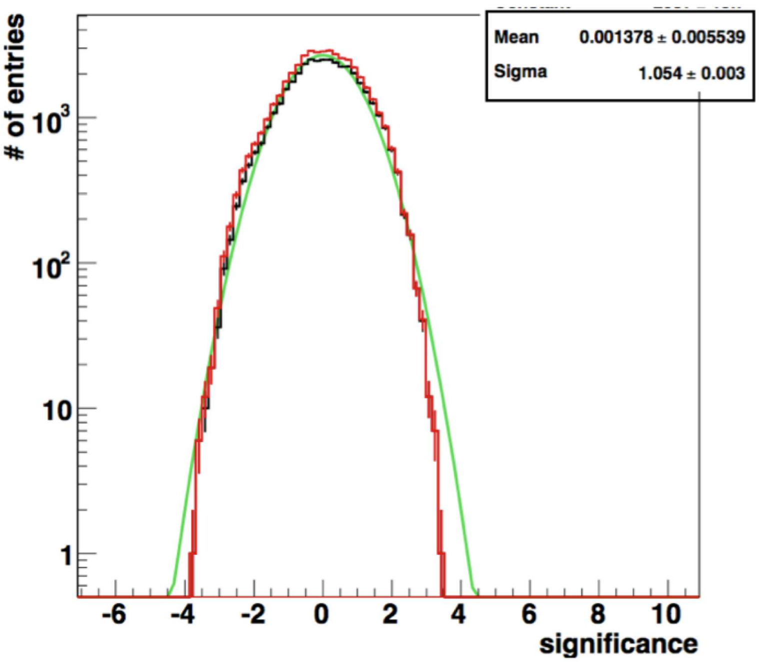

Figure 5–5: The significance distribution of the 4U 0142+61 skymap. The red curve represents the significance distribution for all sky map bins. The black curve represents the significance distribution of all the skymap bins except the bins of the source (contained in a radius of 0.4°). The fit to the black curve of a Gaussian distribution is shown with the green line.

1E 2259+586

The VERITAS observations show no gamma-ray emission from 1E 2259+586. The significance skymap is shown in Figure 5–6. The significance at the source position is 1.5 σ.

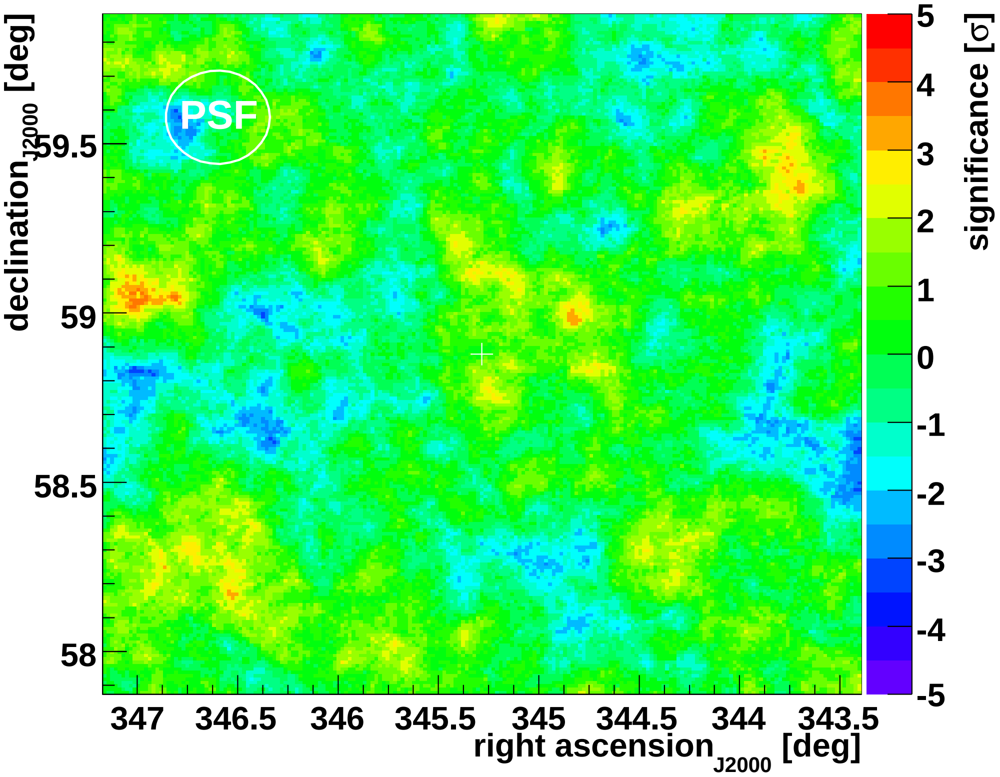

Figure 5–6: Significance skymap for 1E 2259+586 in J2000 equatorial coordinates. The white cross shows the object position and the white circle at the top left represents the point spread function (PSF) of the instrument.

The significance distribution shown in Figure 5–7 is well fitted by a Gaussian of mean 0 and sigma of 1, indicating clearly a normal distribution with no signal. Assuming a Crab-like spectrum, calculation gives a 99% C.L. flux upper limit of

2.49 x 10^{-12} cm^{-2} s^{-1}, corresponding to less than 2.5% of the Crab Nebula flux, for energies above 400 GeV, for the quiescent phase. More details on the results are summarized in Table 5–5.

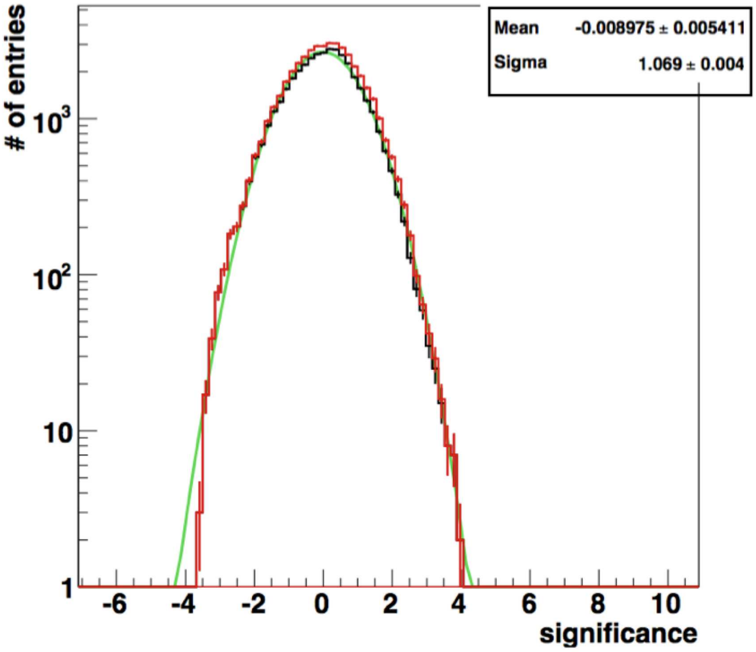

Figure 5–7: The significance distribution of the 1E 2259+586 skymap shown in Figure 5–6. The red curve represents the significance distribution for all sky map bins. The black curve represents the significance distribution of all the skymap bins except the bins of the source (contained in a radius of 0.4°). The fit to the black curve of a Gaussian distribution is shown with the green line.

SGR 0501+4516

The significance skymap for SGR 0501+4516 is shown in Figure 5–8. The significance at the source position is 0.6 σ.

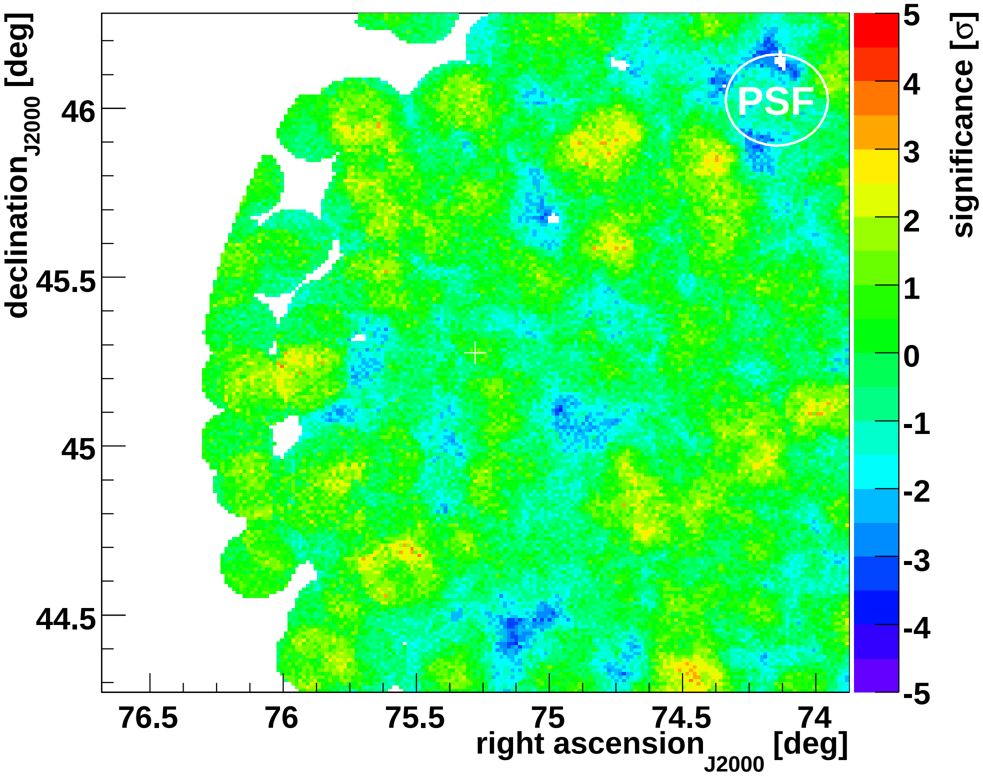

Figure 5–8: Significance skymap for SGR0501+4516 in J2000 equatorial coordinates. The white cross shows the object position and the white circle at the top right represents the point spread function (PSF) of the instrument.

No gamma-ray emission was detected by VERITAS. The significance distribution shown in Figure 5–9 is well fitted by a Gaussian of mean 0 and sigma of 1. From this result, a flux upper limit, for energies above 400 GeV, at 99% C.L. of 5.22

x 10^{-12} cm^{-2} s^{-1} has been calculated. This represents less than 6.2% of the Crab Nebula flux.

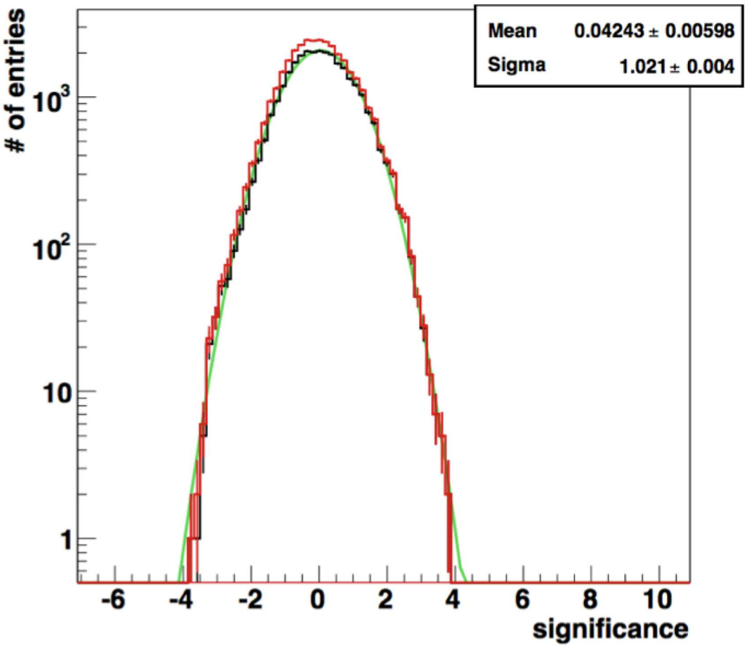

Figure 5–9: The significance distribution of the SGR0501+4516 skymap shown in Figure 5–8. The red curve represents the significance distribution for all sky map bins. The black curve represents the significance distribution of all the skymap bins except the bins of the source (contained in a radius of 0.4°). The fit to the black curve of a Gaussian distribution is shown with the green line.

Since the observations used for this analysis are on average 1.3° away from the source, the total exposure time has to be scaled by the acceptance curve of the camera (see Section 4.5.1). Therefore, the 1.3 h exposure represents only 0.5 h at typical VERITAS sensitivity (for observations in *wobble* mode of 0.5°). This is a very short exposure, but sources emitting at the level of 10% of the flux of the Crab

Nebula should be detected in this amount of time. The results are summarized in Table 5–5.

Table 5–5: Results on magnetar observations.

Object	Exposure (h)	N_{on}	N_{off}	α	Significance (σ)	99% C.L. U.L.(E>400 GeV) (cm^{-2} s^{-1}) [Crab Units]
4U 0142+61	9.25	82	454	0.25	-2.9	$8.68\text{x}10^{-13}$ [0.9%]
1E 2259+586	4.27	40	185	0.23	1.5	$2.49\text{x}10^{-12}$ [2.5%]
SGR 0501+4516	1.28	7	5	0.16	0.6	$5.22\text{x}10^{-12}$ [6.2%]

5.3.2 Search for pulsed emission in 4U 0142+61 and 1E 2259+586

Magnetars exhibit pulsed emission in the X-ray band (see Section 5.1.2). Even though no TeV gamma-ray emission has been detected from any of the magnetars observed by VERITAS, a search for pulsed emission could reveal a signal. No pulsations are expected at TeV energies. Indeed, only pulsations from the Crab pulsar have been detected at very high energies by the MAGIC experiment, and the detection was between 25 GeV and 60 GeV [122], which is at much lower energy than the VERITAS energy threshold for this analysis.

A search for pulsed emission has been performed for two of the three magnetars studied: 4U 0142+61 and 1E 2259+586. The ephemeris for SGR 0501+4516 was not available. The X-ray ephemerides for 4U 0142+61 and 1E 2259+586 for the VERITAS observation periods were provided by Prof. Vicky Kaspi and Dr. Rim Dib. These two objects are part of a X-ray monitoring program led by Prof. Kaspi.

Figure 5–10 shows the results of the pulsed emission analysis. No pulsed emission has been found in any of the magnetars analyzed. Since there is no reason why a potential gamma-ray pulsed emission would occur at the same phase as other wavelength pulsed emission, a flat line fit has been done to the data to look for a potential signal.

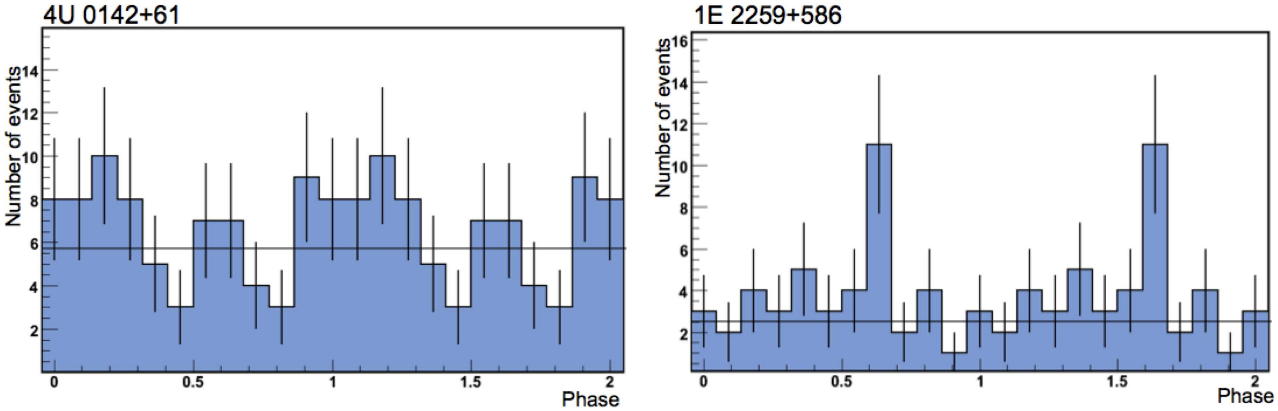

Figure 5–10: Pulsed emission analysis for the magnetars 4U 0142+61 (left panel) and 1E 2259+586 (right panel) for energies above 300 GeV for 4U 0142+61 and above 275 GeV for 1E 2259+586. The solid lines represent the fit of a uniform distribution on the data.

In the case of 4U 0142+61, the uniform distribution fit (with value of 5.5 ± 0.7 events/bin) gives a reduced χ^2 of 1.1, showing a good agreement of the fit with the data. No bin deviates from the fit by more than 1.4 sigma (pre-trials), showing no presence of a signal.

For 1E 2259+586, the uniform distribution fit (with value of 2.7 ± 0.5 events/bin) gives a reduced χ^2 of 1.2, also showing a good agreement of the fit with the data. The highest bin in the plot is 2.5 sigma (pre-trials) away from the fitted line, which is not significant.

5.4 Implications of the VERITAS results

The VERITAS results presented at the *31st International Cosmic-Ray Conference* in July 2009 were the first published results on magnetar observations in the VHE band [68]. No gamma-ray emission has been detected by VERITAS from any of the observed magnetars; such high-energy emission was not expected during quiescence. The results give strength to the current models of magnetars, which do not predict VHE emission. Note that the *Fermi*/LAT instrument has not detected quiescent GeV emission from magnetars either [168], corroborating this conclusion.

As mentioned in Section 5.1.2, models suggesting VHE emission from magnetars are based on particular states of the neutron star (*e.g.* in binary systems, fast-spinning, in a flaring state, etc). In the case of the magnetars presented here, none meets the criteria for the models with fast-spinning magnetars or magnetars in binary systems. The only potential model left to test is the one suggesting VHE emission during major outbursts.

Magnetar major outbursts are rare events. Indeed, only three giant flares from SGRs have occurred in the last 30 years. Smaller outbursts are a slightly more frequent, but still occur at a low rate (estimated to be approximately one per year considering all monitored magnetars and previous bursting activities).

No observed magnetars were in an outburst state during the VERITAS observations, although, in the case of SGR 0501+4516, the VERITAS observations were performed less than two months after the outburst leading to its discovery. The intensity of the X-ray flux after 40 days (period of the first VERITAS observations) had decreased significantly, as shown in Figure 5–11.

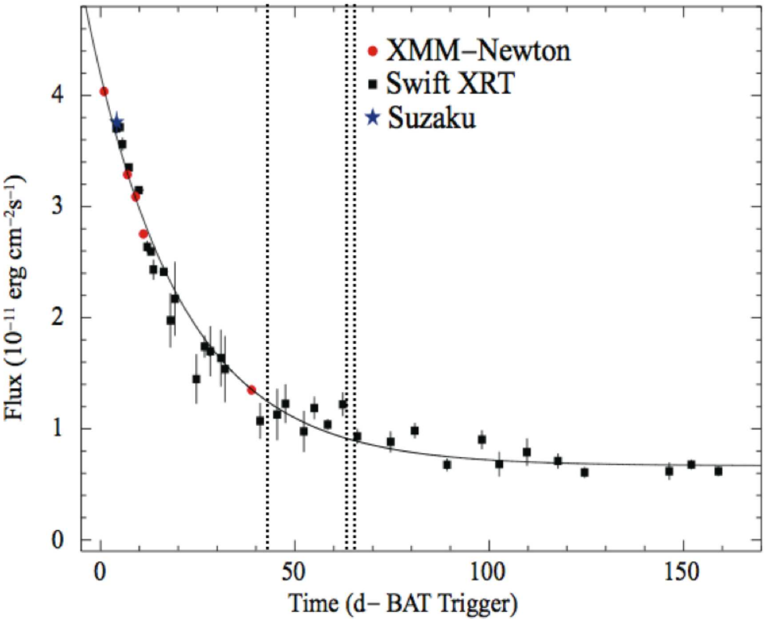

Figure 5–11: The outburst decay of the persistent X-ray flux of SGR 0501+4516 fitted with an exponential function. The BAT trigger corresponds to MJD 54700.0 12:41:50.00 (UT). The fluxes are in the 1-10 keV energy range for XMM-Newton, *Swift* and *Suzaku*. The vertical dashed lines indicate the days of the VERITAS observations. Figure adapted from [141].

In addition, it is clear from Figure 5–12, showing the Integral observations in the 18-60 keV band, that the intensity of the emission had faded considerably after 10 days. Therefore, since the VERITAS observations were done too long after the outburst, only weak constraints can be put on VHE emission predictions during outbursts. Since most of the outburst energy is released at the beginning of the flare, it is important that the observations are made as soon as possible after the burst detection.

The results presented here show that magnetars, in quiescence, do not emit strongly in the TeV regime. This does not contradict the current magnetar models.

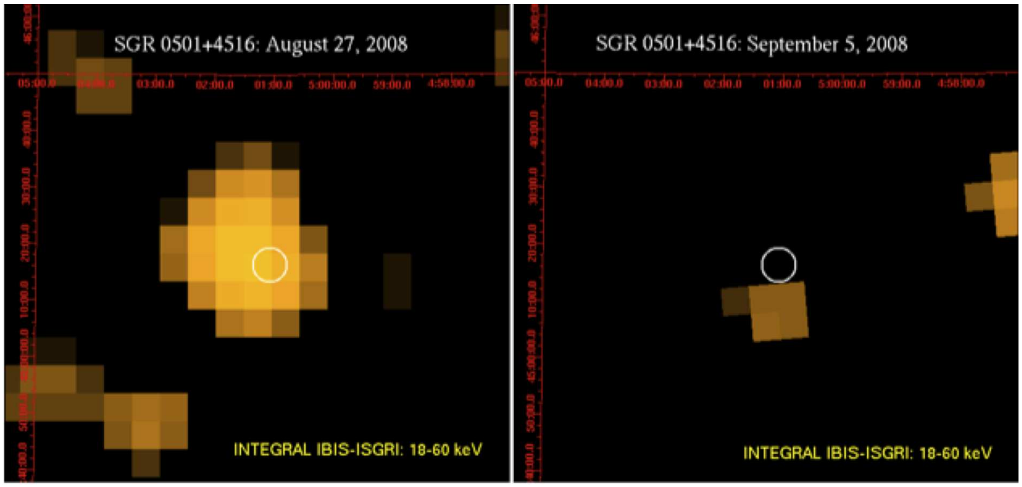

Figure 5–12: The INTEGRAL data of SGR 0501+4516 shows that a higher energy component was present early on (5 days after the start of the outburst) (left panel), but quickly fell below threshold (right panel). Copyright: ESA/INTEGRAL/IBIS-SIGRI (Rea et al. 2009).

It has been discussed in this chapter that VHE gamma rays could be emitted by magnetars in particular conditions, in particular during major outbursts. As a result of this work, observations of magnetars in major outbursts are now part of VERITAS Target of Opportunuity program.

At VERITAS, a program of GRB alerts has been set up. When an X-ray or gamma-ray flare is detected by any of the satellite instruments (*e.g. Swift* or *Fermi*), an alert is sent instantaneously via GCN circulars. These alerts are picked up by VERITAS software which sends information to the observers to slew the telescopes immediately to the flare position. Observations can start in a time scale of the order of a minute (time required to slew the telescopes).

All magnetars have now been included in the GRB alert software. Therefore, any major outburst can potentially trigger VERITAS observations, which will start a minute or so after the trigger. Such observations would be helpful to constrain models that suggest VHE emission during major outbursts.

CHAPTER 6
X-Ray Binaries

X-ray binaries are the brightest X-ray sources in the galaxy. Three of these systems have been recently discovered to be TeV gamma-ray emitters. In this chapter, X-ray binaries will be described, focusing on the known TeV-emitting systems. Data on fifteen binary systems were retrieved from VERITAS archival data and the analysis results will be presented, as well as the implications of the results.

6.1 X-ray binaries

X-ray binaries are systems composed of a compact object, either a neutron star or a black hole, and a stellar companion. The accretion of matter from the companion star onto the compact object is mostly responsible for the X-ray emission, although some systems are powered by the fast rotation of the neutron star. The kinetic energy gained by the matter falling onto the compact object is converted into thermal energy and the X-ray luminosity is well described as black body emission.

Usually in binary systems, the compact object is not detectable optically. Any optical observations of these systems refers to the stellar companion. It is possible to estimate the mass relation between the two objects in binary systems when the velocity curve of the X-ray source is available. Equation 6.1, known as the mass function (f), shows that if the angle of inclination of the orbit plane to the plane of the sky (θ_i) can be obtained, the mass of the compact object (M_X) can be determined. M_0 is the mass of the stellar companion.

$$f(M_X, M_0, \theta_i) = \frac{M_0^3 sin^3\theta i}{(M_X + M_0)^2} \tag{6.1}$$

Several X-ray binaries have been detected in the radio band. It is known that the most efficient mechanism to produce intense radio emission is the synchrotron emission process. This radio emission from binary systems is thus explained by a population of non-thermal relativistic electrons.

X-ray binaries can be subdivided into two groups: High Mass X-ray Binaries (HMXBs) and Low Mass X-ray Binaries (LMXBs). These two sub-groups are described below. There is another sub-division made among X-ray binaries based on the interaction between the compact object and the stellar companion. Indeed, in some systems, the accretion of matter onto the compact object may lead to the formation of relativistic jets. These particular systems are then called microquasars. Both HMXBs and LMXBs can be microquasars. These systems will be discussed in detail in Chapter 7.

6.1.1 High Mass X-ray Binaries

HMXBs are systems in which the companion is a massive star ($\sim 8M_\odot - 20M_\odot$). The stellar companion is usually either a Be star (B star with emission lines) or a supergiant O or B star. In the first case, where the companion is a Be star, accretion from the star to the compact object will occur via the Be star decretion disk. In a typical system, every time that the compact object passes through the disk, matter is accreted. See Figure 6–1 for an illustration of the process. These systems are known to have transient behavior. In the second case, where the stellar companion is a O or B supergiant, two scenarios can lead to accretion of matter: by Roche lobe overflow and by strong stellar wind. The Roche lobe overflow occurs when, at a certain point in its evolution, the star's outer envelope becomes large enough to exceed its Roche lobe. This overflow forces the matter to accrete onto the compact object. The accretion through stellar wind occurs when the strong wind from the star interacts with the gravitational potential of the compact object. Figure 6–2 shows an illustration of these two processes. Systems accreting through these two scenarios are persistent X-ray emitters and show significant variability. To date 114 HMXBs are known [118].

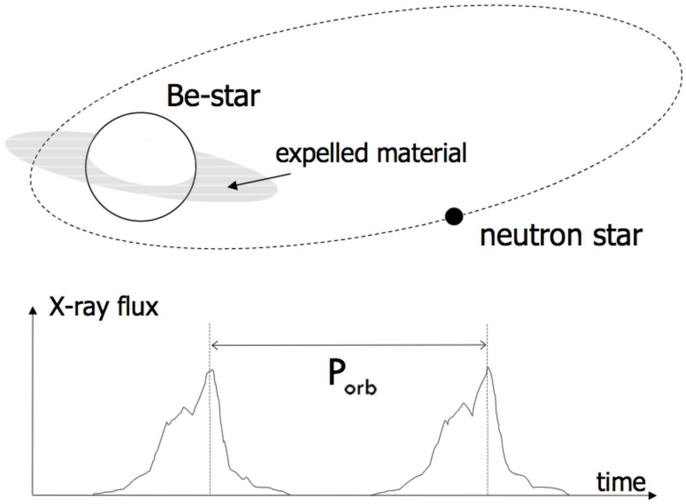

Figure 6–1: Schematic model of a Be-star X-ray binary system. The neutron star moves in an eccentric orbit around the Be-star which is not filling its Roche lobe. However, near the periastron passage the neutron star accretes circumstellar matter, ejected from the rotating Be-star, resulting in an X-ray burst lasting several days. Figure taken from [156].

6.1.2 Low Mass X-ray Binaries

LMXBs are systems containing a companion star of low mass ($\leq 2M_{\odot}$) and of type later than A. The compact object can be either a black hole or neutron star. The mass transfer from the stellar companion onto the compact object in these systems occurs via Roche-lobe overflow, as described above (see Figure 6–2). Most of the LMXBs are X-ray transients due to instabilities in the accretion onto the compact object or to variable ejection episodes from the stellar companion. To date, 185 LMXBs are known [119].

6.2 TeV emitting binary systems

It has recently been discovered that X-ray binaries can also be TeV gamma-ray emitters. Three systems (PSR B1259-63, LS 5039 and LS I +61 303) have been discovered to emit in the TeV band. It is not clear why, of all the binary systems in the Galaxy observed in the GeV-TeV bands, only three have been detected at very high energies. As we will see below, there are no obvious characteristics that make these systems unique. Furthermore, there is no strong correlation between the individual characteristics of the three systems that could demonstrate with certainty the TeV emission criteria. In this section, a detailed description of the three systems will be given, as well as a highlight of the characteristics that might be responsible for the VHE emission.

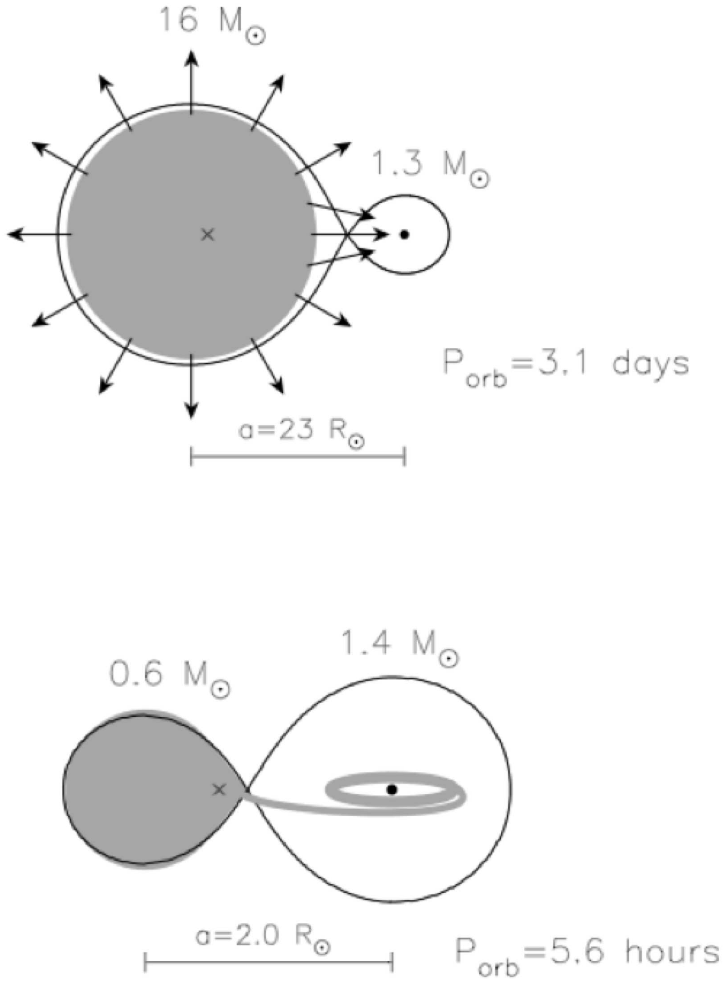

Figure 6–2: Top: Illustration of accretion through stellar wind. The neutron star is fed by a strong high-velocity stellar wind. Bottom: Illustration of the Roche lobe overflow. The neutron star is surrounded by an accretion disk which is fed by Roche-lobe overflow. Figure taken from [156].

6.2.1 PSR B1259-63

PSR B1259-63 is a system composed of a pulsar and a Be star. The pulsar has a period of 47.7 ms, a period derivative of 2.28 $\times 10^{-15}$ ss^{-1} and a magnetic field of $\sim$3.3 $\times 10^{11}$ G. The system evolves on an highly eccentric orbit (e = 0.87) of 1237 days [105][106], with an inclination angle of ∼36° [177]. Figure 6–3 shows an illustration of the system. The distance to the system is estimated to be between 1.5 kpc and 4.5 kpc [107][158].

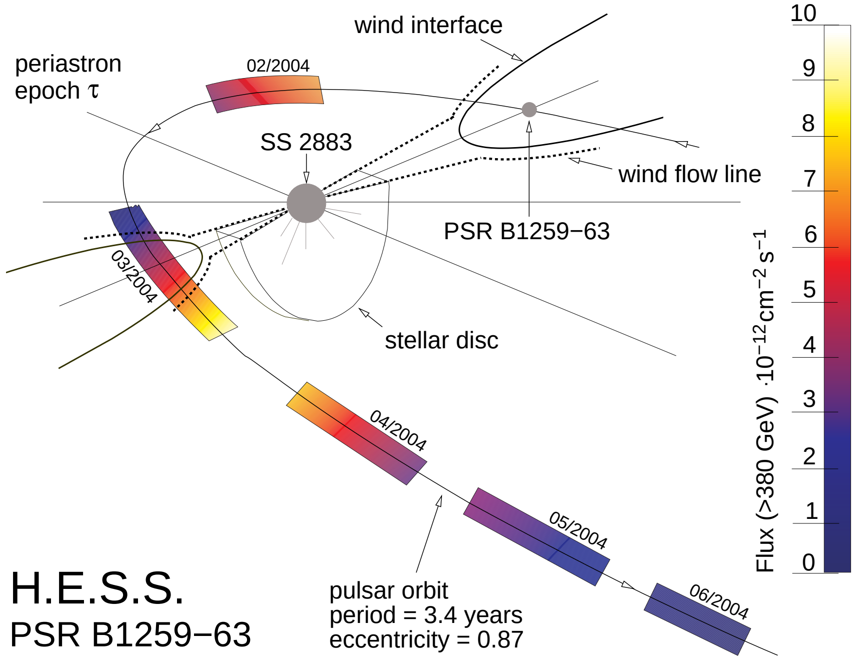

Figure 6–3: Sketch of the orbit of PSR B1259-63 with respect to the line of sight. The pulsar approaches the equatorial disk prior to periastron while it is "behind" the companion star and turns toward the observer before it crosses the disk after periastron for the second time. The color gradient bars along the orbit indicate the period of H.E.S.S. observations and show the integral VHE γ-rayflux. Figure taken from [10].

The pulsar passes through the equatorial stellar wind (the decretion disk) of the companion twice during the orbit; ∼13 days before periastron and ∼17 days after periastron [33], as shown in Figure 6–3. The X-ray emission from the system can be explained by the interaction of the pulsar wind and the equatorial disk of the Be star. The $e^{\pm}$ pairs escaping the pulsar magnetosphere are accelerated at the pulsar wind termination shock and interact with the magnetic field and thermal radiation of the massive star. The X-ray and soft γ-ray emission is produced via synchrotron losses or ICS processes.

The H.E.S.S. collaboration discovered that PSR B1259-63 also emits in the TeV gamma-ray regime [10]. The TeV emission occurs before and after periastron passage as seen in the light curve presented in Figure 6–4. From the same figure, there is a correlation between the highest radio emission point and the highest TeV emission point, suggesting a common acceleration mechanism for both energy bands. The radio data were taken contemporaneously with the TeV observations [108]. The acceleration involved in this system will be described in detail in Section 6.3. The integrated flux detected by H.E.S.S. is $(4.0 \pm 0.4) \times 10^{-12}$ cm^{-2}s^{-1} at energies above 380 GeV [10].

Note that in the GeV gamma-ray band, PSR B1259-63 has not been detected yet. This may be because, since the launch of the *Fermi* satellite (June 2008), the pulsar has not passed through the stellar disk, from where the emission is expected. The next passage will be in December 2010.

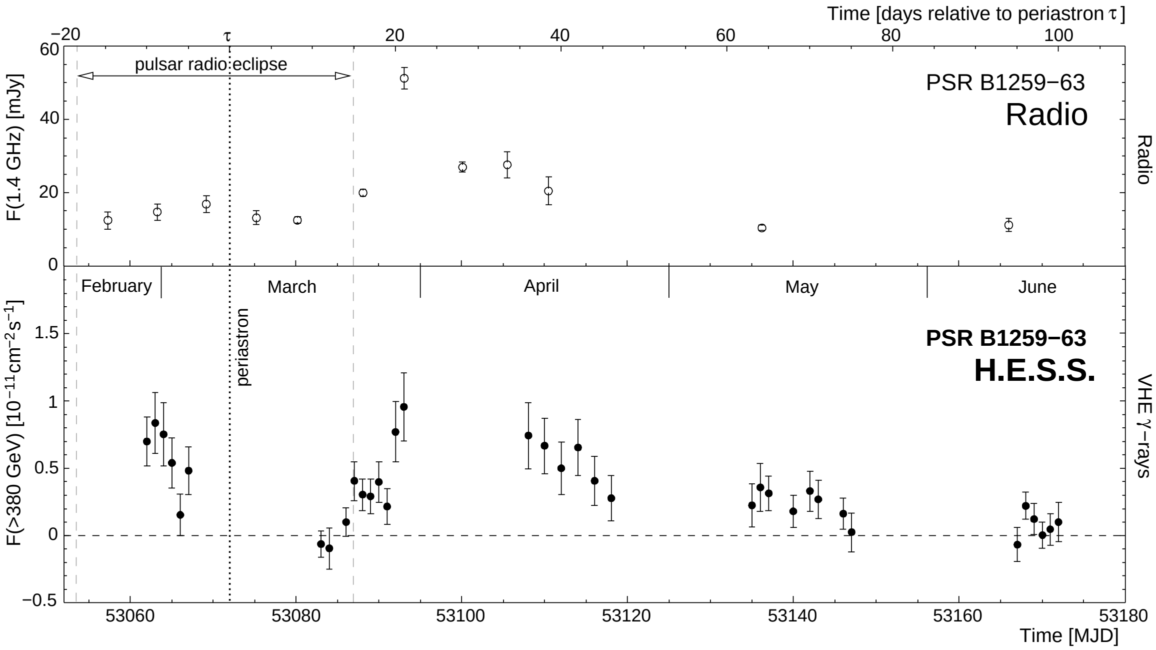

Figure 6–4: VHE γ-ray and radio light curves of PSR B1259−63 around its periastron passage (τ=0, dotted vertical line). Upper panel, open points: Flux density of the transient unpulsed radio emission at 1.4 GHz. The pulsed radio emission was eclipsed in the time interval between $\sim \tau - 18$,days and $\sim \tau + 15$ days, indicated by the two dashed vertical lines. Lower panel, full points: Daily integral flux above 380 GeV as measured by H.E.S.S.. Figure taken from [10].

6.2.2 LS 5039

LS 5039 is a binary system containing a compact object and a massive star of type O. The nature of the compact object, black hole or neutron star, is still undetermined. The system has an orbital period of 3.9 days with an eccentricity of $e = 0.35$ and is located 2.5 kpc away [28]. The mass of the compact object is between 1.4 and 5 $M_{\odot}$, depending on the inclination angle (see Equation 6.1) and the angle of inclination toward the observer could be ∼20° for a black hole or ∼60° for a neutron star.

There are observations and arguments that favor the scenario where the compact object is a black hole, while others favor the pulsar scenario. The system shows jet-like structures at radio wavelengths, see Figure 6–5. The bipolar jet-like structure suggests the presence of an accreting black hole. However, the change in morphology between the left and the right panels (representing two different orbital phases) in Figure 6–5 cannot be explained easily with the presence of a black hole. The pulsar scenario also has caveats, requiring the inclination of the binary system to be very close to the upper limit imposed by the absence of X-ray eclipses.

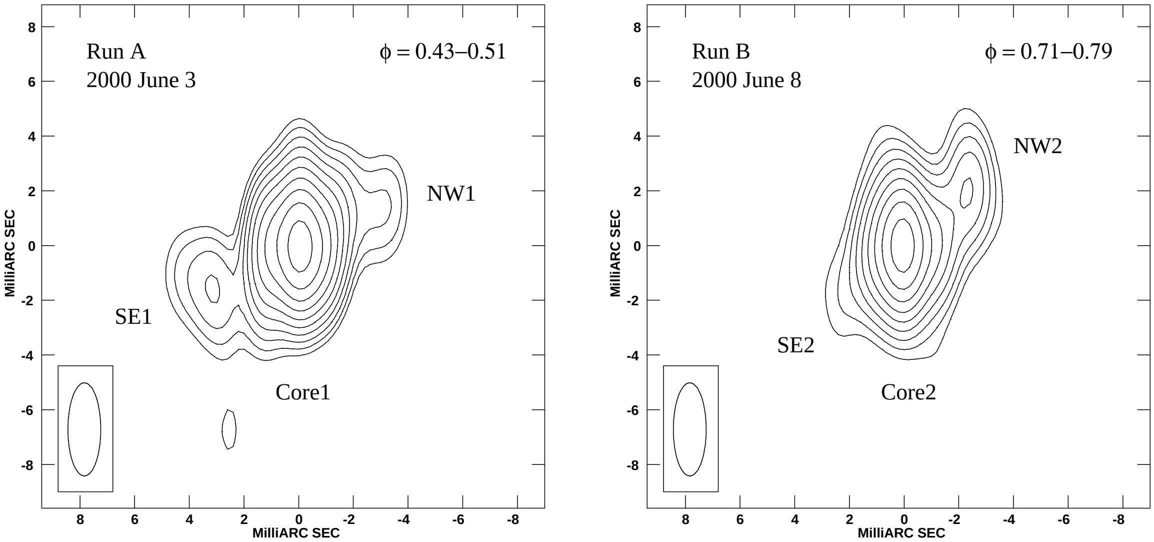

Figure 6–5: VLBA maps at 5 GHz of LS 5039 for two different observations [147]. The presence of potential opposite relativistic jets is visible on each side, identified by the letters SE and NW.

LS 5039 was associated with the unidentified EGRET GeV source 3EG J1824-1514 [139] and a theoretical model predicted TeV emission from this source [25]. The H.E.S.S. discovery of TeV gamma-ray emission from LS 5939 confirmed the source as a VHE emitter [11]. The H.E.S.S. experiment observed VHE gamma-ray emission with a 3.9 day periodicity. Figure 6–6 shows the orbital geometry of the system.

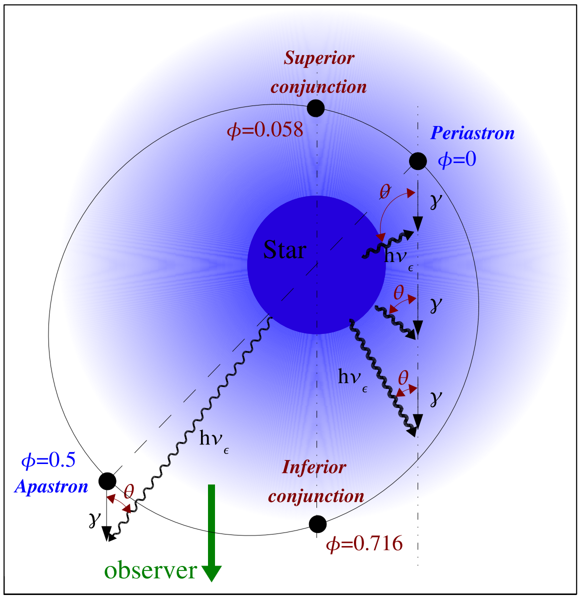

Figure 6–6: Orbital geometry of LS 5039 viewed from directly above. Figure taken from [13].

The maximum intensity of the emission occurs during the phase of the compact object inferior conjunction and the minimum during the phase of superior conjunction (see left panel in Figure 6–7). The integrated flux above 200 GeV observed by H.E.S.S. during inferior conjunction is $(2.28 \pm 0.1) \times 10^{-12}$ cm^{-2}s^{-1} and during superior conjunction is $(0.91 \pm 0.1) \times 10^{-12}$ cm^{-2}s^{-1} [13].

H.E.S.S. also found that the spectrum changed between inferior and superior conjunction (see right panel in Figure 6–7). Indeed, during inferior conjunction, the spectrum is consistent with a hard power-law $dN/dE = E^{-\Gamma}$ ($\Gamma_{VHE} = 1.85 \pm 0.06_{stat} \pm 0.1_{syst}$) with exponential cutoff at $E_0 = 8.7 \pm 2.0$ TeV. At superior

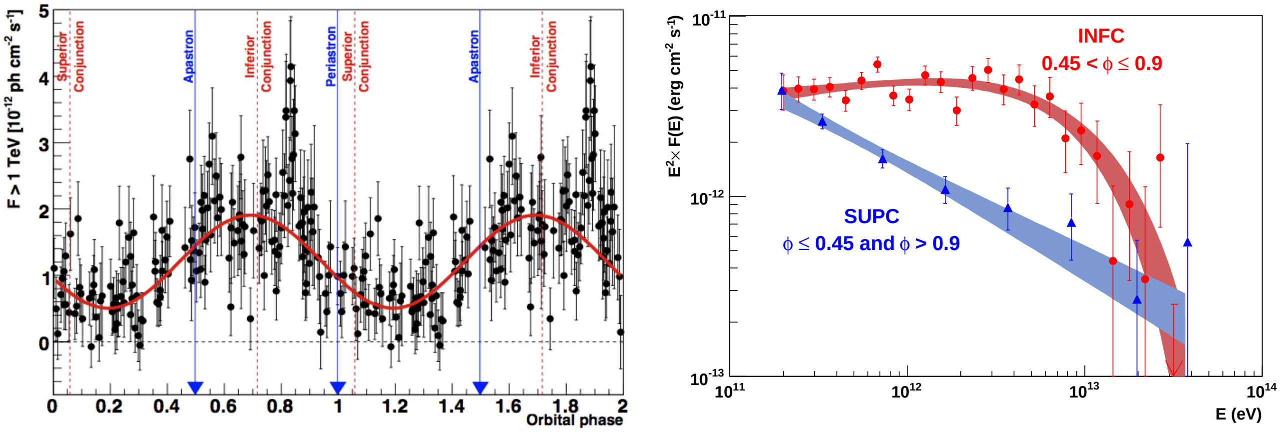

Figure 6–7: Left panel: LS 5039 integral gamma-ray flux (E > 1 TeV) light curve as a function of orbital phase as observed by H.E.S.S.. Right panel: VHE gamma-ray spectra obtained by H.E.S.S. for two broad orbital phase intervals: inferior conjunction and superior conjunction. Figures taken from [13].

conjunction, the spectrum is consistent with a steep ($\Gamma_{VHE} = 2.53 \pm 0.07_{stat} \pm 0.1_{syst}$) pure power-law.

Fermi/LAT has also detected LS 5039 [1]. There is a 3.9 day periodicity in the *Fermi/LAT* HE data, consistent with the VHE regime. The maximum of the emission in the GeV band occurs at superior conjunction and the minimum around inferior conjunction, which is opposite to the VHE emission. In addition, the GeV spectrum shows a cutoff at ∼6.3 GeV, as shown in Figure 6–8.

The differences between HE and VHE observations are puzzling. While the maximum emission phase difference could be explained by the competition between ICS on HE electrons and VHE pair production, the cutoff in the HE data suggests different radiative processes to explain the HE and VHE observations, which disagrees with the previous explanation. One possibility would be that the HE emission is a magnetospheric emission, similar to the pulsar emission seen by *Fermi/LAT* [1].

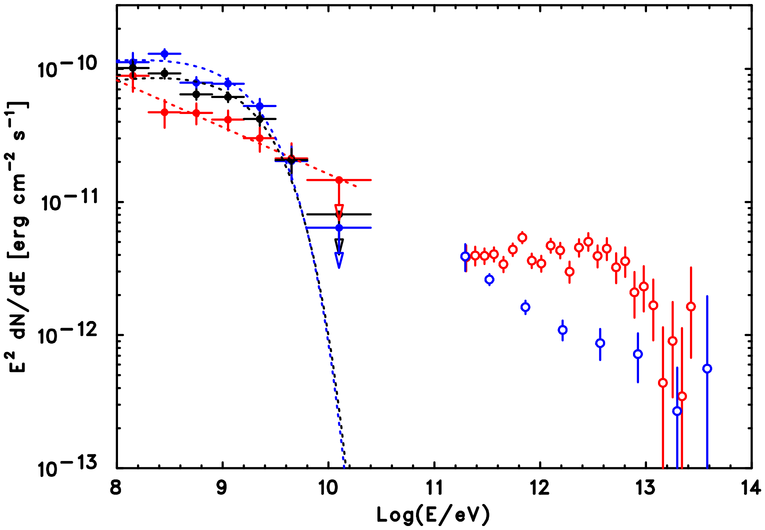

Figure 6–8: Fitted spectrum of LS 5039. *Fermi* data points are from likelihood fits in each energy bin. The black points (dotted line) represent the phase-averaged *Fermi*/LAT spectrum. The red data points (dotted line) represent the spectrum (overall fit) at inferior conjunction (Phase 0.45–0.9); blue data points (dotted line) represent the spectrum (overall fit) at superior conjunction (Phases, <0.45 and >0.9). Data points above 100 GeV are taken from H.E.S.S observations [13]; the data from H.E.S.S are not contemporaneous with *Fermi*, though they do cover multiple orbital periods. Figure taken from [1].

6.2.3 LS I +61 303

LS I +61 303 is a HMXB composed of a compact object, of unknown nature, and a massive Be star (B0 Ve). The system evolves on an eccentric orbit ($e = 0.72$) of period of 26.5 days and is located at a distance of 2.0 ± 0.2 kpc [57]. The nature of the compact object has been under debate for a long time. Radio observations suggest the presence of jet-like structure (see Figure 6–9, *e.g.* phase 0.3), which might imply a black hole. But it is also argued, from the same radio observations, that the emission could satisfy a pulsar scenario [38]. Recently, SGR-like behavior (showing bursting activity (see Chapter 5)) has been observed from the vicinity of the compact object in LS I +61 303 [46], suggesting the presence of a neutron star. However, it has not been confirmed that the burst was associated with the binary system.

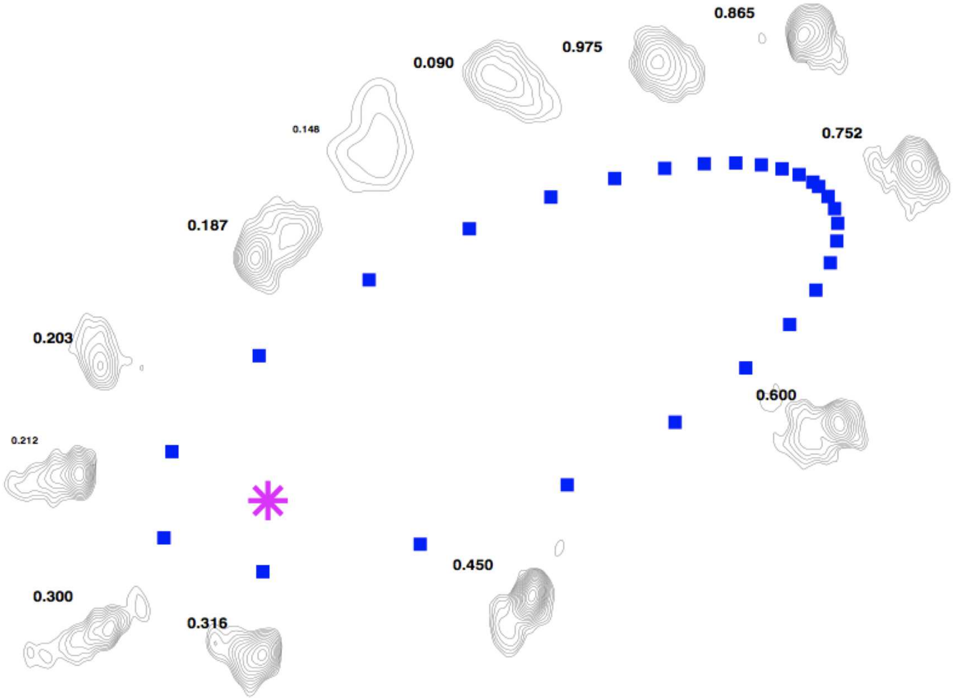

Figure 6–9: VLBA 8.3 GHz observations of LS I +61 303 showing extended radio emission. The star indicates the position of the stellar companion and the squares the positions of the pulsar 1 day apart. The time progression is counter-clockwise. Figure taken from [38].

LS I +61 303 was discovered as a VHE emitter by MAGIC in 2006 [16] and confirmed by VERITAS in 2008 [4]. MAGIC observations show a periodicity of 26.5 days. The emission occurs only at apastron (no emission was observed at periastron), as shown in Figure 6–10. The integrated flux measured by VERITAS at energies above 300 GeV is $(8.13 \pm 1.02) \times 10^{-12}$ cm^{-2}s^{-1} [4], which is consistent with the MAGIC results. More recent observations of the system by VERITAS show no emission at either apastron or periastron, which clearly indicates orbit to orbit variability [80].

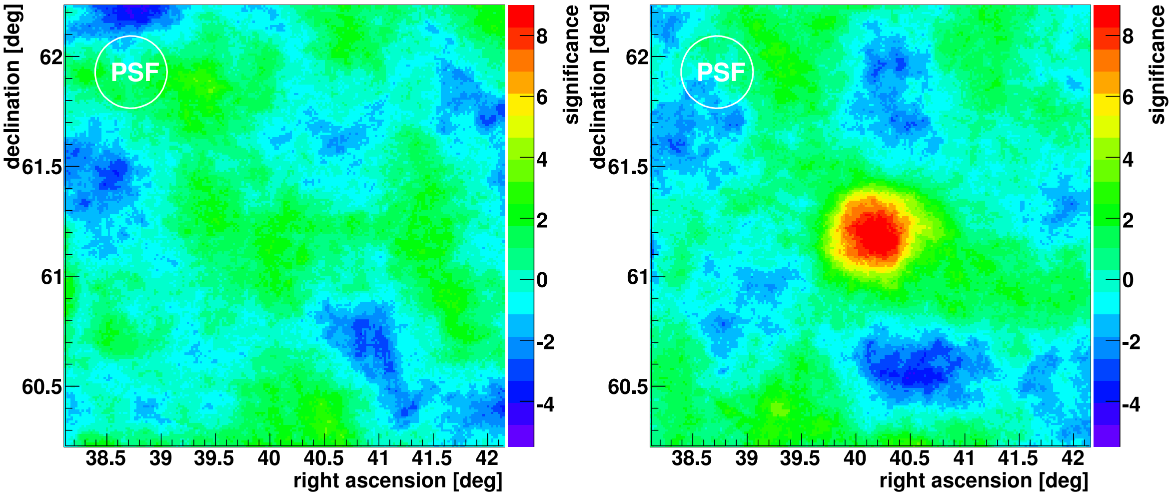

Figure 6–10: VERITAS significance maps in equatorial J2000 coordinates for the binary system LS I +61 303 for periastron (phases 0.8 to 0.5)(left panel) and apastron (phases 0.5 to 0.8)(right panel) in 2008. Figures taken from [4].

Observations in the GeV regime have been performed by *Fermi/LAT* [2]. In this energy band, the system is detected at all orbital phases; the maximum of the emission occurs at apastron and the minimum at periastron (see Figure 6–11), which is again the opposite of what is seen in the TeV energy band. The spectrum observed by *Fermi* shows a cutoff around 6 GeV (which is very similar to the case of LS 5039, see Section 6.2.2), as shown in Figure 6–11. This also suggests different radiative mechanisms to produce the HE and the VHE emission. As mentioned before, a cutoff in the energy spectrum is also seen in spectra from gamma-ray pulsars, suggesting that the HE emission could come from the pulsar itself.

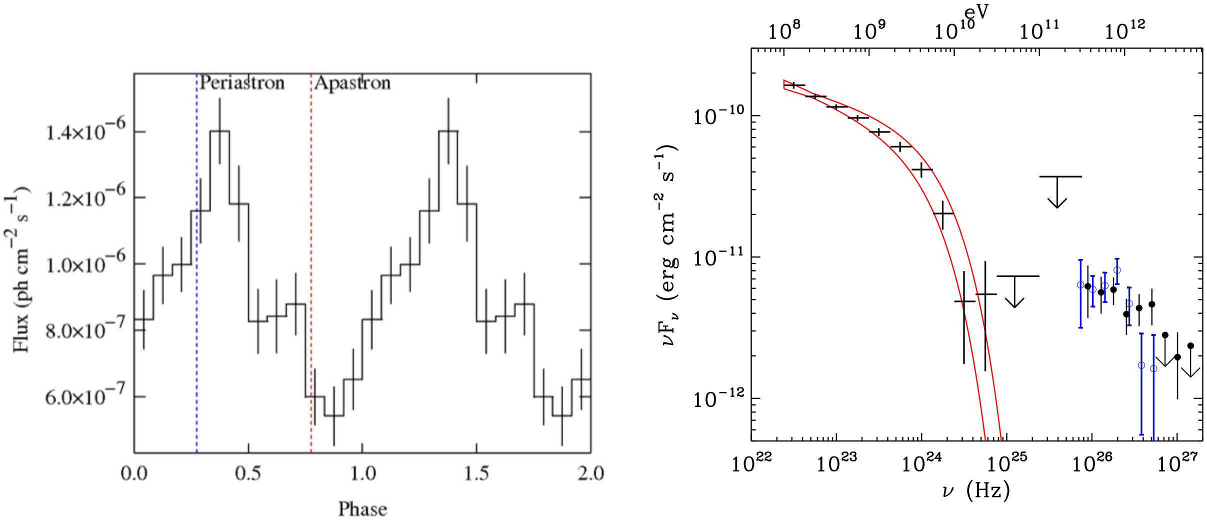

Figure 6–11: Left panel: Folded *Fermi*/LAT light curve of LS I +61 303 binned in orbital phase. The dashed lines indicate periastron and apastron. Right panel: Fitted spectrum of LS I +61 303 of the phase-averaged *Fermi*/LAT data below 10 GeV. The blue (open circle) data points are from MAGIC (high-state phases 0.5–0.7) and the black (filled circle) data points are from VERITAS (high-state phases 0.5–0.8). Figures taken from [2].

6.3 Radiative processes for TeV emission in X-ray binaries

To explain the VHE emission from the three systems presented above, two main models have been proposed; the binary pulsar model and the microquasar model. The key difference in these models is the nature of the compact object. While in the binary pulsar scenario the compact object is a neutron star, the microquasar scenario involves a black hole. Only one of the TeV binaries (PSR B1259-63) can be identified with a particular model. In the case of the two others, LS 5039 and LS I +61 303, the compact object nature has not been confirmed and so either could be applied. The two models, as well as how they apply to the different TeV binary systems, are described in detail below.

6.3.1 The binary pulsar model

The binary pulsar model has been proposed for systems composed of a massive star with a pulsar as the compact object. The system PSRB1259-63 has been identified as such, although the cases of LS I +61 303 and LS 5039 are still under debate. In this model, the emission is powered by the rotational spindown of the young pulsar. Indeed, the emission is produced at the interaction between the pulsar wind and the stellar wind. Particles are accelerated at the shock produced by the winds [44].

Be stars rotate rapidly, producing highly asymmetric outflow. This is the stellar wind. A young pulsar with a spindown power of around 10^{36}erg/s generates a strong relativistic wind. This is the pulsar wind. The pulsar wind is radial, isotropic and composed mainly of either $e^{\pm}$ (leptonic model) or protons (hadronic model). Most of the spindown power is transferred to the particles with a small fraction going to the magnetic field. The pulsar wind is contained by the stellar wind, as shown in Figure 6–12. A collisionless shock forms, beyond which the leptons or hadrons are accelerated. The shock has a “bow” or “comet” shape with a tail extending away from the stellar companion, as shown in Figure 6–12 and in the right panel of Figure 6–13.

In the leptonic model, the VHE gamma rays are produced by ICS of the stellar photons by VHE electrons accelerated at the shock [45]. The X-ray and radio emission are produced by synchrotron radiation of those same electrons. Since ICS depends on the incident angle between the photons, there is an orbital phase dependence in the IC spectrum as seen by the observer. Note as well that absorption by

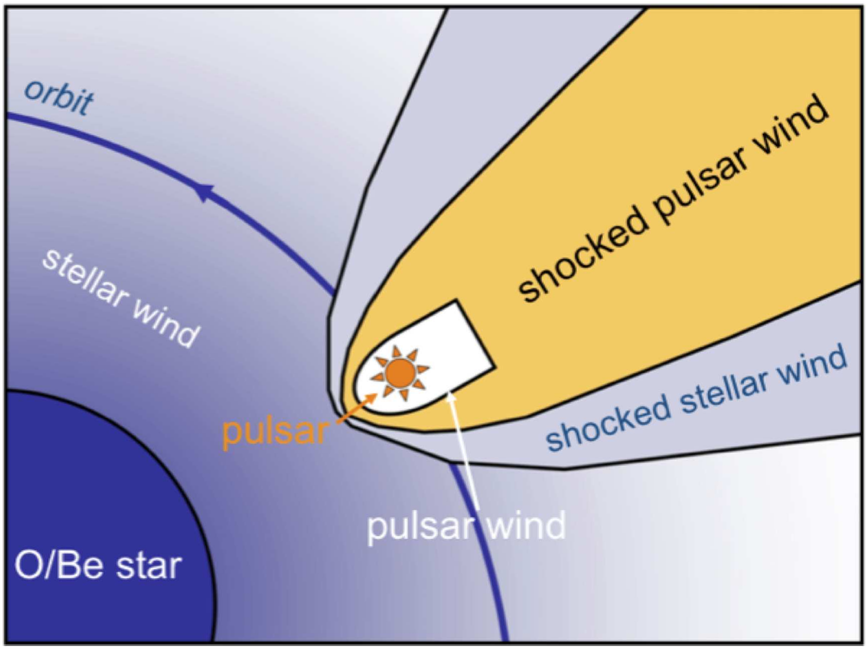

Figure 6–12: Illustration of a rotation-powered gamma-ray binary. Figure taken from [45].

the stellar UV photons plays a role in the phase-dependent emission. In the hadronic model, protons are accelerated in the same way as described for the electrons. The accelerated protons interact with the protons from the stellar wind and produce neutral pions that will produce TeV gamma rays [135]. The right panel of Figure 6–13 illustrates the binary pulsar model.

6.3.2 The microquasar model

The microquasar model has been proposed for systems composed of a massive star and a black hole as the compact object. In this model, the emission is accretion powered. It is important to mention that contrary to the binary pulsar model, the

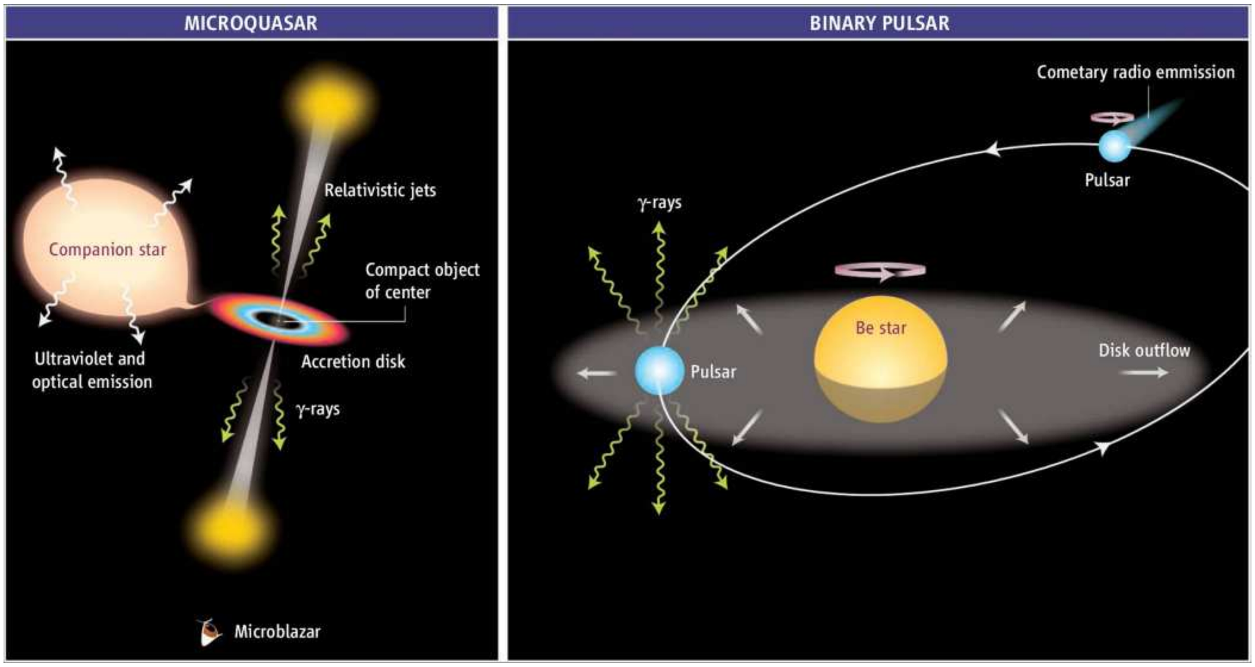

Figure 6–13: Illustration of the binary pulsar model (right) and the microquasar model (left). Figure taken from [129].

microquasar model has not yet been confirmed by observations. Indeed, since the systems LS 5039 and LS I +61 303 have not been confirmed as microquasars (nor binary pulsars), the microquasar model stays theoretical for now.

The accretion onto the black hole results in the production of two opposing relativistic jets. In the leptonic model, electrons and positrons are accelerated in the jets. In the case of the hadronic model, protons are accelerated. Figure 6–13 (left panel) shows a schematic of the microquasar. More details are given on this in Chapter 7.

In the case of the leptonic model, gamma rays can be produced by ICS of the stellar photons from the massive star by the relativistic leptons from the jet [149].

In the case of the hadronic model, the jet-accelerated protons will interact with the protons from the stellar wind and produce neutral pions. The neutral pions will decay into VHE gamma rays [149].

6.4 VERITAS observations of X-ray binaries

VHE emission from X-ray binaries is not well understood and more observations are necessary. Apart from the three known systems, only a few others have been identified as potential candidates, *e.g.* Cyg X-1, Cyg X-3, GRS 1915+105 and SS 433. Based on previous deep observations by Cherenkov telescopes, it is clear that these systems may need very long exposures in order to unveil the potential TeV emission. Also, in order to help understand the mechanisms responsible for the VHE emission, data on different types of X-ray binaries should be collected. The VERITAS experiment has dedicated time to only a few binary systems, with LS I +61 303 being the most observed system. The VERITAS results on this object showed that the apastron VHE emission was not present every orbit [80].

The 15 X-ray binaries (10 HMXBs and 5 LMXBs) presented here were studied using archival VERITAS observations dedicated to other targets, where the binaries happen to be in the same FOV. Below, each system will be described, as well as the observations. A summary of the binaries' characteristics and the VERITAS observations is presented in Tables 6–1 and 6–2.

Table 6–1: Characteristics of the X-ray binaries presented.

Object	System type[1]	Distance (kpc)	P_{orb} (d)	Ecc.[2]
LMXBs				
XTE J1901+014[109]	low mass star? + NS?	?	?	?
XTE J2012+381[169, 27]	faint red star + BH?	3 - 12	?	?
3A 1954+319[125]	M + NS(P = 5.09h)	1.7	< 400?	?
1A 0620-00 [73, 53]	K + BH	1.05±0.4	0.323	?
IGR J02291+5934[62, 165]	BD? + NS(P = 1.67 ms)	2 - 4	0.1	?
HMXBs				
EXO 2030+375 [154, 178, 179, 115]	Be + NS(P = 42s)	7.1	46.02	0.37 - 0.41
KS 1947+300[155, 114, 61]	Be + NS(P = 18.8s)	≈10	40.43	0.033
Cygnus X-1[182, 65]	O + BH	2.2±0.2	5.6	∼0
Cygnus X-3[167, 117]	WNe + BH?	9	0.2	∼0
IGR 00370+6122[36, 176, 26, 104]	B supergiant + NS	∼ 3	15.67	?
RX J0146.9+612[143, 76, 31, 151]	Be + NS(P ∼25min)	2.2	?	?
RX J0440.9+4431[144]	Be + NS(P = 202.5s)	3.3	?	?
SAX J0635.2+053[34, 110]	Be + NS(P = 33.8ms)	2.5 - 5	11.2	0.29
SAX J2239+6116[103, 102]	Be + NS(P =1247 s)	4.4	262	?
4U 1909+07[132]	OB + NS(P = 605 s)	∼ 7	4.4	?

6.5 VERITAS results on X-ray binaries

The analysis was done using EVNDISP-330 and EVNDISP-346, using the *Ring Background Model* and *standard cuts* (see Chapter 4 for more details). No gamma-ray emission has been detected from any of the binary systems analysed. The results are presented in Table 6–2, where the total significances and the flux upper limits are shown. An energy threshold of 400 GeV has been chosen to calculate the upper

---

[1] NS: Neutron Star, BH: Black Hole , BD: Brown Dwarf, WR: Wolf-Rayet, P: Neutron Star Period, ?: unmeasured quatity

[2] Ecc. = Eccentricity.

limits because some of the data was taken under moderate moonlight, raising the energy threshold slightly. To compare the results a uniform threshold of 400 GeV has been implemented.

In the next section, the implications of these results will be discussed. The characteristics of the three known TeV emitting binary systems will be compared to the systems presented here.

Table 6–2: Characteristics and results of VERITAS observations on X-ray binaries. The upper limits (U.L.) are for 99% confidence level for energies above 400 GeV. The offset is the distance between the object and the center of the FOV and S is the significance.

Object	Dates yy(mm)	Exposure (h)	Offset (°)	S (σ)	U.L. (cm^{-2} s^{-1}) [Crab Units]
LMXBs					
XTE J1901+014	08(05-06-10)	3.5	0.9 - 1.2	-1.8	1.08×10^{-12} [1.29%]
XTE J2012+381	07(09-10-11)/08(09-10-11)	14.0	0.5 - 1.4	0.6	2.56×10^{-12} [3.05]
3A 1954+319	07(05-06)/08(10)	12.4	0.2 -1.5	-0.6	1.01×10^{-12} [1.20%]
1A 0620-00	08(02)	4.2	0.5	0.5	1.92×10^{-12} [2.29%]
IGR J02291+5934	08(10-11-12)	12.6	0.5 - 1.2	0.8	1.87×10^{-12} [2.23%]
HMXBs					
EXO 2030+375	07(10)/08(06-09-10)	6.7	0.3 - 1.4	-1.3	2.34×10^{-12} [2.78%]
KS 1947+300	07(04-06)	4.3	0.9 - 1.4	-0.1	3.00×10^{-12} [3.57%]
Cygnus X-1	07(06)	9.8	0.5 - 1.4	-1.0	1.11×10^{-12} [1.32%]
Cygnus X-3	07(06)/08(06-09-11)/09(10)	20.0	0.3 - 1.0	2.1	1.62×10^{-12} [1.92%]
IGR 00370+6122	08(09-11-12)	4.7	1.0	-0.4	1.75×10^{-12} [2.08%]
RX J0146.9+612	08(10)	9.3	0.1 - 0.9	-1.1	1.40×10^{-12} [1.66%]
RX J0440.9+4431	08(10)	1.8	1.0 - 1.2	1.7	4.82×10^{-12} [5.73%]
SAX J0635.2+0533	08(12)/09(01-10)	18.0	0.2 - 1.2	1.4	7.27×10^{-13} [0.86%]
SAX J2239+6116	08(09-10-12)/09(09-10)	12.0	0.5 - 0.8	-0.8	7.90×10^{-13} [0.94%]
4U 1909+07	08(05-06)/09(09)	6.4	0.9 - 1.3	0.2	1.69×10^{-12} [2.01%]

6.6 Discussion

No TeV gamma-ray emission has been detected from any binary systems presented here. Note that some of the upper limits on the flux do not reach the observed flux levels from the three known TeV emitters (see Table 6–3). Longer observations would be needed to reach such flux limits or to observe fluxes at that level.

Table 6–3: Summary of the results from TeV gamma-ray observations of the three known TeV binary systems.

Object	Exposure (h)	Significance (σ)	Integrated fluxes ($\mathrm{cm}^{-2}\ \mathrm{s}^{-1}$) [% of Crab Units]
PSR B1259-63	49.8	13.8	$(4.0 \pm 0.4) \times 10^{-12}$ [4.4][1]
LS 5039	69.2	> 40	Inf. Conj. : $(2.28 \pm 0.1) \times 10^{-12}$ [0.97][2] Sup. Conj. : $(0.91 \pm 0.1) \times 10^{-12}$ [0.39][2]
LS I +61 303 (apastron)	45.9	8.4	$(8.13 \pm 1.02) \times 10^{-12}$ [6.32][3]

If we recall from Section 6.2, despite the lack of obvious correlation between the different system characteristics, there are some similarities between the binaries that are TeV emitters. Indeed, all of them contain a massive stellar companion (type O or Be), they all have strong stellar winds, their orbits are eccentric and the compact object passes within a few astronomical units of its companion star. Finally, the

---

[1] For energies above 380 GeV.

[2] For energies above 200 GeV.

[3] For energies above 300 GeV.

systems are all radio emitters. Note that of the 114 HMXBs, only 9 are detected at radio wavelengths [118].

Of the 15 systems observed by VERITAS and presented in Section 6.5, none satisfies all the criteria mentioned above. All, except Cyg X-3, have massive O or Be stars. Most of the systems do not have eccentric orbits. Only Cyg X-1 and Cyg X-3 show radio emission. Since there are no systems fullfilling all the criteria mentioned above, only weak conclusions on the required criteria to emit at the TeV energies can be reached. However, some of the systems presented here have been subjects of theoretical investigations, which predict, in some circumstances, VHE emissison. These systems are discussed below.

Cyg X-1

Cyg X-1 satifies most of the TeV emission criteria. The only characteristic that differs is the circular orbit. This system has been observed extensively by MAGIC. Recently, that collaboration reported evidence of VHE emission from Cyg X-1 coincident with an X-ray flare [17]. The signal was at a significance of 4.1 σ post-trials, below the generally accepted threshold of 5 σ to claim a detection. Thus, the MAGIC result requires confirmation. MAGIC did not observe steady VHE emission from Cyg X-1. With 40 hours of data on the source, their upper limits on the integral flux were from 1% to 2% of the Crab Nebula flux. A possible signal was observed only during an X-ray flare. Figure 6–14 shows the measured fluxes from Cyg X-1. The flare in X-rays, seen by *Swift* and *RXTE*, is coincident with the possible signal in VHE gamma rays. Note that, except for the point representing the flare, the MAGIC points are all consistent with no emission.

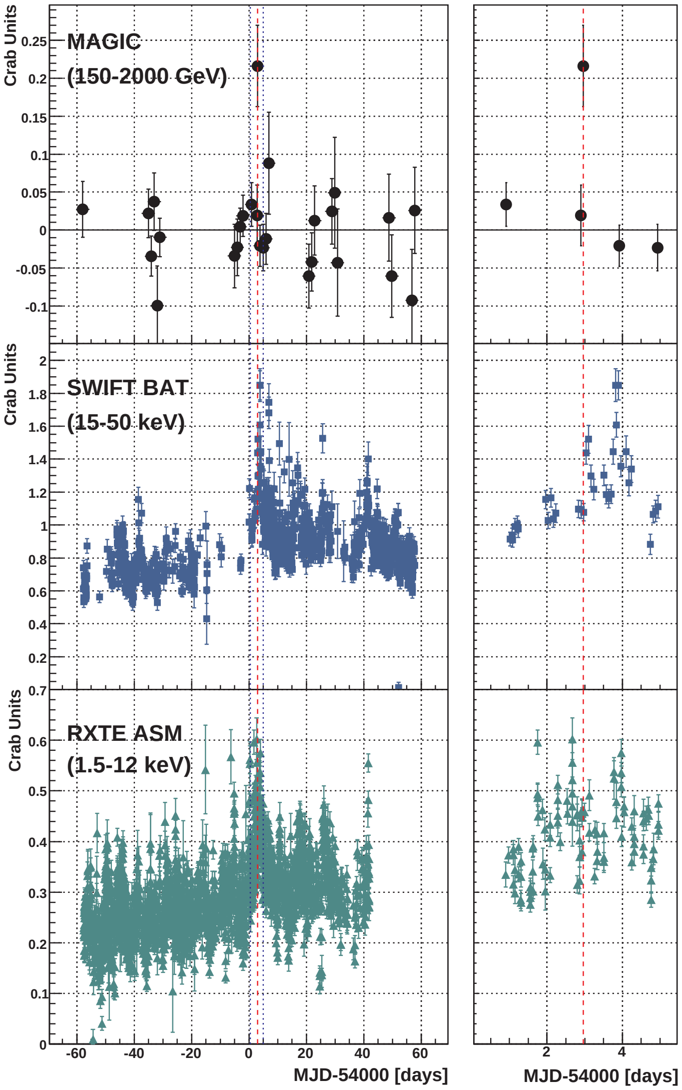

Figure 6–14: MAGIC, *Swift/BAT* and *RXTE/ASM* measured fluxes from Cyg X-1 as a function of time. Figure taken from [17].

In the case of the VERITAS Cyg X-1 observations, no data were taken at the time of an X-ray flare (see Figure 6–15). The last data set was taken the night after a high X-ray count rate, although the intensity was not as high as major flares from

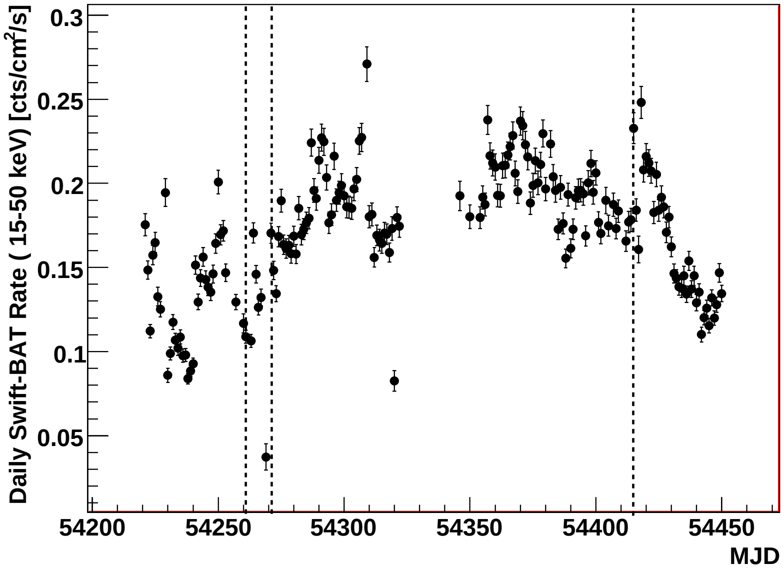

Figure 6–15: *Swift* daily light curve for Cygnus X-1 for the energy band 15-50 keV. The dotted lines show the period intervals of VERITAS observations. Note that the last period was only one day long.

this source [where the *Swift/BAT* count rate can reach 0.4 counts/cm^2/s]. The upper limit on the integrated flux derived from this analysis (1.3% of the Crab Nebula flux above 400 GeV) is comparable with the MAGIC upper limit for the quiescent phase.

Cyg X-3

Cyg X-3 has been studied in gamma-rays for almost 30 years. In the 1980s, TeV detections of Cyg X-3 were claimed, but in the 1990s, the more sensitive new generation of ground-based telescopes did not confirm these detections. Recently, Cyg X-3 has been detected in the HE gamma-ray band by the *Fermi/LAT* instrument [3] and the AGILE satellite [157]. The detection, however, is modulated; the HE emission

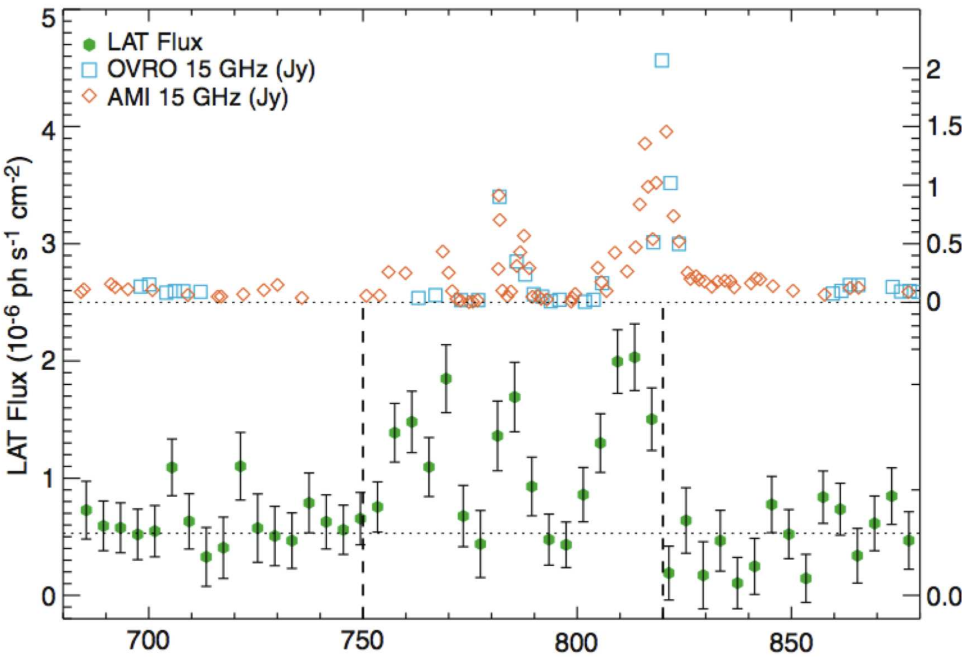

Figure 6–16: Gamma-ray and radio light curves of Cyg X-3 from the *Fermi*/LAT and from radio telescopes *OVRO* and *AMI* as a function of time. The quantity on the horizontal axis is MJD − 54000. The two dashed lines illustrate the active period. Figure taken from [3].

occurs only at superior conjunction. The HE emission occurs close to high-intensity radio emission, see Figure 6–16. The HE emission corresponds to the minimium intensity in the 15-50 keV X-ray band and to the maximum in the 1.5-12 keV band, indicating correlation with the soft X-ray state. The flux during the HE emission phase corresponds to $1.19 \pm 0.06_{stat} \pm 0.37_{syst} \times 10^{-6}$ photons $cm^{-2}s^{-1}$ above 100 MeV and the spectral index Γ is $2.70 \pm 0.05_{stat} \pm 0.20_{syst}$ [3].

From the VERITAS observations, 2.33 h of data were taken during the HE emission state of Cyg X-3. Data were taken on MJD 54786, 54789, 54804. From Figure 6–16, these dates are close to HE emission points. An analysis of this subset of data gives a significance of 1.0 σ at the nominal source position. This gives an upper limit on the VHE flux of 4.01 $\times 10^{-12}$ photons cm^{-2}s^{-1} above 400 GeV. The extrapolation of the *Fermi/LAT* flux, considering a power-law with the spectral index quoted by *Fermi*, gives 9 $\times 10^{-13}$ photons cm^{-2}s^{-1} above 400 GeV. Thus, VERITAS observations are not sufficient to probe the extrapolation from the *Fermi* results, assuming the emission would follow a power-law from 100 MeV to TeV energies.

KS 1947+300

KS 1947+300 has some characteristics that could suggest VHE emission. This system contains a highly magnetized neutron star (B = 2.5 $\times$ 10^{13} G). It has been proposed that systems composed of Be stars and highly magnetized neutron star should produce detectable TeV emission during major X-ray outbursts [137]. This particular model was developed for the case of A0535+26, which undergoes a major outburst every ∼5 years. Note that the outbursts observed for the KS 1967+300 system are not as intense as the ones seen in A0535+26. The VERITAS observations on KS 1947+300 were not performed during a period of intense X-ray activity[1] .

For the other HMXBs, some of the systems have not been studied enough to identify their orbital parameters. It is therefore difficult to include these systems in

---

[1] VERITAS dedicated intense coverage to A0535+26 during the last major X-ray outburst (December 2009), and no TeV emission was detected. These results, that will be presented in a paper in preparation at the time that this document is written, do not seem to confirm the model.

the general discussion of TeV emitting binaries. Other systems only possess a few of the common characteristics of the TeV binaries, making them also difficult to include in the general discussion.

For the case of the LMXBs, since no such systems have been detected in the TeV regime, there is no direct comparison that can be made. These systems are known to have transient behavior, but none of the VERITAS observations were performed during flaring activity.

CHAPTER 7
The SS 433 system

SS 433 is one of the most well-studied microquasars at present. The system is known for its powerful precessing jets, which fire energetic particles into the surrounding interstellar medium. In this chapter, a detailed description of the SS 433 system will be given. Between 2008 and 2010, VERITAS dedicated several hours of observation to this system. The observations and results will be presented here, as well as a discussion of the implications of these results.

7.1 Review of microquasars

A brief introduction to the subject of microquasars and a description of theoretical scenarios of VHE gamma-ray production by microquasars were given in Chapter 6. Before going into the details of the microquasar SS 433, a general review of the characteristics and of the emission processes of microquasars will be given.

Microquasars are part of a sub-class of X-ray binaries composed of a compact object (NS or BH) and a stellar companion. The characteristic that differentiates microquasars from other binary systems is the presence of relativistic radio jets. The accretion of material from the stellar companion towards the compact object (see Section 6.1 for details on accretion) is believed to be responsible for the jet production.

Emission from microquasars ranges from radio wavelengths to HE (potentially to VHE) gamma-ray wavelengths. At lower energies, the emission is dominated by thermal radiation. At higher energies, where temperatures required to produce high energy thermal radiation would be extremely high, the emission is attributed to non-thermal processes.

Thermal emission is detected from these systems in the optical and UV bands. In the case of HMXBs, the thermal emission is principally produced by the companion star, although some emission can also come from the stellar wind and from cold regions of the accretion disk. In the case of LMXBs, emission at these wavelengths is believed to be produced in the accretion disk by interaction of X-ray photons with the disk material resulting in lower energy photons. In this case, the emission from the stellar companion is small. There is also intense thermal X-ray emission produced in the accretion disk (temperature of the order of $10^8 K$).

The non-thermal emission, which is produced mainly in the jets, extends from the radio to the gamma-ray bands. Several processes play a role in the non-thermal emission. The origin of the radio emission is synchrotron radiation from accelerated leptons in the magnetic field. Note that the origin and evolution of the magnetic field, as well as particle acceleration mechanisms (see Section 6.3 for a description of acceleration mechanisms) are not well understood. At higher energies, inverse Compton scattering of photons (either from the companion star, the disk, the CMB or the jets themselves) by relativistic leptons could be responsible for the gamma-ray emission. High-energy protons, accelerated in the jets, could also produce HE emission by interacting with ambient material and producing π^0s. Furthermore, HE emission could also be produced by the interaction of the jets with the interstellar medium (ISM) (where the accelerated jet particles hit the target particles of he ISM) (see Section 7.3.2).

The preceding paragraph gave a brief description of how radiation is or could be produced in microquasar systems. The study of VHE emission (which has not yet been detected) may allow the study of detailed emission mechanisms.

7.2 The microquasar SS 433

SS 433 is a close binary system composed of a black hole and a massive stellar companion of type A. The system evolves on a 13.1-day circular orbit [54] and is located between 4.5 kpc [138] and 5.5 kpc [170][79] from Earth. From observations by *INTEGRAL* and optical observations, the mass of the black hole and of the massive star are estimated to be $M_{bh} \simeq 9M_{\odot}$ and $M_{\star} \simeq 30M_{\odot}$ [30].

The system displays two oppositely directed relativistic jets. The bulk speed in the jets is $0.26c$ [124]. The axis of the jets is precessing in a cone with a half opening angle of ∼20°, with a precession period of ∼163 days. The system is oriented at an angle of ∼79° with respect to our line of sight. Figure 7–1 shows a schematic view of the system. It has been shown that the jets contain a hadronic component [128] which is accelerated in the jets along with the leptonic component. Note that SS 433 is the only system where a hadronic component of the jets has been identified.

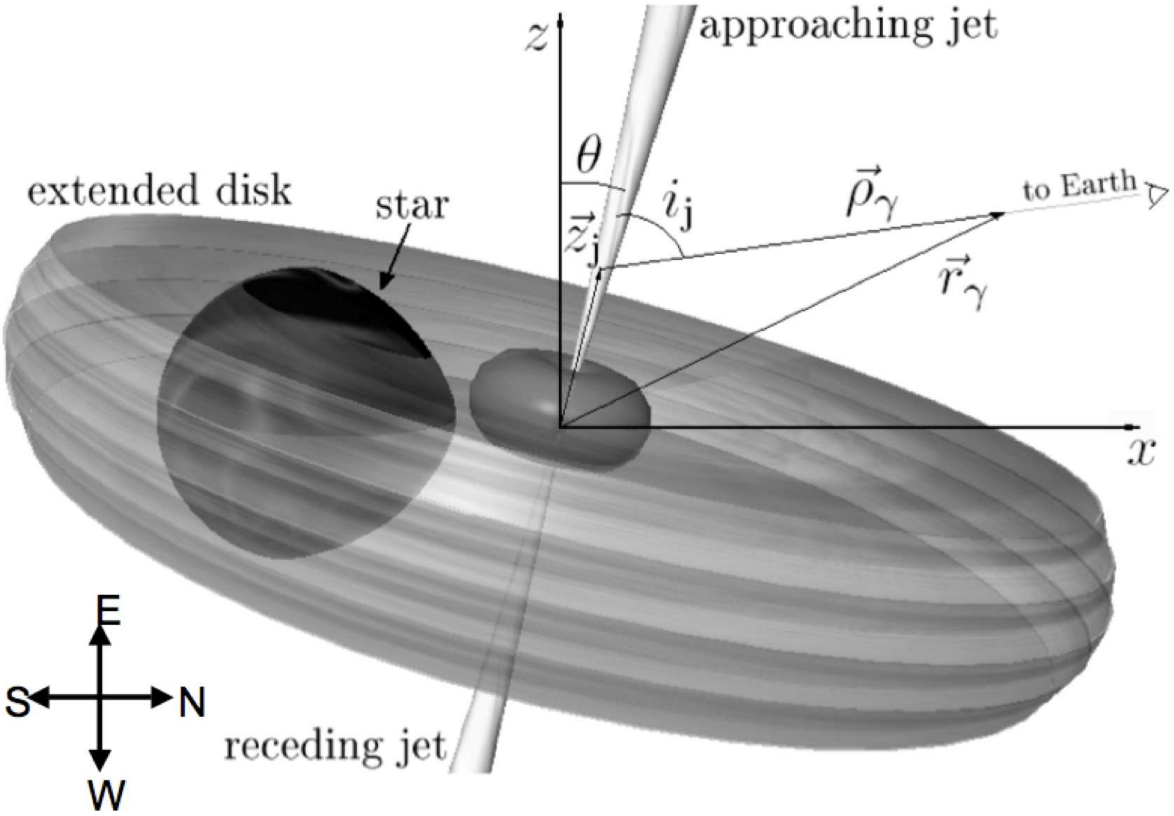

Figure 7–1: Schematic view of SS 433. This view has been rotated by 90° clockwise from the view in the sky. The approaching jet is the eastern one and the receding jet is the western one. Figure taken from [145].

The SS 433 system is located at the center of the large W50 supernova remnant. The W50 shell has been deformed by the jets, which have created opposite lobes, extending to the east and west directions of the jets. This is clearly visible in Figure 7–2, where the circular shell is seen to be deformed in the east and west.

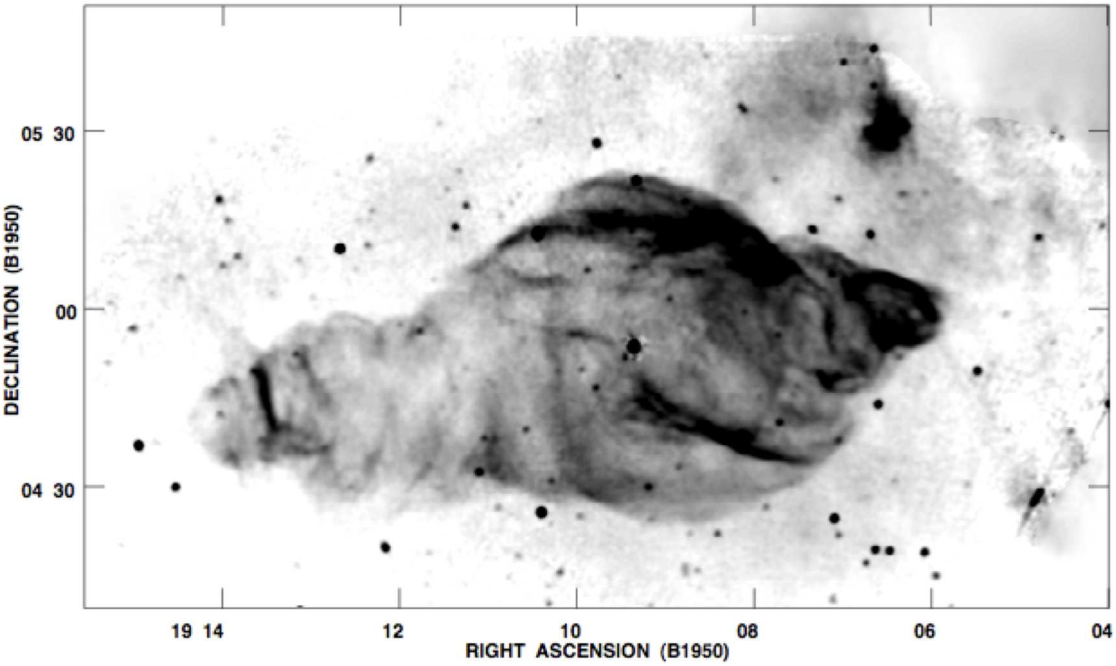

Figure 7–2: VLA radio continuum image of W50 at 1465 MHz. The bright point source at the center (RA: ∼19 09 Dec: ∼+04 53) is the black hole, the regions where the jets interact with the ISM are visible in the east (RA:∼19 13 Dec: ∼+04 40) and in the west (RA:∼19 07 Dec:∼+05 00). Figure taken from [43].

7.2.1 Radio emission from SS 433

SS 433 is the most powerful permanent radio-jet X-ray binary in the Galaxy. The central part of SS 433 radiates at the level of ∼1 Jy at cm wavelengths [54]. Practically all of the radio emission from SS 433 is non-thermal synchrotron radiation from the jets. The structure of the precessing jets has been well determined from VLA observations [79], see Figure 7–3.

Long term monitoring of SS 433 at radio wavelengths has shown strong variability in the emission flux and structure [153]. Flares have also been observed, during which the radio emission can be modified considerably, showing emission only in

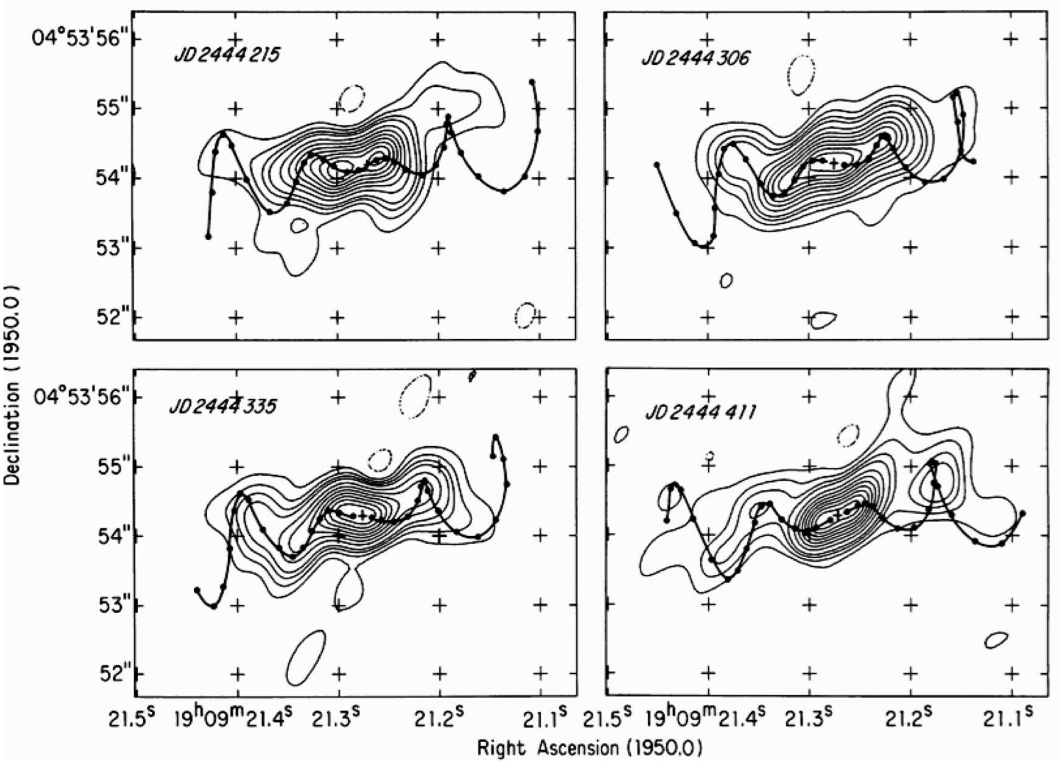

Figure 7–3: VLA radio contour maps of the SS 433 system at 4885 MHz for different dates. The proper motion paths of material ejected are shown by the heavy solid lines. Figure taken from [79].

one jet for example [170]. This asymmetry in the radio emission during flares suggests interactions between the jets and the surrounding material, absorbing the radio emission [54]. Radio observations presented in Figure 7–3 show clear helical structures (created by the jet precession) that have formed in the interaction with the surrounding material.

7.2.2 X-ray emission from SS 433

SS 433 has been studied at X-ray wavelengths since the 1980s [172]. X-rays have been detected from the vincinity of the black hole and from the regions where the jets interact with the surrounding medium (both eastern and western ends). The X-ray image from the western region of the jets is shown in Figure 7–4, where X-ray emission is coming from the region labeled $w2$ [150]. Deeper observations performed with *Chandra* (see Figure 7–5), show that the emission from $w2$ is non-thermal [131].

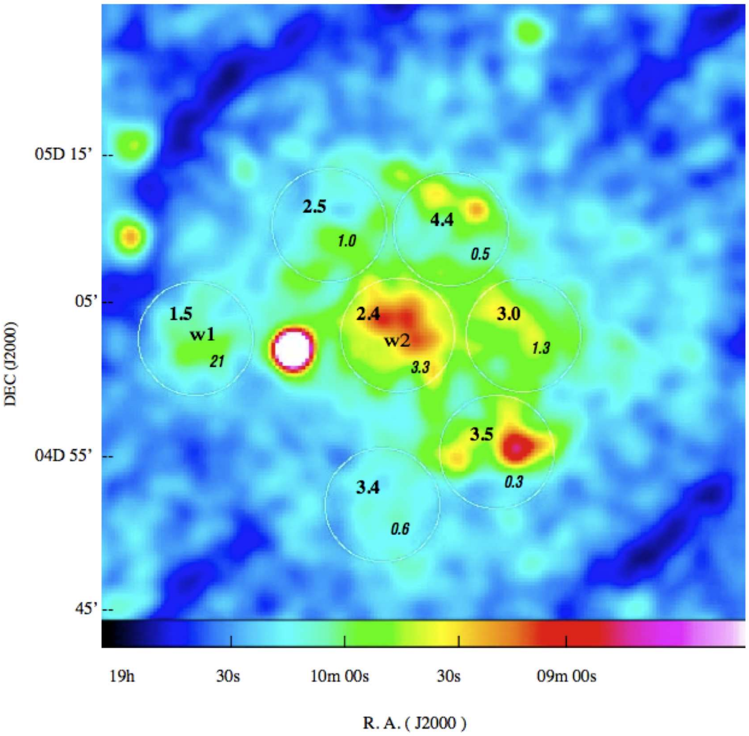

Figure 7–4: *ROSAT* PSPC brightness image of the western lobe of SS 433. Note that the bright pointlike source appearing at R.A.(J2000) = 19h10m13s and decl. (J2000) = 05°02'14" is a known X-ray source not related to the SS 433 system. Figure taken from [150].

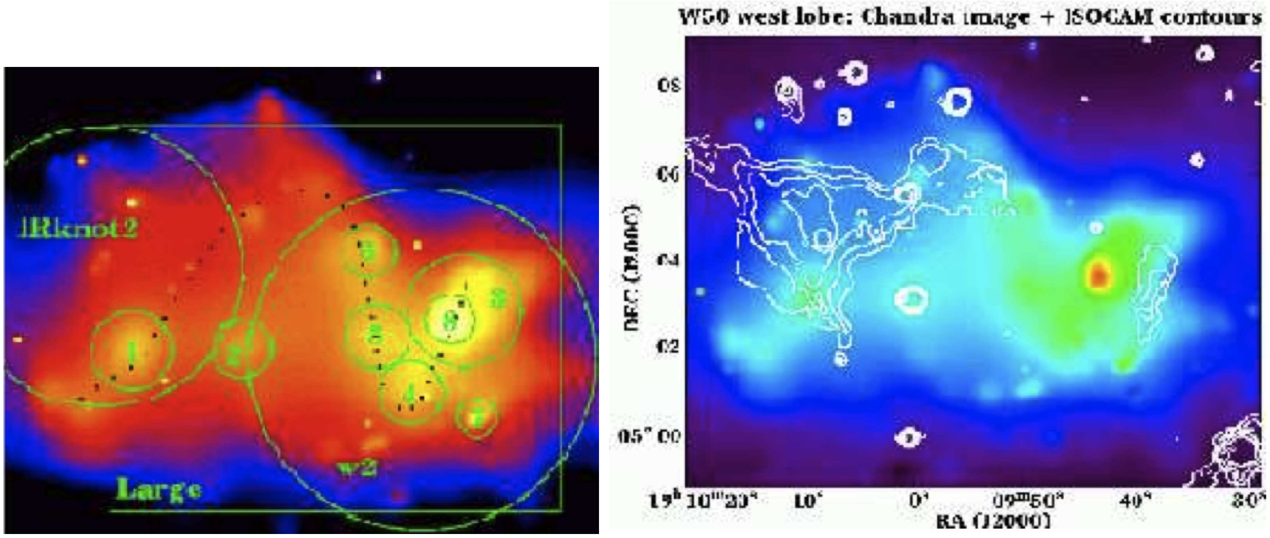

Figure 7–5: X-ray images of the western lobe of SS 433. Left: *Chandra* 0.3-10 keV image. $w2$ is indicated by the green circle. Right: *Chandra* image shown with infrared contours. The bright emission region at Ra: 19h09m45s Dec: +05°03' corresponds to the w2 region. Images taken from [131].

7.2.3 Millimeter emission around SS 433: CO emission

Observations in the millimeter wavelengths have shown that a molecular cloud is located at the edge of the western lobe of SS 433. Figure 7–6 presents the CO contour map, where the molecular cloud can be seen at the western edge of the system.

7.2.4 VHE observations of the SS 433 system

TeV gamma-ray observations of SS 433 have previously been performed by the HEGRA collaboration [12]. Over 100 h of data were acquired on the SS 433 system between 1998 and 2001. No gamma-ray emission was detected and upper limits at the 99% confidence level on the flux from different parts of the system were calculated:

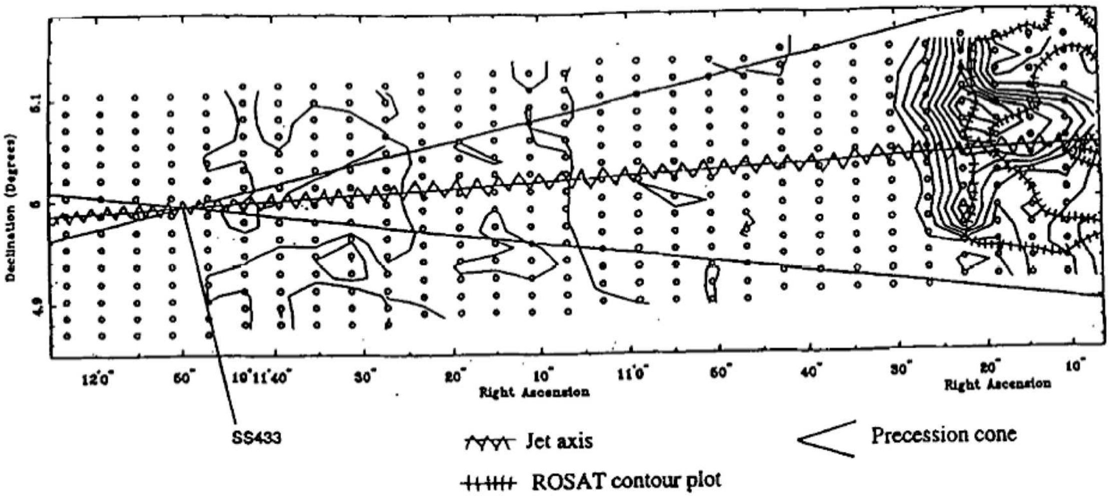

Figure 7–6: CO contour map around the SS 433 system. The solid line indicates the precession cone of the jet. The black hole is indicated by the SS 433 position. The zigzagged line shows the jet axis. The X-ray *ROSAT* data are shown by the railroad lines. The CO contours lines clearly show the presence of a molecular cloud at the end of the western jet. Figure taken from [50].

8.9 $\times 10^{-13}$ ph cm^{-2} s^{-1} above 800 GeV at the black hole position and 9.0 $\times 10^{-13}$ ph cm^{-2} s^{-1} above 700 GeV at the w2 position.

The CANGAROO-II experiment also observed the SS 433 system in 2001 and 2002. No gamma-ray emission was detected and an upper limit at the 99% confidence level on the flux from near the w2 position was calculated: 1.3 $\times 10^{-12}$ ph cm^{-2} s^{-1} above 850 GeV.

7.3 Predictions of gamma-ray emission from SS 433

In Chapter 6, a general model for VHE emission from microquasars was described (see Section 6.3.2). For the particular case of SS 433, two theoretical models have been developed in deeper details, giving predictions of the VHE emission.

7.3.1 Production of gamma-rays in the jets of SS 433

The first model (referred to here as the *Reynoso* model) describes gamma-ray production in the jets of SS 433, near (less than $\sim$1 pc away) the black hole [145]. In this model, protons are accelerated along the jets at shocks produced by collisions of plasma outflows with different bulk velocities. These protons are accelerated up to energies $E_p^{max} \approx 3.4 \times 10^6$ GeV. This efficient acceleration occurs only up to $\sim 10^{12}$ cm from the black hole. It is the collisions of the high-energy protons with lower-energy protons in the jets that cause the production of secondary gamma rays.

However, the VHE gamma rays produced in the jets are subjected to absorption [146]. Indeed, the gamma-ray absorption can occur via interactions with ambient photons or with the matter from the stellar disk. These interactions will cause pair production processes. Since the system is precessing, the disk moves in and out of the line of sight of the observer (see Figure 7–1). When the disk is not in the line of sight, gamma rays produced near the black hole can escape without having to travel through the disk.

The moments where the disk is out of the line of sight occur at precessional phases $\psi \lesssim 0.09$ and $\psi \gtrsim 0.91$ (see Figure 7–7). During these phases, gamma-ray emission is favored. Figure 7–7 shows the gamma-ray flux predictions from the model for different energy bands.

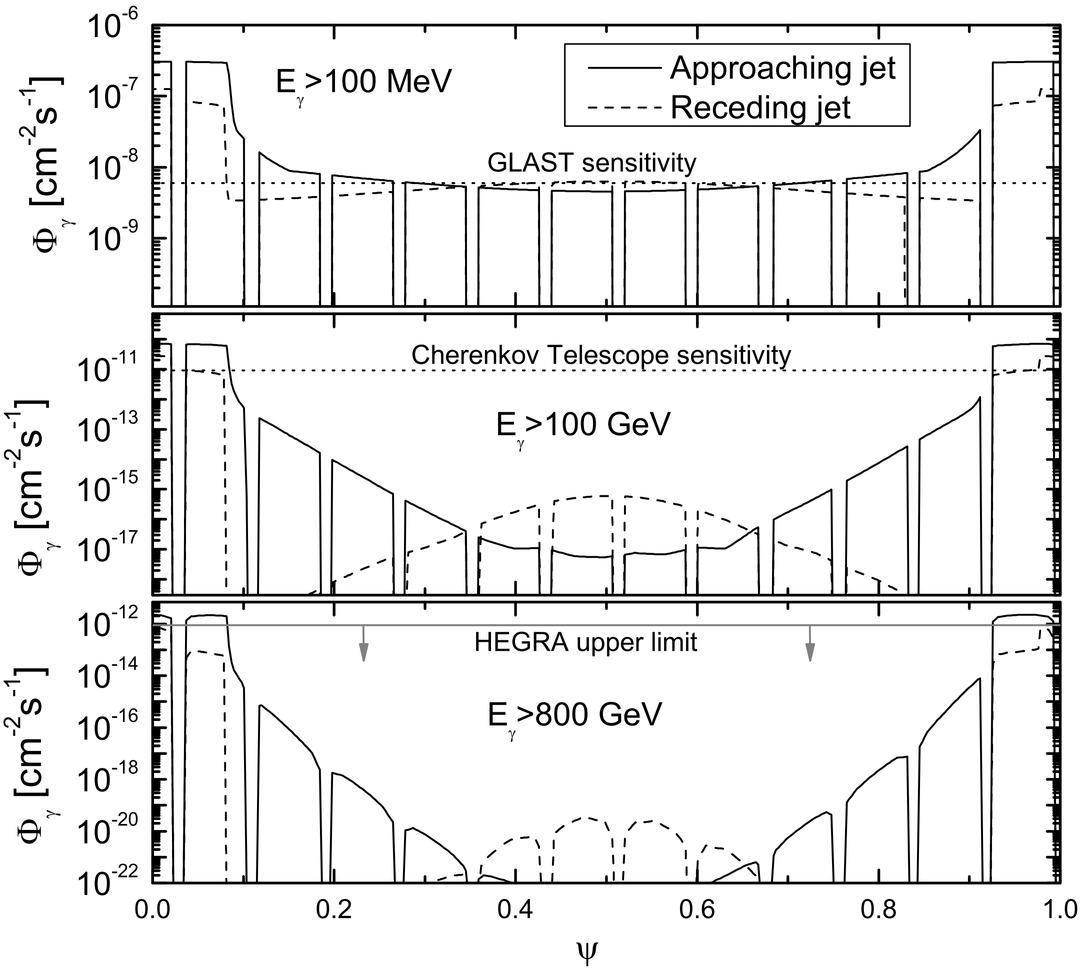

Figure 7–7: Predictions of the gamma-ray fluxes arriving at Earth from SS 433 as a function of precessional phase, from the *Reynoso* model. The contributions of the two jets are shown: solid line for the east jet and dashed line for the west jet. Figure taken from [145].

7.3.2 Production of gamma rays in the microquasar/ISM interaction

The second model (referred to here as the *Bordas* model) proposes gamma-ray production where the jet interacts with the interstellar medium (ISM) [23]. In this model, acceleration of electrons is considered and three regions of emission are studied: the shell, the cocoon and the reconfinement region (see Figure 7–8). The shell region corresponds to the ISM swept up by the primary forward shock (called *bow shock* on the figure). The cocoon region is the region where the material of the jet crosses the reverse shock (the reverse shock is created when the primary shock hits the ISM). The reconfinement region is between the reconfinement shock (formed in the jet where the jet pressure equals that of the cocoon) and the point where the accelerated material from the jet reaches the material from the cocoon.

In this model, the particles (electrons) are accelerated by the shocks along the jets (in the same way as in the previous model). In the shell region, the acceleration brings the electrons to a maximum energy ranging between 2 and 10 TeV. The synchrotron emission dominates and the inverse Compton scattering (ICS) emission is well below. In the cocoon region, the electrons can be accelerated up to ∼100 TeV. The synchrotron emission still dominates over the ICS emission. Finally, in the reconfinement region, electrons are accelerated up to ∼10 TeV, and in this case, synchrotron emission is at the same level as the ICS emission.

The model predicts gamma-ray emission for energies above 100 GeV to be of the order of $\sim 10^{-15}$erg s^{-1} cm^{-2}, which is below the sensitivity of current Cherenkov telescopes. However, the author points out that for different values of some parameters assumed in the model (*e.g.* the age of the microquasar (τ_{MQ}), the distance (d), the density of the ISM medium (n_{ISM}), the jet kinetic power (Q_{jet}) and the non-thermal luminosity fraction (χ)), the emission flux could be much higher and reach detectable fluxes. Indeed, the values used in the model are rather conservative. In

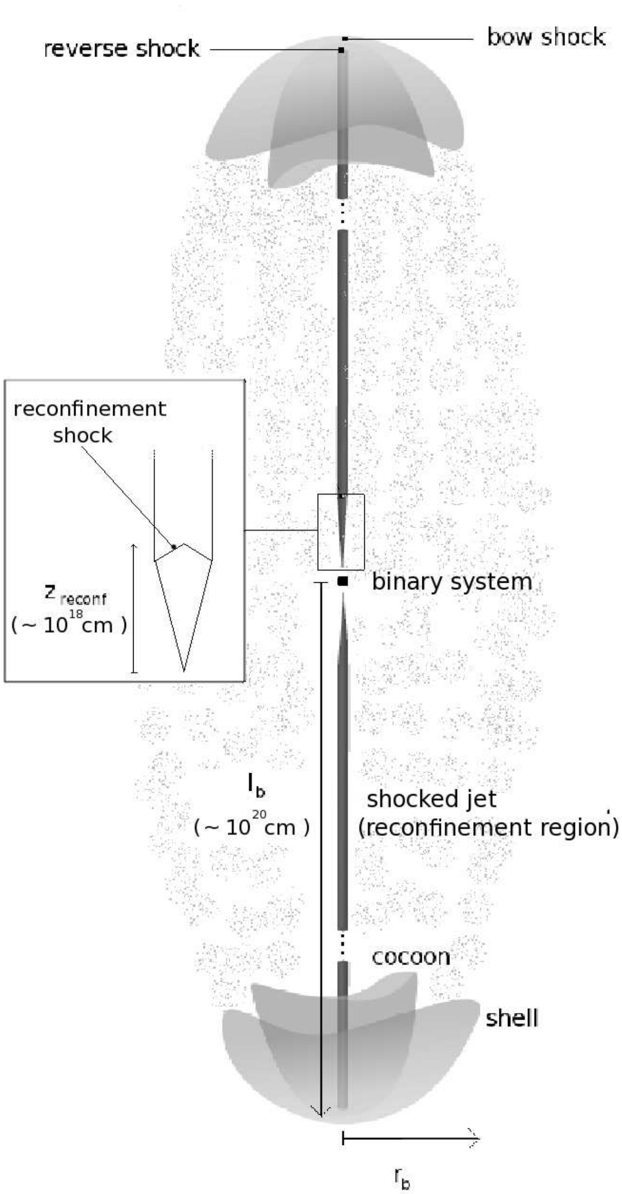

Figure 7–8: Schematic drawing of the *Bordas* model (not to scale) representing the three different zones discussed in the text. Figure taken from [23]

the discussion section (Section 7.6), these parameters will be reviewed and discussed. An example of the predicted spectral energy distribution (SED) for a particular set of parameters is given in Figure 7–9.

In addition, the model has considered acceleration of electrons only, although it has been shown that the jets have a hadronic content as well (see Section 7.2). Acceleration of protons is briefly discussed in the model. It is suggested that for some sensible values of the parameters mentioned above, moderate levels of hadronic emission from the jet termination regions may be detected if the jets are powerful enough.

7.4 VERITAS observations of SS 433

Data from SS 433 were retrieved from VERITAS archival data, as was done for the X-ray binaries presented in the previous chapter. A total of 10.4 h, taken in Fall 2007 and Spring 2008, were selected for the analysis. The *standard* analysis (see Section 4.3) was used. At the position of the black hole, no gamma-ray emission was detected. However, at the position of w2, an excess of 4.7 σ (pre-trials) was found. Figure 7–10 shows the skymap of the first analysis. A secondary analysis, using a different analysis package confirmed the excess. The excess does not reach the level of 5 σ, conventionally taken as the minimum required to claim a new discovery, but because it lies at the position of w2, where VHE gamma-ray emission could be produced, the excess is considered as a tantalizing hint of a signal.

For the 2009-2010 VERITAS observing season, observations were allocated at the w2 position of SS 433. Note that this source is only visible for VERITAS in September, October, the end of April, May and the beginning of June. In order to

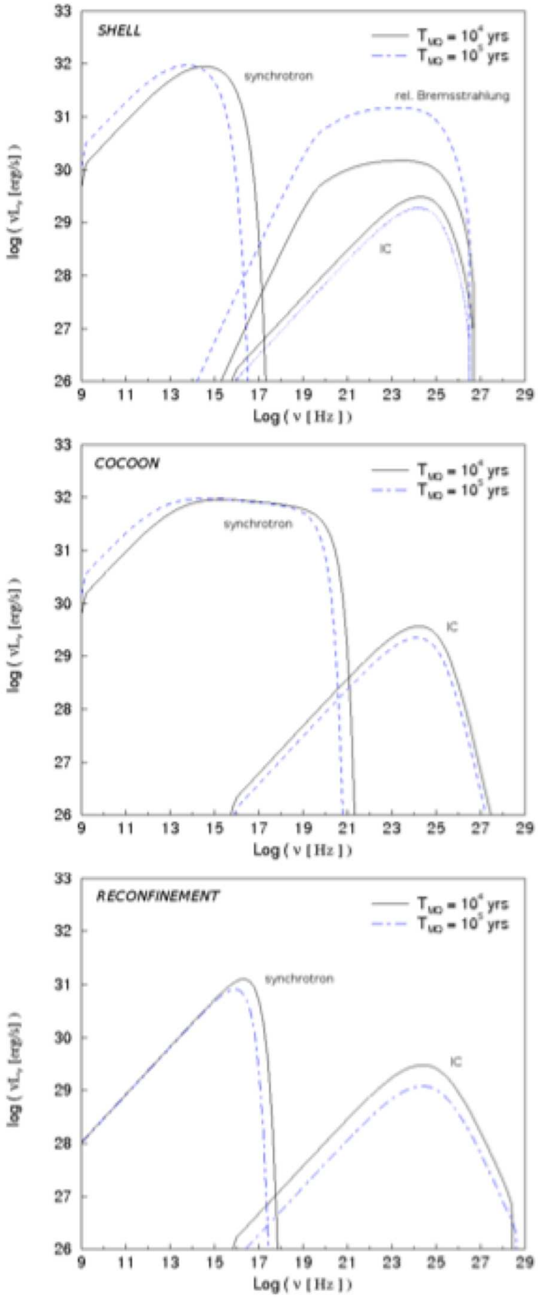

Figure 7–9: SED obtained using $Q_{jet} = 10^{37}$ ergs^{-1} and $n_{ISM} = 1$ cm^{-3} in the *Bordas* model. Figure taken from [23].

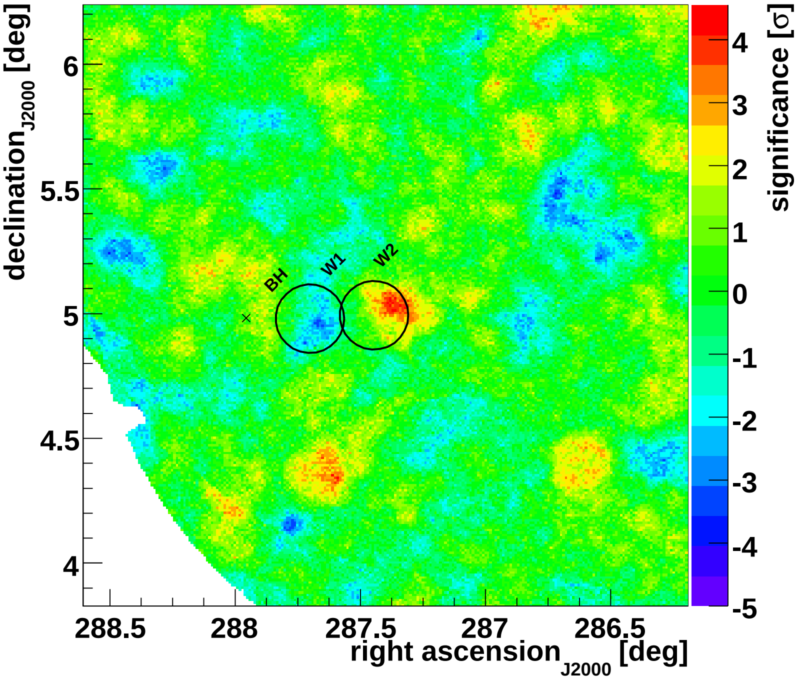

Figure 7–10: VERITAS significance skymap in J2000 equatorial coordinates of the w2 position in the SS 433 system for the 2007-2008 data. The black cross indicates the position of the black hole and the black circles indicate the w1 and w2 positions as identified from X-ray observations.

investigate the *Reynoso* model, $\frac{3}{5}$ of the time was reserved for the favored gamma-ray emission phase (see Section 7.3.1 for details), which is around May 30th (with a 15 day range before and after). During Fall 2009, 7 h of data were obtained. In Spring 2010, the observations were scheduled from April 16th, but due to bad weather, only 1 h of data was taken up until May 1st. More observations (10 h) are scheduled starting on May 10th 2010, but unfortunately, those data are not included in this thesis. Table 7–1 summarizes the VERITAS observations taken on SS 433 and analyzed here.

Table 7–1: Details of the VERITAS observations of SS 433

Date (yyyy/mm(dd-dd))	Exposure[1] (h)	Offsets (°)	Mean elevation (°)
2007/10(05-14)	3	0.8-1.3	53
2007/11(01-05)	2.3	0.5-1.3	46
2008/05(07-31)	2	0.7-1.3	57
2008/06(01-06)	3.3	0.7-1.3	60
2009/09(19-23)	4.6	0.5	60
2009/10(10-21)	2.9	0.5	55
2010/04(17-20)	1	0.5	56
Total	18.9	0.75	57

7.5 VERITAS results on the SS 433 system

7.5.1 Trial factor

When looking for a signal in a skymap, one has to make certain that a statistical fluctuation is not taken as a gamma-ray excess. The conventional 5 σ (post-trials) detection threshold is chosen high enough to avoid results that would come from statistical fluctuations. This value corresponds to a probability of 0.00003% that the observed excess is due to a background fluctuation.

When using skymaps containing tens of thousands of bins (160 000 in this case), the probability of finding a high significance excess is greatly increased. We correct the raw statistical probability of a given excess by a *trials factor* accounting for this increased probability. The trials factor can be estimated by accounting for all positions in the skymap where a signal is searched for.

---

[1] Uncorrected for the camera acceptance at different offsets.

7.5.2 Results for the w2 region

In the case of the SS 433 system, the trials for the first data set were limited to the positions of interests; the black hole, w1 and w2 (see Figure 7–4). These regions had already been targeted by previous TeV experiments in the past (see Section 7.2.4). However, since the w1 and w2 regions have an extent of 0.1°, and a bin in our skymap has a width of 0.01°, by looking in one of these regions, the trials factor is of the order of a few hundred. Note that only one set of cuts was used for this first analysis, since no *a priori* assumptions other than point-like emission at moderate flux were made. Adding the factors from the w1 region to these for the w2 region and the black hole position, the total trials factor (629) brings the 4.6 σ excess seen in the first analysis to 3.0 σ, which is much further from the 5 σ detection threshold. Nevertheless, this excess was observed and new observations pointing in wobble mode around the center of the w2 region were taken. Here, the analyses of the new data set (pointing at the w2 region) are presented as well as the analysis of the combined data set.

Results from the observations pointed at the w2 region

From September 2009 to April 20th 2010, a total of 8.5 h of data were recorded and have been analyzed. In this analysis, four sets of cuts were used: *standard* cuts (see Chapter 4) for point and extended source and *hard* cuts for point and extended source. These cuts were used because no assumptions can be made on the type of emission that would be expected from the w2 region. Table 7–2 presents the two cut quantities that vary between the four sets of analysis cuts.

Table 7–2: Analysis cut sets as discussed in this chapter.

Analysis cut	Cut on *size* (d.c.)	Cut on θ^2 (°)
standard point	> 500	< 0.01
standard extended	> 500	< 0.055
hard point	> 1200	< 0.01
hard extended	> 1200	< 0.055

The trials factor in this case will be 4 times the number of bins in the w2 region (314), which gives 1256. The results (pre-trials) for the four sets of cuts on the w2 region are presented in Table 7–3 and in Figures 7–11 and 7–12.

Table 7–3: Results (pre-trials) from the four selected sets of cuts on the w2 region for the 2009-2010 data set. The values presented correspond to the results at the center of the w2 region and the numbers in parentheses correspond to the value of the bin with the maximum significance within the w2 region (of 0.1° radius).

Analysis cut	Exposure (h)	N_{on}	N_{off}	α	Significance (σ)
standard point	8.5	92 (99)	84.8 (72.2)	0.17	0.7 (2.7)
standard extended	8.5	441 (460)	416.3 (408.2)	0.16	1.1 (2.3)
hard point	8.5	20 (25)	11.1 (9.1)	0.17	2.2 (3.9)
hard extended	8.5	70 (73)	62.4 (54.0)	0.17	0.9 (2.3)

From these results, the excess observed in maps using the *hard* cut analysis for a point source suggests that potential emission may have been detected. However, since the significance does not reach the level of 5 σ post-trials, no definitive claim of a detection can be made. Since the *hard* cuts analysis gives the most significant results, this analysis will be used to calculate the flux upper limit for the 2009-2010 data set. The result is a 99% C.L. flux upper limit for energies above 360 GeV (analysis threshold) of 1.33×10^{-12} cm^{-2}s^{-1}.

Results from all the observations usable for the w2 region

By adding the data taken in Fall 2007 and Spring 2008 to the new data set, a total of 18.9 h of observations can be analyzed. Again the four selected cut sets were applied and the results (pre-trials) for the w2 region are presented in Table 7–4 and in Figures 7–13 and 7–14.

Table 7–4: Results (pre-trials) from the four selected sets of cuts of the w2 region for all data available. The values presented correspond to the results at the center of the w2 region and the numbers in parentheses correspond to the value of the bin with the maximum significance within the w2 region (of 0.1°).

Analysis cut	Exposure (h)	N_{on}	N_{off}	α	Significance (σ)
standard point	18.9	169 (186)	139.1 (132.6)	0.16	2.3 (4.1)
standard extended	18.9	788 (839)	733.1 (731.6)	0.16	1.9 (3.5)
hard point	18.9	36 (41)	16.5 (15.4)	0.16	3.8 (4.9)
hard extended	18.9	138 (142)	105.0 (95.8)	0.16	2.8 (4.0)

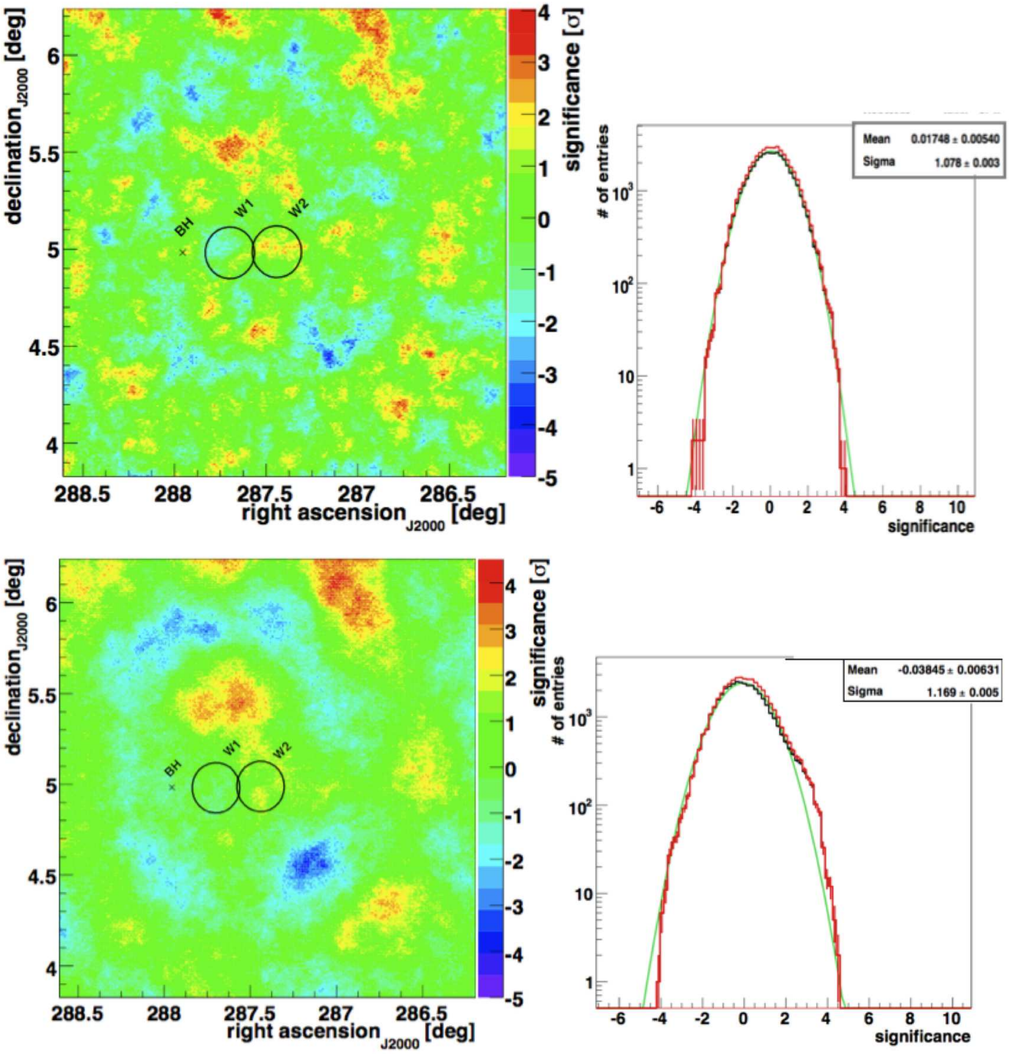

Figure 7–11: Results (pre-trials) for *standard* cut analysis for *point* source (top) and *extended* source (bottom) for the pointed observations on w2 (2009-2010 data set). Left: significance skymaps. The black hole (BH) position is indicated by the black cross and the two black circles indicate the w1 and w2 regions. Right: significance distributions. The red curve represents the significance distribution for all skymap bins. The black curve represents the significance distribution of all the skymap bins except the bins near the source (contained in a radius of 0.4°). The fit to the black curve of a Gaussian distribution is shown with the light green line.

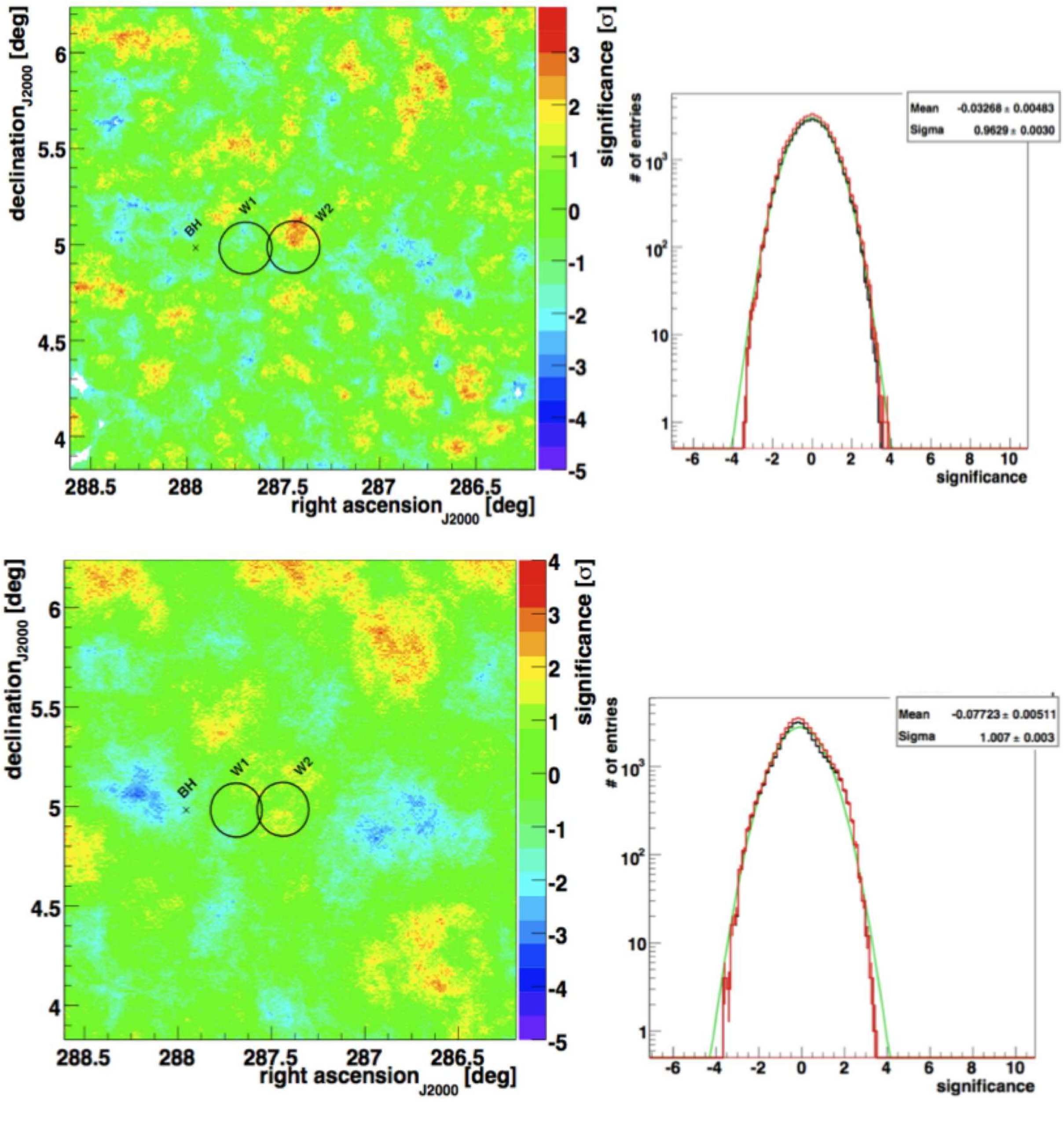

Figure 7–12: Same as Figure 7–11 for *hard* analysis.

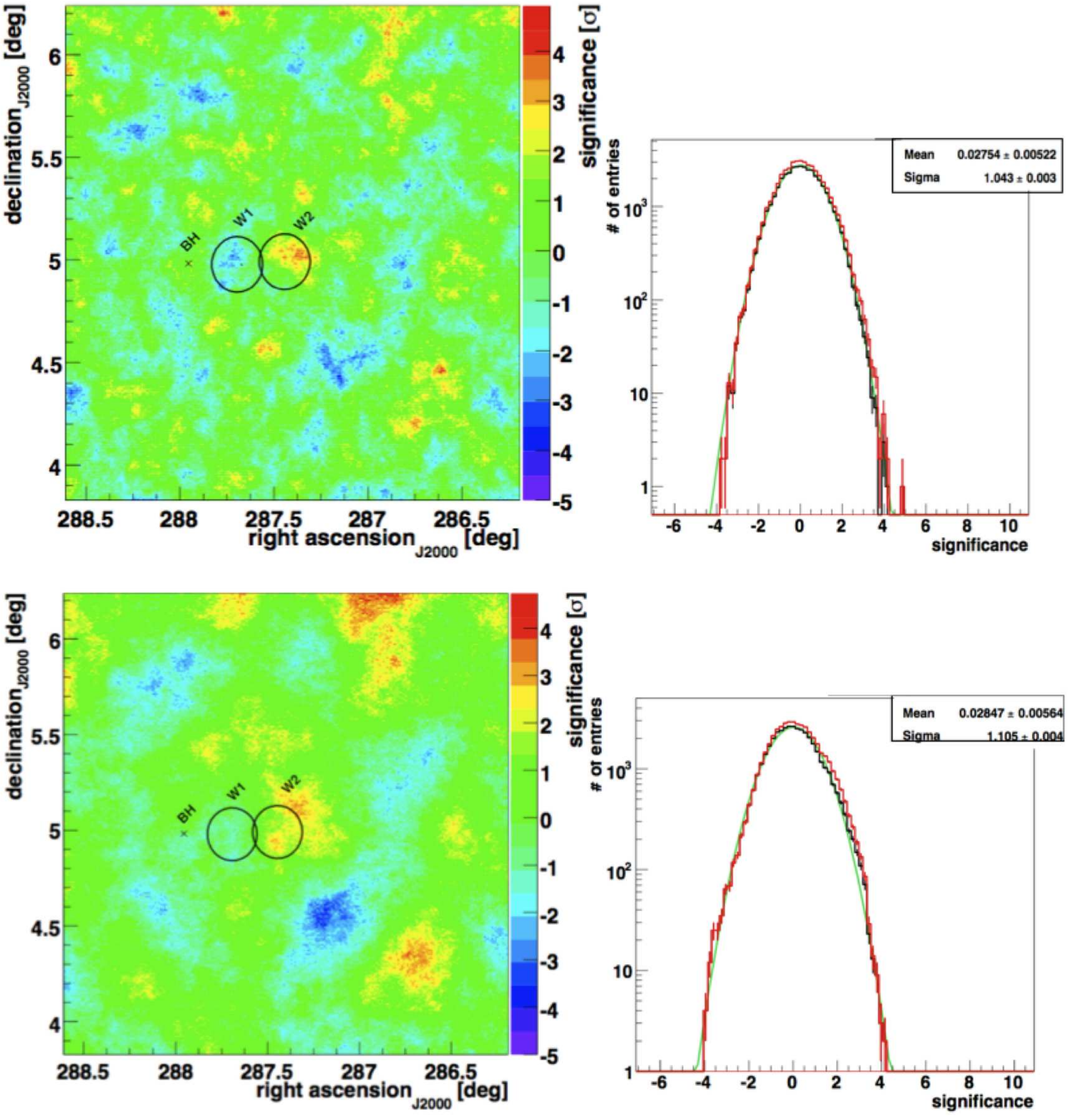

Figure 7–13: Same as Figure 7–11 (*standard* analysis) for the whole data set on the SS 433 system.

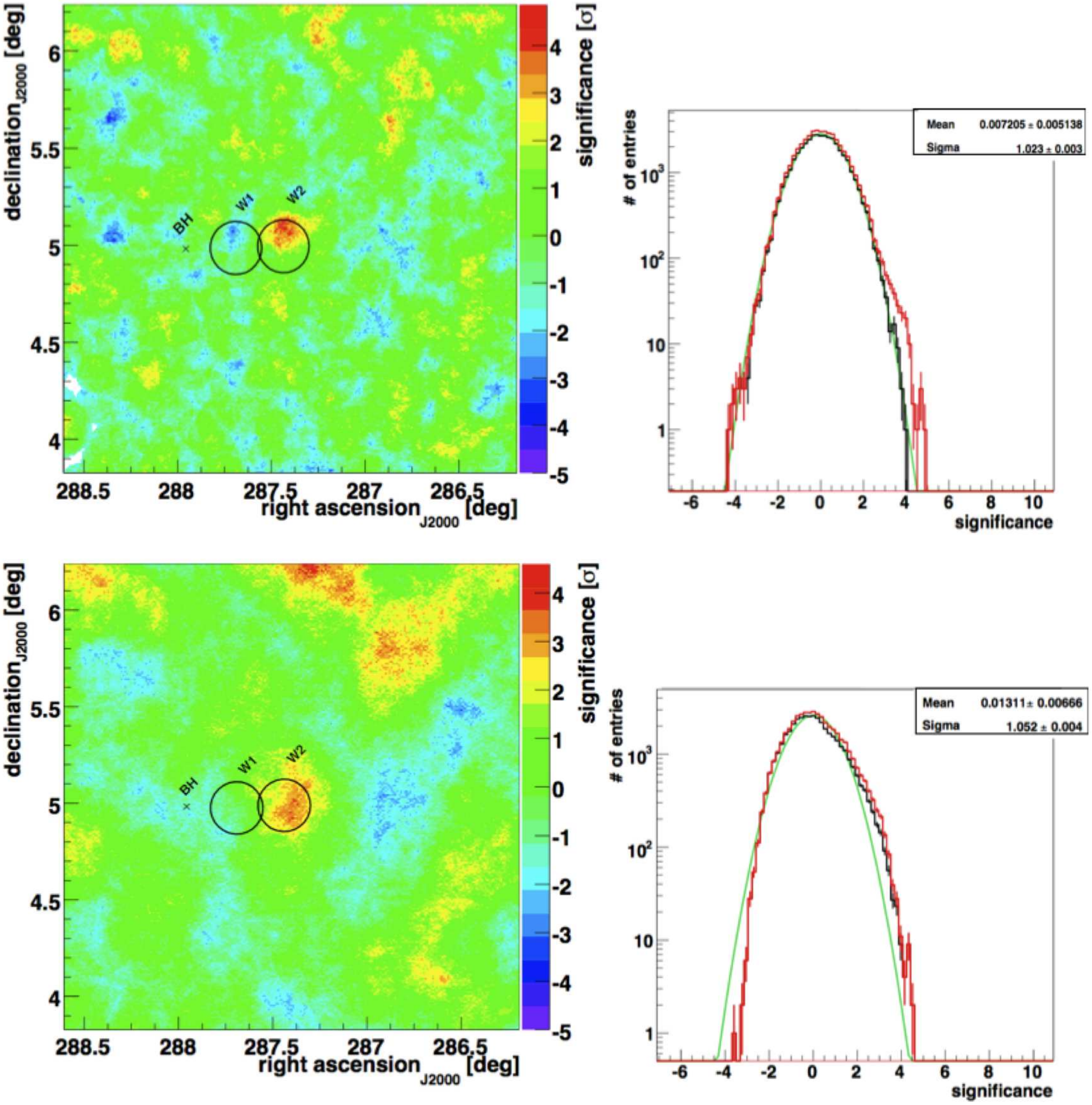

Figure 7–14: Same as Figure 7–11 for *hard* analysis) for the whole data set on the SS 433 system.

7.5.3 Results for the black hole in SS 433

Gamma-ray emission from near the black hole is predicted in the *Reynoso* model. In order to test the model, an analysis has also been performed assuming emission from the black hole position. The results for the black hole position can be seen in Figures 7–11, 7–12, 7–13 and 7–14. Since no excess at the black hole position was found in the archival data (see Figure 7–10), and the emission from the black hole is not expected to be extended, only *standard* cuts are considered further and the full data set (18.9 h) was used.

Because the *Reynoso* model predicts emission during certain orbital phases, the data sets have been separated into phase bins. Figure 7–15 shows the different precessional phases and exposures where VERITAS observed SS 433.

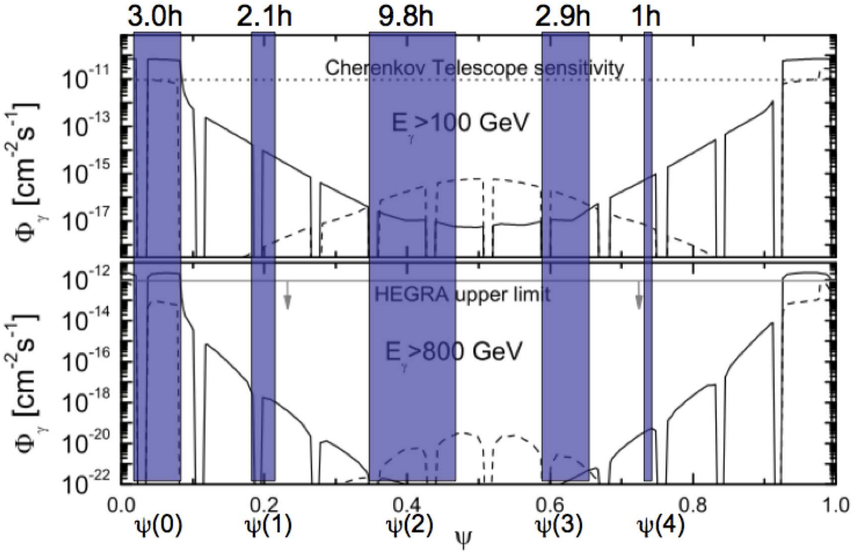

Figure 7–15: Precessional phases where VERITAS observed the SS 433 black hole. The exposure is indicated at the top of each period. The solid line shows the contribution from the approaching jet and the dashed line shows the contribution form the receding jet. Figure adapted from [145].

The results for the analysis of the different precessional phases are presented in Table 7–5, as well as the average on all phases. No gamma-ray excess has been found at any of the phases and flux upper limits have been calculated for energies above 800 GeV in order to compare with the *Reynoso* model. The results are also shown in Figure 7–16 together with the *Reynoso* predictions.

Table 7–5: Results on the analysis at the SS 433 black hole position for different precessional phases (see Figure 7–15 for the details of each phase). The upper limits (U.L.) are calculated at the 99% confidence level for energies above 800 GeV.

Phase	Exposure (h)	N_{on}	N_{off}	α	Significance (σ)	U.L. (cm^{-2} s^{-1}) [Crab Units]
$\Psi(0)$	3.0	21	13.5	0.17	1.7	1.54×10^{-12} [5.1%]
$\Psi(1)$	2.2	8	9.0	0.17	-0.3	1.26×10^{-12} [4.2%]
$\Psi(2)$	9.8	74	58.9	0.16	1.7	3.48×10^{-13} [1.2%]
$\Psi(3)$	2.9	23	22.1	0.16	0.2	1.34×10^{-12} [4.5%]
$\Psi(4)$	1.0	5	4.0	0.16	0.5	1.17×10^{-12} [3.9%]
All	18.9	126	106.4	0.16	1.7	4.39×10^{-13} [1.5%]

7.6 Discussion

7.6.1 The w2 region

The results from the w2 region of the SS 433 system do not show gamma-ray emission above the detection level. The analysis using the *hard* cuts for a *point* source on the 2009-2010 data set (full data set) shows an excess of 3.9 σ (4.9 σ) (pre-trials) within the search region of 0.1° around the w2 center. This is below the conventionally accepted detection level of 5 σ, and no claim of a discovery is made. Although it is tempting to take this excess as evidence of a signal, the quoted significances are pre-trials significances. In fact, an estimate of the post-trials significance

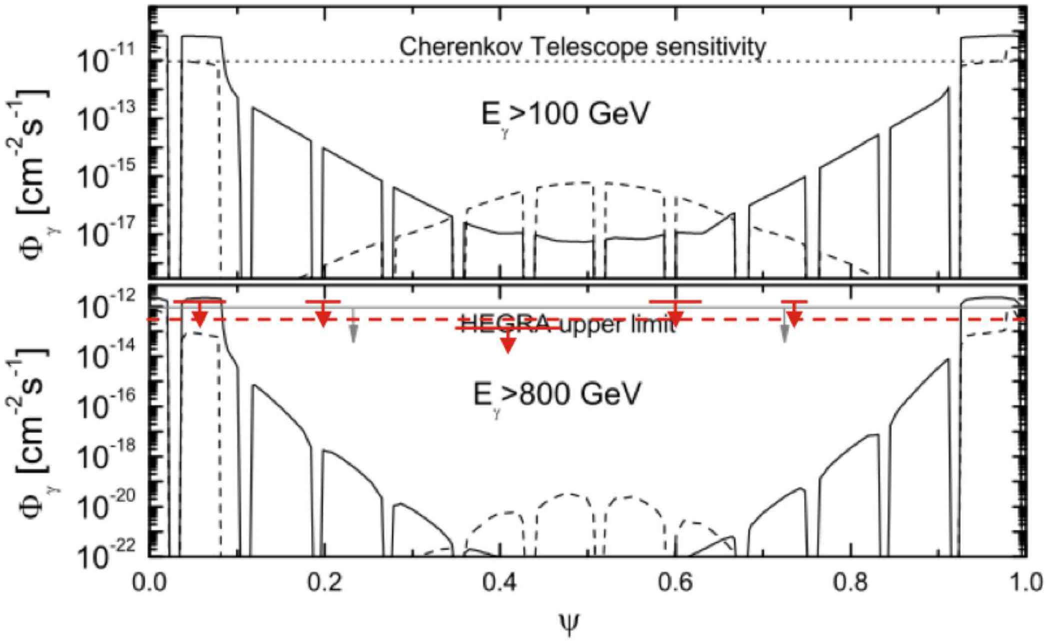

Figure 7–16: VERITAS upper limits on the emission from the SS 433 black hole as a function of precessional phase (thick red arrows) and for the average over all phases (dashed red line). Figure adapted from [145].

can be made. By searching the w2 region, which has an extent in the X-ray data of 0.1°, 314 trials are taken, due to the fact that the size of the skymap bins is $0.01(^\circ)^2$. In addition, 4 sets of cuts were used, bringing the factor to 1256. From this factor the 3.9 σ (4.9 σ) is decreased to 1.6 σ (3.3 σ). Several hours of data will be taken during May 2010.

Even though the excess in the *hard* analysis cannot be attributed to gamma-ray emission yet, it is interesting to use the results to calculate the corresponding gamma-ray flux, in order to compare with the theoretical models. In this case, the results from the full data set are used to calculate the flux. Note that the probability that the signal really does not come from gamma-ray emission is of the order of 0.063% (from the 3.3 σ result). In the eventuality that new observations show an excess above the canonical 5 σ, these conclusions would still hold.

The flux obtained from the *hard* analysis is $(1.1 \pm 0.33) \times 10^{-12}$ cm^{-2} s^{-1} (corresponding to 1.2×10^{-12} erg cm^{-2} s^{-1}) for energies above 360 GeV.

In the *Bordas* model, three regions are considered for gamma-ray production. Since we are studying the w2 region, we ignore the reconfinement region in this discussion (it is too far from the w2 region). In the shell region the dominant radiative process is relativistic Bremsstrahlung and for the cocoon region, the dominant process is inverse Compton scattering (as seen in Figure 7–9). Since the emission from the shell region is more intense than in the cocoon region, we discuss only the shell region. The most optimistic results from the *Bordas* model, *i.e.* the result that predicts the highest flux of emission gives a flux in the shell region of $\approx 10^{-15}$ erg cm^{-2} s^{-1} for energies above 100 GeV, well below the flux calculated from VERITAS results. Figure 7–17 shows the flux point calculated by VERITAS plotted with the most optimistic predicted SED from the shell region.

Considering for a moment that the VERITAS excess at the w2 position is real gamma-ray emission, it is clear that the *Bordas* model under-predicts the gamma-ray emission from the shell region (where the extremity of the jet interacts with the ISM). This would strongly suggest that either some parameters from the model are under-estimated (such as Q_{jet} or χ) or that the emission is powered by hadronic interactions. Hadronic gamma-ray production in the SS 433 system has not yet been

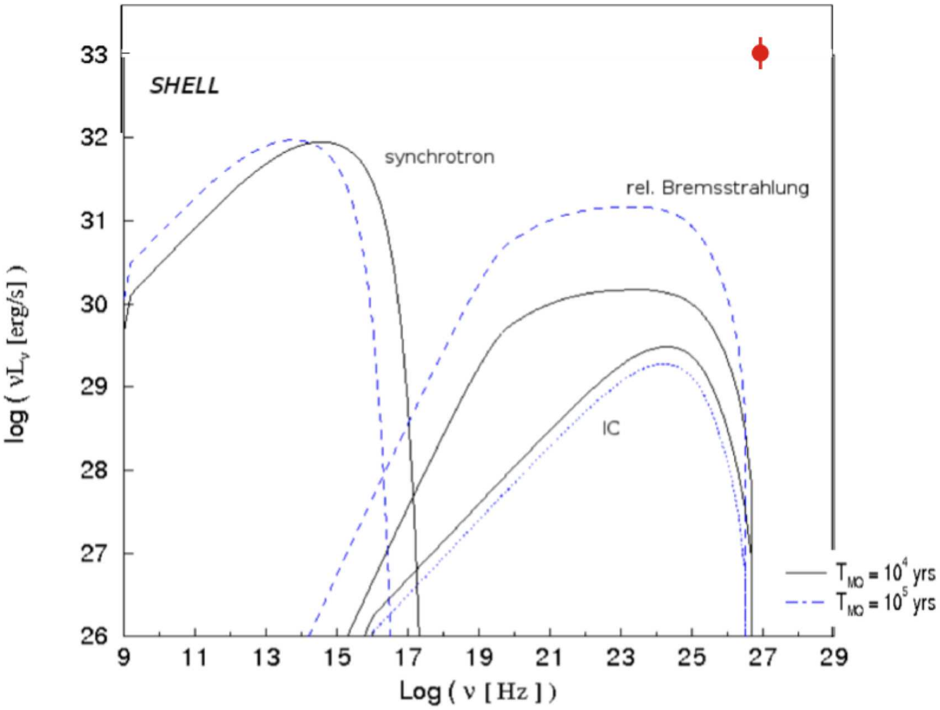

Figure 7–17: SED obtained in the *Bordas* model in the shell region using $Q_{jet} = 10^{37}$ ergs^{-1} and $n_{ISM} = 1$ cm^{-3}. The VERITAS flux point (in red) has been added to the plot. Figure adapted from [23].

modeled. However, it is mentioned in the *Bordas* work that for the following parameters: $t_{MQ} = 10^5$ yr, $Q_{jet} \gtrsim 10^{37}$ erg s^{-1} and shell density of $\sim$1 cm^{-3}, gamma-ray emission would reach the detectable level of $\sim 10^{-12}$ erg cm^{-2} s^{-1}. If, with more data, the VERITAS excess turns out to be a detection, this interpretation would be favored. Nevertheless, detailed modeling of the hadronic scenario will be required to understand the phenomena involved.

7.6.2 The black hole

In the case of the SS 433 black hole, the results obtained in this analysis can be compared to the predictions made in the *Reynoso* model. The predicted flux is a function of the precessional phase of the system. As seen in Figure 7–16, the upper limits computed in this work do not strongly constrain the theoretical predictions. The only limit is below the level of the predictions is at phase 0. However the limit covers only a small region of the predictions, making it impossible to draw strong conclusions about the constraints. Clearly, more data are needed to understand the VHE emission of this system. New data is scheduled to be taken in May 2010, during the precessional phase 0, which may constrain much more strongly the predictions of the *Reynoso* model.

CHAPTER 8
Conclusion

The field of VHE gamma-ray astrophysics has undergone an important evolution in the last two decades. The number of sources detected at these wavelengths has passed from a handful to over 100 in the last 10 years. These detections have proven that very energetic phenomena occur in the Universe and that efficient particle acceleration is happening in several astrophysical objects. Despite the new discoveries in the TeV band, the understanding of the physical processes involved in VHE emission is still far from complete. Several theoretical models have been put forward to try to explain the radiative mechanisms, however, the current observations do not yet strongly constrain those models.

Magnetars, highly magnetized neutron stars, are exotic objects. Only a handful of such objects are known to date, and the theoretical models explaining the radiative processes occurring in magnetars are not yet fully satisfactory. VERITAS observed three magnetars, showing no significant VHE gamma-ray emission in quiescent emission phase. This result supports the current theoretical models, where no VHE emission is predicted. However, in the case of magnetars, major outbursts occur, and some models have suggested that VHE gamma rays could be emitted during these flares. VERITAS has included all the known magnetars visible to it in its burst alert program in order to observe these objects during major outbursts. Such observations would be very useful to constrain the models predicting VHE gamma-ray emission.

Among the hundreds of X-ray binaries in the Galaxy, three systems have been detected in the TeV band. Two main theoretical models have been proposed to explain the VHE component of the emission. One of the model seems to be relatively satisfactory in one case, but for the two others, the models cannot explain completely the emission. In addition, it is not clear which physical characteristics of the binary systems are responsible of the TeV emission. Searching in the VERITAS archival data, 15 X-ray binaries have been analyzed. No gamma-ray emission was detected from these systems. It was shown that from these results, no conclusions could be drawn about a potential relation between the physical properties of the systems and the TeV emission, due to the fact that the observed systems were significantly different from the three known TeV emitting systems and that several properties were still unidentified in some systems. However, these results are very useful for future VHE observations, giving upper limits on the VHE emission.

The SS 433 system was also presented in this thesis. VHE gamma-ray emission from microquasars has been proposed, however, no gamma-ray emission has been detected from any microquasars yet. The SS 433 system is unique. The relativistic jets are firing into the surrounding medium. The interaction between the jet and the medium has already been observed at different wavelengths. VHE emission from near the black hole and from the interaction between the jet and the surrounding medium has been predicted by detailed models of the SS 433 system. VERITAS observed the system for almost 19 h, and no significant gamma-ray emission was detected at either the black hole or the region of interaction between the jet and the surrounding medium. A total significance of 4.9 σ (pre-trials) was found in the 0.1° search region of the western region where the jet interacts with the ISM. Nevertheless, this excess cannot be attributed to gamma-ray emission with certainty. In addition, the trials factor has been estimated conservatively, and the excess significance is considerably reduced post-trials. More observations will be taken shortly and the results will show if the excess seen here is due to gamma-ray emission or to a statistical fluctuation. An interpretation of the results, considering the excess as a gamma-ray signal, was performed, putting strong constraints on the theoretical model predicting such emission. However, this interpretation is conditional on a future detection of this region.

No significant gamma-ray emission was found in any of the galactic objects studied here. These results are important for current and future theoretical models, giving upper limits on the gamma-ray flux. In addition, the results will be useful for future observational proposals in the VHE regime, giving a firm idea of the emission level of these objects. Finally, the SS 433 system requires more data in order to confirm or to refute the excess seen in the analysis of the region where the western jet interacts with the surrounding medium.

Appendix A: Studies of the camera radial acceptance

Some background models are strongly dependent on the radial acceptance curve of the camera; the systematic errors in significance and flux calculations depend on the input radial acceptance curves. In particular, the FOV background model (which has not been discussed in this work) depends strongly on a good knowledge of the camera radial acceptance. An inappropriate radial acceptance curve will result in an under- or over-estimation of the background, causing an incorrect calculation of a potential signal. It is very important to have a full understanding of how different parameters, like the zenith angle or the energy of the showers, affect the camera radial acceptance. Here, the results of different studies made on the camera radial acceptance are presented. The effect of the shower's energy, the zenith angle of the observations, the azimuth angle of the observations and the validity of the camera radial symmetry assumption have been investigated.

All the results presented here have been produced with the following cuts: theta square $< 0.025^{\circ 2}$, distance cut in the camera of 1.2°, array mean scaled width between -1.2° and 0.5° and array mean scaled length between -1.2° and 0.5°, cut of 250 m on the distance of the core position to the telescopes, requirement of more than two telescopes trigerring and a 10% loss cut at the edge of the camera. The radial acceptance curves are produced with data, from gamma-ray-like background events of observations where no gamma-ray emission has been observed, or with simulations, from simulated gamma-rays.

Radial symmetry

The first assumption made for the camera acceptance is that the acceptance is radially symmetrical. Since we rotate a one-dimensional acceptance curve (obtained from the fit on the data, see Figure 4–9) around the camera center to produce the two-dimensional radial acceptance, it is crucial that the camera acceptance has radial symmetry. Figure 8–1 shows an example of a two-dimensional radial acceptance curve obtained from data (left panel) and from the model (1D radial acceptance curve rotated around the camera center) (middle panel). The residual map in sigma between the data produced acceptance curve and the model produced acceptance curve is shown in right panel of Figure 8–1.

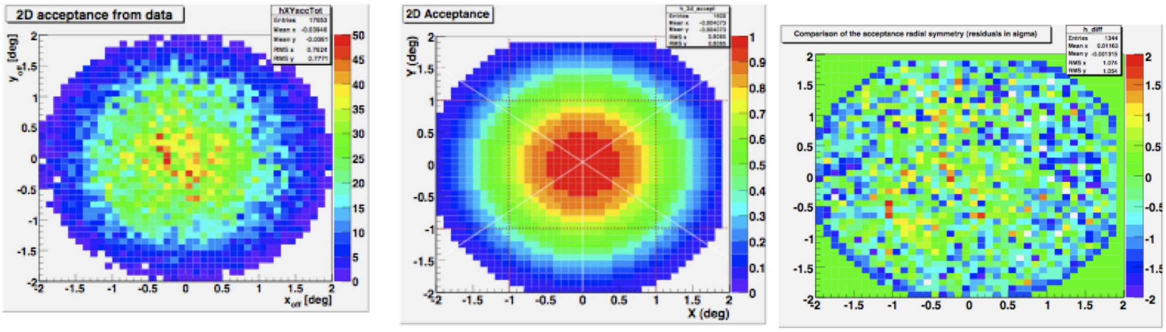

Figure 8–1: Left panel: 2D camera radial acceptance produced from data. Middle panel: 2D acceptance produced from the 1D fit to the data rotated around the camera center. Middle panel: Residual map in sigma between the left and middle histograms.

The residual plot shows that most bins are consistent within the errors (0 to 2 sigmas) with no residuals between the data and the model. In order to see this effect more clearly, a projection of the 2D histograms (from Figure 8–1) have been done.

Figure 8–2 shows these projections in x and y for the data and the model (top panels) and the sigma distribution of the residual 2D histogram (bottom panel). This last plot shows clearly that the residuals between the data and the assumed model are consistent with a null hypothesis, being well fitted by a Gaussian (mean 0 and sigma 1). In addition, the x and y projections show good agreement between the data and the model.

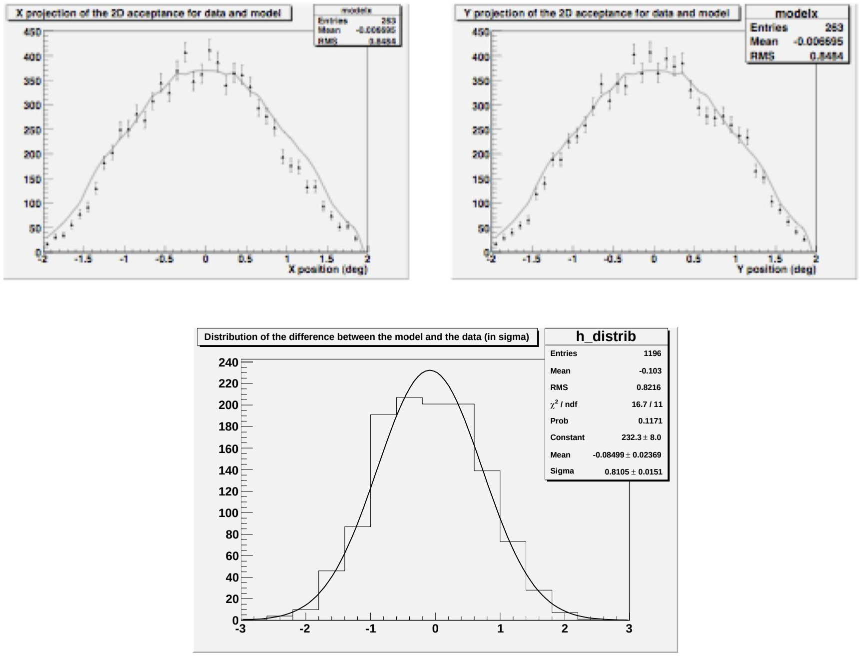

Figure 8–2: Top panels: Left panel: X projection between -1° to 1 ° of the 2D acceptance curves for the data (points) and for the model (solid line). Right panel: Y projection between -1° to 1 ° of the 2D acceptance curves for the data (points) and for the model (solid line). Bottom panel: sigma distribution of the residuals between the data and the model. The distribution is well fitted by a Gaussian of mean 0 and sigma of 1.

Zenith and azimuth angle dependence

Figure 8–3 shows how the radial acceptance varies with the zenith angle and the azimuth angle of the observations. These plots have been produced with simulations, not with real data. The reason for using simulations instead of real data is that there is not enough statistics with the data to split them into several zenith angle bins. Those simulations produced at seven different offsets in the camera (from 0.3° to 1.5°) contain 150 000 gamma-rays within a radius of 750 m around the telescopes, analyzed with the same cuts mentioned before.

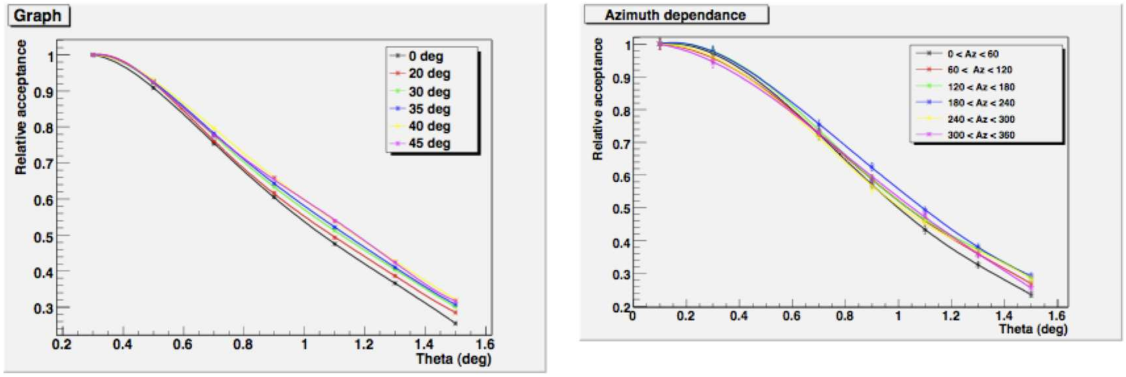

Figure 8–3: Zenith angle (left) and azimuth angle (right) dependence of the radial acceptance curve.

The zenith angle dependence (left panel of Figure 8–3) shows that the smaller the zenith angle is, the lower the acceptance curve is. Near the camera center, $\theta <$ 0.6°, the difference is of the order of a few percent ($\approx$ 3%), but when you go further out in the camera that difference increases to a few tens of percent ($\approx$ 35%).

For the azimuth angle dependence, the right plot of Figure 8–3 shows that there is up to $\approx$ 20% difference between the North (300° $<$ Az $<$ 60°) and the South (120° $<$ Az $<$ 240°) further out in the camera. Near the camera center, this difference is only a few percent (≈ 6%). This difference is explained by the geomagnetic field that influences more the showers coming from the North, as explained in Section 4.5.1.

Energy dependence

Figure 8–4 shows how the energy of the incoming shower affects the radial acceptance curve of the camera. The left plot is from simulations where two analysis have been done; one using a 10% loss cut and one without. Recall that the loss cut reject events having more than a defined percentage of the shower contained in the edge pixels (see Section 4.2.2). The right plot has been produced with data that have been taken at different wobble offsets. There is much fewer statistics in the data than in the simulations.

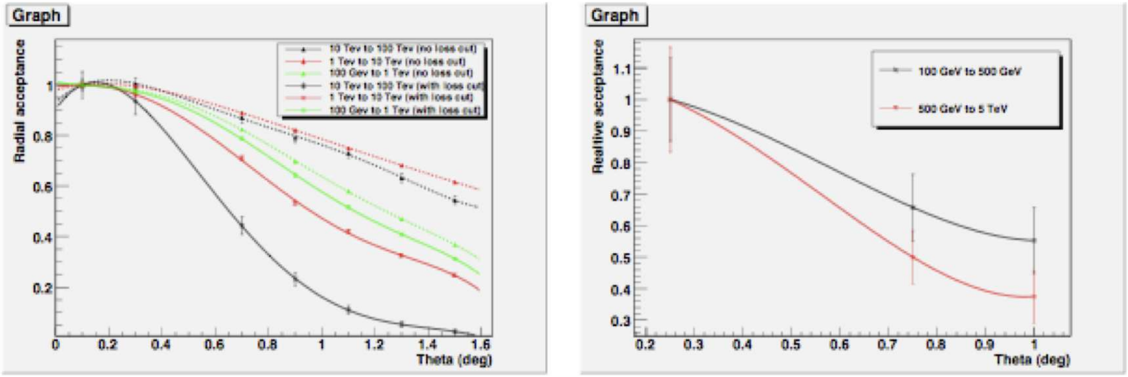

Figure 8–4: Energy dependence of the radial acceptance curve for simulations (left) (with the loss parameter of 10% applied (solid lines) and without it (dashed lines)) and for Crab data (right).

Because the loss cut is applied at the edge of the camera, high energy shower acceptance drops dramatically, for both data and simulations. At lower energy this effect is much smaller.

Conclusions

From these different studies, it has been shown that assuming a radial symmetry in the camera acceptance is valid.

For the dependence on the zenith and azimuth angle of the observations, effects up to 35% and 20% respectively have been found, showing that using radial acceptance curves with appropriate zenith and azimuth angle is recommended. However, most of VERITAS observations are performed at zenith angle varying from 20° to 35°. In this case, the difference in radial acceptance is less than 5% at a distance of 1° in the camera. This means that using an radial acceptance curve averaged over these three zenith angle bins will not have a noticeable effect on the analysis.

In the case of the azimuth dependence, the effect in the camera radial acceptance can go up to 20% between North and South. However, by using a radial acceptance curve averaged over all azimuth angles, the effect is reduced to less $\approx$ 10% at a distance of 1° in the camera. Therefore, using an averaged acceptance curve is correct.

Finally, it has been shown that the energy dependence is very important. However, in the VERITAS analysis, the events used for the source position are events with energy corresponding to the energy threshold (few hundreds GeV), therefore the uncertainty brought by the radial acceptance curve at high energy does not affect the results.

Abbreviations

AGILE	Astro-rivelatore Gamma a Immagini LEggero
AGIS	Advanced Gamma-Ray Imaging System
AGN	Active Galactic Nuclei
AXP	Anomalous X-ray Pulsar
BAT	Burst Alert Telescope
BATSE	Burst And Transient Source Experiment
CASA-MIA	Chicago Air Shower Array MIchigan muon Array
CFD	Constant Fraction Discriminator
CGRO	Compton Gamma-Ray Observatory
C.L.	Confidence Level
CMB	Cosmic Microwave Background
COMPTEL	COMPton TELescope
CTA	Cherenkov Telescope Array
Dec	Declination
EGRET	Energetic Gamma-Ray Experiment Telescope
ESA	European Space Agency
FADC	Flash Analog to Digital Converter
FLWO	Fred Lawrence Whipple Observatory
FOV	Field of view

GBM	Gamma-ray Burst Monitor
GCN	Gamma-ray burst Coordinates Network
GeV	Giga electron Volt
GHz	Giga Hertz
GPS	Global Positioning System
GRB	Gamma-Ray Burst
HAWC	High Altitude Water Cherenkov
HE	High Energy
HEGRA	High Energy Gamma-Ray Astronomy
H.E.S.S.	High Energy Stereoscopic System
HMXB	High Mass X-ray Binary
IACT	Imaging Air Cherenkov Telescope
IC	Inverse Compton
ICS	Inverse Compton Scattering
INTEGRAL	International Gamma-Ray Astrophysics Laboratory
IR	InfraRed
ISM	InterStellar Medium
keV	kilo electron Volt
LAT	Large Area Telescope
LMXB	Low Mass X-ray Binary

MAGIC	Major Atmospheric Gamma-ray Imaging Cherenkov
MeV	Mega electron Volt
MHz	Mega Hertz
MJD	Modified Julian Day
Mrk	Markarian
MSCL	Mean SCaled Length
MSCW	Mean SCales Width
NASA	National Aeronautics and Space Administration
NSB	Night Sky Background
OSO	Orbiting Solar Observatory
OSS	Optical Support Structure
OSSE	Oriented Scintillation Spectrometer Experiment
PMT	PhotoMultiplier Tubes
PSF	Point Spread Function
PWN	Pulsar Wind Nebula
Ra	Right ascension
RXTE	Rossi X-ray Timing Explorer
SAS	Small Astronomy Satellite
SED	Spectral Energy Distribution
SGR	Soft Gamma-ray Repeater
SNR	SuperNova Remnant

TeV	Tera electron Volt
UHE	Ultra High Energy
U.L.	Upper Limit
UV	Ultra Violet
VBF	VERITAS Bank Format
VERITAS	Very Energetic Radiation Imaging Telescope Array System
VHE	Very High Energy
VLA	Very Large Array
VLBA	Very Long Baseline Array
XMM	X-ray Multi-mirror Mission
ZCD	Zero Crossing Discriminator

References

[1] Abdo A.A. et al. *ApJ*, 706:L56–L61, 2009.

[2] Abdo A.A. et al. *ApJ*, 701:L123–L128, 2009.

[3] Abdo A.A. et al. *Science*, 326:1512–1516, 2009.

[4] Acciari V. et al. *ApJ*, 679:1427, 2008.

[5] Acciari V. et al. *Science*, 325:44, 2009.

[6] Acciari V. et al. *Nature*, 462:770–772, 2009.

[7] Acero F. et al. *Science*, 326:1080–1082, 2009.

[8] Aharonian F. et al. *A&A*, 403:L1, 2003.

[9] Aharonian F. et al. *ApJ*, 614:897, 2004.

[10] Aharonian F. et al. *A&A*, 442:1, 2005.

[11] Aharonian F. et al. *Science*, 309:746–749, 2005.

[12] Aharonian F. et al. *A&A*, 439:635–643, 2005.

[13] Aharonian F. et al. *A&A*, 460:743–749, 2006.

[14] Aharonian F. et al. *A&A*, 467:1075–1080, 2007.

[15] Aharonian F. and Jelley J.V. *ApJ*, 695:L40–L44, 2009.

[16] Albert J. et al. *Science*, 312:1771, 2006.

[17] Albert J. et al. *ApJ*, 665:L51–L54, 2007.

[18] Barthelmy S.D. et al. *GCN Circular 8113*, 2008.

[19] Baykal A. and Swank J. *ApJ*, 460:470, 1996.

[20] Bednarek W. *MNRAS*, 397:1420–1425, 2009.

[21] Bhattacharya D. and Soni V. *arXiv e-prints/0705.0592*, 2007.

[22] Blackett P. *Physical Society Gassiot Committe Report 34*, 1948.

[23] Bordas P. et al. *A&A*, 497:325, 2009.

[24] Borione A. et al. *proceeding of the 23rd ICRC*, 1993.

[25] Bosch-Ramon V. et al. *ApJ*, 628:388, 2005.

[26] Cameron P.B. et al. *ATel 312*, 2004.

[27] Campanas L. et al. *A&A*, 384:163, 2002.

[28] Casares J. et al. *MNRAS*, 364:899, 2005.

[29] Celik O. et al. *Proceedings of the 30th ICRC, Merida, Mexico*, 2007.

[30] Cherepashchuk A.M. et al. *A&A*, 437:561, 2005.

[31] Coe M.J. et al. *MNRAS.*, 261:599, 1993.

[32] Cogan P. *PhD thesis, University College Dublin*, 2006.

[33] Connors T.W. et al. *MNRAS*, 336:1201, 2002.

[34] Cusumano G. et al. *A&A*, 440:1079–1086, 2005.

[35] Davies J.M. and Cotton E.S. *Journ. of solar Energy*, 1:26–32, 1957.

[36] den Hartog P.R. et al. *A&A*, 451:587–602, 2006.

[37] den Hartog P.R. et al. *A&A*, 09390, 2008.

[38] Dhawan V. et al. *Proceedings of the VI Microquasar Workshop: Microquasars and Beyond. Sept. 2006, Italy*, page 52.1, 2006.

[39] Dib R. *PhD thesis, McGill University*, 2009.

[40] Donati J.F. et al. *MNRAS*, 333:55, 2002.

[41] Donati J.F. et al. *MNRAS*, 370:639–644, 2006.

[42] Donati J.F. et al. *MNRAS*, 365:L6–L10, 2006.

[43] Dubner G.M. et al. *ApJ*, 116:1842–1855, 1998.

[44] Dubus G. *A&A*, 456:801, 2006.

[45] Dubus G. *New Astr. Rev.*, 51:778–784, 2008.

[46] Dubus G. and Giebels B. *ATEL 1715*, 2008.

[47] Duncan R. *http://solomon.as.utexas.edu/ duncan/magnetar.html.*

[48] Duncan R. and Thompson C. *ApJ*, 392:L9–L13, 1992.

[49] Durant M. and van Kerkwijk M.H. *ApJ*, 650:1070, 2006.

[50] Durouchoux P. et al. *Adv.Space Res.*, 25:703–708, 2000.

[51] Enoto T. et al. *ApJ*, 693:L122, 2009.

[52] Ertan U. et al. *ApJ*, 657:441–447, 2007.

[53] Esin A.A. et al. *ApJ*, 532:1069, 2000.

[54] Fabirka S. *Astrophys. Space Phys. Rev.*, 12:1, 2004.

[55] Fegan S.D. *Nucl.Part.Phys.*, 23:1013–1060, 1997.

[56] Ferrario L. and Wickramasinghe D. *MNRAS*, 367:1323–1328, 2006.

[57] Frail D.A. and Hjellming R.M. *ApJ*, 101:2126–2130, 1991.

[58] Gaensler B.M. and Chatterjee S. *GCN Circular 8149*, 2008.

[59] Galbraith W. *Space Sc. Rev.*, 75:17–30, 1953.

[60] Galbraith W. and Jelley J.V. *Space Sc. Rev.*, 75:17–30, 1955.

[61] Galloway D.K. et al. *ApJ*, 613:1164, 2004.

[62] Galloway D.K. et al. *ApJ*, 622:L45–L48, 2005.

[63] Gammell S. *PhD thesis, University College Dublin*, 2004.

[64] Gavriil F.P., Dib R., and Kaspi V.M. *40 Years of Pulsars: Millisecond Pulsars, Magnetars and More, held 12-17 August 2007, in Montreal, QC.*, 983, 2008.

[65] Gies D.R. and Bolton C.T. *ApJ*, 304:371–393, 1986.

[66] Gogus E. et al. *GCN Circular 8118*, 2008.

[67] Grube J. et al. *Proceedings of the 30th ICRC, Merida, Mexico*, 2007.

[68] Guenette R. et al. for the VERITAS collaboration. *Proceedings of the 31st ICRC, Poland*, 2009.

[69] Guidorzi C. et al. *A&A*, 416:297–310, 2004.

[70] Guver T., Ozel F., and Gogus E. *ApJ*, 675:1499–1504, 2008.

[71] Halpern J.P. and Gotthelf E.V. *ApJ*, 710:941–947, 2009.

[72] Halzen F., Landsman H., and Montaruli T. *arXiv:astro-ph/0503348v1*, 2005.

[73] Harrison T.E. et al. *ApJ*, 133:162, 2007.

[74] Heck D. et al. *Forschungzentrum Karlsrushe Report FZKA*, 6019, 1998.

[75] Helene O. *Nucl. Instr. Meth.*, 483:868, 1983.

[76] Hellier C. *MNRAS*, 271:L21, 1994.

[77] Hillas A.M. *Proceedings of the ICRC*, 1985.

[78] Hillas A.M. *Space Sc. Rev.*, 75:17–30, 1996.

[79] Hjellming R.M. et al. *ApJ*, 246:L141–L145, 1981.

[80] Holder J. et al. *Proceeding of the 31st ICRC, Poland, July 2009*, 2009.

[81] Holland S.T. et al. *GCN Circular 8112*, 2008.

[82] Horan D. *PhD thesis, University College Dublin*, 2001.

[83] http://chandra.harvard.edu/photo/1999/0052/.

[84] http://commons.wikimedia.org/wiki/ File:Atmospheric_electromagnetic_transmittance_or_opacit

[85] http://fermi.sonoma.edu/multimedia/gallery/.

[86] http://hawc.umd.edu/index.php.

[87] http://heasarc.gsfc.nasa.gov/docs/cgro/images/epo/gallery/skymaps/.

[88] http://imagine.gsfc.nasa.gov/docs/sats_n_data/satellites/cgro_image.html.

[89] http://magic.mppmu.mpg.de/.

[90] http://svs.gsfc.nasa.gov/vis/a010000/a010500/a010508/.

[91] http://tevcat.uchicago.edu/.

[92] http://umdgrb.umd.edu/cosmic/milagro.html.

[93] http://veritas.sao.arizona.edu/.

[94] http://veritas.sao.arizona.edu/content/blogsection/6/40/l.

[95] http://www.agisobservatory.org/.

[96] http://www.ast.leeds.ac.uk/ fs/showerimages.html.

[97] http://www.astro.ucla.edu/ veritas/docs/sub_proj8/cfd.pdf.

[98] http://www.mpi hd.mpg.de/hfm/CTA/CTA_arrays.html.

[99] http://www.mpi hd.mpg.de/hfm/HEGRA/HEGRA.html.

[100] http://www.mpi hd.mpg.de/hfm/HESS/HESS.shtml.

[101] http://www.nasa.gov/centers/goddard/news/topstory/2007/active_galaxy.html.

[102] in 't Zand J.J.M. et al. *A&A*, 361:85–91, 2000.

[103] in 't Zand J.J.M. et al. *A&A*, 380:L26–L29, 2001.

[104] in 't Zand J.J.M. et al. *A&A.*, 469:1063–1068, 2007.

[105] Johnston S. et al. *ApJ*, 387:37, 1992.

[106] Johnston S. et al. *MNRAS*, 268:430, 1994.

[107] Johnston S. et al. *MNRAS*, 279:1026, 1998.

[108] Johnston S. et al. *MNRAS*, 358:1069, 2005.

[109] Karasev D.I. et al. *Astr. Lett.*, 34:753–760, 2008.

[110] Kareet P. et al. *ApJ*, 542:L41–L43, 2000.

[111] Kaspi V.M. et al. *ApJ*, 588:L93, 2003.

[112] Khelifi B. et al. *Proceedings of the 30th ICRC, Merida, Mexico*, 2007.

[113] Kildea J. et al. *Astropart. Phys.*, 28:182–195, 2007.

[114] Kiziloglu U. et al. *AN*, 328:142, 2006.

[115] Klochkov D. et al. *A&A*, 491:833, 2008.

[116] Li T.P. and Ma Y.Q. *ApJ*, 272:317–324, 1983.

[117] Ling Z. et al. *ApJ*, 695:111, 2009.

[118] Liu Q.Z., van Pardijs J., and van den Heuvel E.P.J. *A&A*, 455:1165, 2006.

[119] Liu Q.Z., van Pardijs J., and van den Heuvel E.P.J. *A&A*, 469:807, 2007.

[120] Luo Q. *AIP Conference Proceedings*, 745:365–370, 2005.

[121] Luo Q. *ASA Conference 2004*, 22:157–161, 2005.

[122] MAGIC Collaboration. *Science*, 322:1221–1224, 2008.

[123] Maier G. et al. *Proceedings of the 30th ICRC, Merida, Mexico*, 2007.

[124] Margon B. et al. *ApJ*, 230:L41, 1979.

[125] Mattan F. et al. *A&A*, 460:L1, 2006.

[126] Mazets E.P. et al. *Nature*, 282:587, 1979.

[127] McCann A. et al. *Astropart. Phys.*, 32:325–329, 2009.

[128] Migliari S. et al. *Science*, 297:1673, 2002.

[129] Mirabel I.F. *Science*, 312, 2006.

[130] Mohanty G. *Astropart.Phys.*, 9:15, 1998.

[131] Moldowan A. et al. *Adv. Space Res. arXiv:astro-ph/0501361v1*, 2005.

[132] Morel T. and Grosdidier Y. *MNRAS*, 356:665, 2005.

[133] Muno M. et al. *ATEL 902*, 2006.

[134] Muno M.P. *AIP Conference Proceedings*, 924:166–173, 2007.

[135] Neronov A. and Chernyakova M. *ApSS*, 309:253–259, 2007.

[136] Ohm S. et al. *Proc. of the Conf. on High Energy Phenomena in Massive Stars, Jaen, February 2009*, 2009.

[137] Orellana M. et al. *A&A*, 465:703, 2007.

[138] Panferov A.A. *contribution to conference HEA-2009, Moscow, December, 2009/arXiv:1001.5097v1*, 2010.

[139] Paredes J.M. et al. *Science*, 288:2340, 2000.

[140] Punch W. et al. *Nature*, 358:477, 1992.

[141] Rea N. et al. *MNRAS*, 396:2419–2432, 2009.

[142] Rees M.J. and Meszaros P. *ApJ*, 545:L73–L75, 2000.

[143] Reig P. et al. *A&A*, 322:183, 1997.

[144] Reig P. et al. *ApJ*, 528:L25–L28, 2000.

[145] Reynoso M. et al. *MNRAS*, 387:1745–1754, 2008.

[146] Reynoso M. et al. *Astropart. Phys.*, 28:565–572, 2008.

[147] Ribo M. et al. *A&A*, 481:17–20, 2008.

[148] Roache E. et al. *Proceedings of the 30th ICRC, Merida, Mexico*, 2007.

[149] Romero G.E. *Chin.J.Astron.Astrophys.*, 5:110–120, 2005.

[150] Safi-Harb S. and H. Ogelman. *ApJ*, 483:868–881, 1998.

[151] Sarty G.E. et al. *MNRAS*, 392:1242, 2009.

[152] Skinner S.L., Perna R., and Zhekov S.A. *ApJ*, 653:587–592, 2006.

[153] Stirling A.M. et al. *MNRAS*, 337:657–662, 2002.

[154] Stolleberg M.T. et al. *ApJ*, 512:313, 1999.

[155] Swank J. and Morgan E. *IAUC*, 7531, 2000.

[156] Tauris T. and van den Heuvel E.P.J. *arXiv:astro-ph/0303456v1*, 2003.

[157] Tavani M. et al. *Nature*, 462:620–623, 2009.

[158] Taylore J.H. and Cordes J.M. *ApJ*, 411:4674, 1993.

[159] Thompson C. and Beloborodov A.M. *ApJ*, 634:565–569, 2005.

[160] Thompson C., Lyutikov M., and Kulkarni S. *ApJ*, 574:332, 2002.

[161] Thompson C. and Duncan R. *ApJ*, 408:194–217, 1993.

[162] Thompson C. and Duncan R. *MNRAS*, 275:255–300, 1995.

[163] Thompson C. and Duncan R. *ApJ*, 473:322–342, 1996.

[164] Tian W.W., Leahy D.A., and Li D. *to be published in MNRAS*, 2010.

[165] Torres M.A.P. et al. *ApJ*, 672:1079–1090, 2008.

[166] Valcarcel L. *PhD thesis, McGill University*, 2008.

[167] van Kerkwijk M.H. et al. *Nature*, 355:703, 1992.

[168] Vasileiou V. et al. for the Fermi Collaboration. *Proceedings of the 31st ICRC, Poland*, 2009.

[169] Vasiliev L. et al. *A&A*, 362:L53, 2000.

[170] Vermeulen R.C. et al. *A&A*, 270:177–188, 1993.

[171] Wang Z., Chakrabarty D., and Kaplan D.L. *Nature*, 440:772–775, 2006.

[172] Watson M.G. et al. *ApJ*, 273:688, 1983.

[173] Weekes T.C. et al. *Very High Energy Gamma-Ray Astronomy, Institute of Physics, Bristol*, 2003.

[174] Weekes T.C. et al. *ApJ* 342:379, 1989.

[175] Weinstein A. et al. *Proceedings of the 30th ICRC, Merida, Mexico*, 2007.

[176] Wen L. et al. *ApJS*, 163:372–392, 2006.

[177] Wex N. et al. *MNRAS*, 298:997, 1998.

[178] Wilson C.A. et al. *ApJ*, 570:287–302, 2002.

[179] Wilson C.A. et al. *ApJ*, 687:1263, 2008.

[180] Woods P. et al. *GCN Circular 8166*, 2008.

[181] Woods P.M. et al. *ApJ*, 605:378–399, 2004.

[182] Ziolkowski J. *MNRAS*, 358:851–859, 2005.